Master thesis and internship[BR]- Master's thesis : Experimental and Numerical Analysis of Aerodynamic Forces on Small Caliber Projectiles in Supersonic Flows[BR]- Internship

Auteur : Sow, Oumar
Promoteur(s) : Andrianne, Thomas
Faculté : Faculté des Sciences appliquées
Diplôme : Master en ingénieur civil en aérospatiale, à finalité spécialisée en "aerospace engineering"
Année académique : 2023-2024
URI/URL : http://hdl.handle.net/2268.2/20391

Experimental and Numerical Analysis of Aerodynamic Forces on Small Caliber Projectiles in Supersonic Flows

Master's Thesis of
Sow Oumar

Master's Thesis submitted to the Department of Aerospace and Mechanical Engineering at the University of Liège in partial fulfilment of the requirements for the degree of Master of Science in Aerospace Engineering

---

Research project conducted within the
Department of Mechanics of the Royal Military Academy

Advisors: Prof. Dr. Ir. Thomas Andrianne, University of Liège
Prof. Dr. Ir. Benoît G. Marinus, Royal Military Academy

Academic Year 2023-2024

Members of the Master Jury

President
Prof. Dr. Grigorios DIMITRIADIS
University of Liège

Advisor
Prof. Dr. Ir. Thomas ANDRIANNE
University of Liège

Members
Prof. Dr. Ir. Benoît G. MARINUS
Royal Military Academy

Prof. Dr. Ir. Vincent E. TERRAPON
University of Liège

June 2024

Abstract

This thesis investigates the aerodynamic properties of the 5.56 mm NATO projectile using both experimental and numerical methods. Conducted in the Royal Military Academy's new wind tunnel, the study employs Simcenter STAR-CCM+ with the k-ω SST turbulence model for simulations validated by wind tunnel tests at Mach 2, 0° angle of attack, and a Reynolds number of 1.13×10^6. Key analyses include Schlieren visualization, wall static pressure measurements, and drag coefficient comparisons. The research addresses challenges such as instrument precision, setup asymmetry, and measurement uncertainties. Findings reveal a 10% discrepancy in drag coefficient between sting-mounted and confined free flight scenarios, with the confined free-flight scenario matching free-flight data. An asymmetry equivalent to an angle of attack of -0.32° was identified. The study also found that the projectile's contribution to the total drag of the setup was approximately 20%. Confidence in the wind tunnel's flow characteristics and instruments was established, providing a foundation for future aerodynamic studies. The insights gained will guide future experimental setups and improve the accuracy of aerodynamic measurements, paving the way for more refined and accurate future research.

Keywords :

Aerodynamics, Computational Fluid Dynamics, Wind Tunnel, 5.56 mm NATO.

Declaration of Artificial Intelligence Usage

This document has used ChatGPT for various tasks, including formatting original texts, translating, summarizing, and reformulating personal content. The Artificial Intelligence (AI) tools were employed in accordance with the guidelines set forth by the faculty's charter on AI usage.

Contents

Glossary

6/7-DoF High-fidelity trajectory models : 6-DoF (Degrees of Freedom) describes the motion of single rigid bodies in three-dimensional space, including translations and rotations. 7-DoF extends this by modeling projectiles with two coaxial rigid bodies that can spin independently, providing a more detailed analysis of their dynamic behavior [35, 135].. 14

AGARD-C Standard wind tunnel calibration model established by the North Atlantic Treaty Organization (NATO) Advisory Group for Aeronautical Research and Development (AGARD). The AGARD-C model extends the AGARD-B configuration by adding a 1.5-diameter-long body section and a T-tail, consisting of a horizontal and a vertical tail. This addition makes the model more sensitive to flow curvature and the influence of reflected shock waves in the wind tunnel test section. 40

AOP (NATO **A**llied **O**rdnance **P**ublication) are technical documents established under the cover of a reference STANAG. 12

artillery Large-caliber firearms, such as cannons, howitzers, and mortars, used for launching projectiles over long distances. These weapons are typically employed in support of ground forces (e.g., infantry) to deliver firepower against enemy positions, vehicles, or personnel. 16

ballistic coefficient Measure of a projectile's efficiency in overcoming air resistance during flight. It takes into account the bullet's mass, diameter, and drag coefficient. A higher ballistic coefficient indicates better aerodynamic performance, allowing the projectile to retain speed and stability over longer distances, thus enhancing accuracy and range. 12

caliber or cal. Largest diameter of the projectile. It is expressed in inches or millimeters. 2, 5

cannelure Indented groove around the bullet's circumference. It provides a secure grip for the cartridge case mouth when crimped onto the cannelure. This prevents the bullet

from shifting forward or backward within the case, ensuring stable seating and consistent performance during firing. 6

center of gravity or CG Point of application of the resultant of gravity forces (also considered as the center of mass, through which pass the principal moments of inertia). 23

center of pressure or CP Point of application of the resultant of aerodynamic forces. 23

indirect fire Fire delivered without direct line-of-sight to the target. It relies on calculated azimuth and inclination, often adjusted based on projectile trajectory observations (e.g., artillery, mortars, rocket, howitzer). 13

infantry Branch of the military composed of foot soldiers trained and equipped to engage in combat on foot. They typically use small arms and light weapons and play a crucial role in ground warfare operations. vii

muzzle conditions Initial state and behavior of a projectile immediately after it exits the barrel of a firearm. This includes the effects of the muzzle blast and the aerodynamic disturbances caused by the sudden transition from the controlled environment of the barrel to the open atmosphere. These conditions are characterized by high angular rates and yawing motion, often resulting in significant initial instability. As the projectile travels further, these disturbances, known as the muzzle effect, gradually dampen out, allowing the projectile to stabilize in flight. 7

S^4 (SG2 Shareable (Fire Control) Software Suite (S4)) developed by the NATO Army Armaments Group (NAAG) Integrated Capability Group Indirect Fires (ICGIF), it represents a suite of fire control software widely used within the international ballistics community and by fire-control system developers. It serves as a comprehensive solution for various shareable fire control applications and integrates multiple software components tailored for fire control. The Firing Tables and Ballistics Division within the Armaments Research, Development, and Engineering Center (ARDEC) serves as a focal point for its development and enhancement. 14

shell Projectile fired from a firearm with a diameter of 20 mm or more. Smaller projectiles are referred to as bullets. Despite this distinction, both shells and bullets are often colloquially referred to as bullets. 89

spotter Individual, often a trained observer or sniper's assistant, responsible for providing surveillance, target acquisition, and environmental analysis to support accurate shooting. In the context of long-range shooting, a spotter assists the shooter by observing the

target, estimating range, evaluating environmental conditions, and offering guidance for precise shot placement. They typically use specialized tools like rangefinders and weather meters to enhance accuracy. 14

STANAG (NATO **Stan**dardization **Ag**reement) establishes shared military and technical standards among member nations, fostering interoperability in procedures, equipment, and communications. STANAGs are available via the NATO Standardization Office (NSO) Website [1] (depending on security clearances). vii, 12

STANREC (NATO **Stan**dardization **Rec**ommendation) establishes document specifying one or more NATO or NON-NATO standards relevant for a specific activity of the alliances, but not related to interoperability. 14

tracer ammunition or tracers Projectiles that are built with a small pyrotechnic charge in their base. The latter ignites upon firing, creating a visible trace along the projectile's trajectory. This enables shooters to track the path and make ballistic adjustments, enhancing accuracy without relying on sights, especially in low-light conditions. 4

[1] https://nso.nato.int/nso/nsdd/main/standards

Chapter 1 | Introduction

1.1 History of NATO Standardized Cartridges

In the early 1950s, the North Atlantic Treaty Organization (NATO) initiated efforts to develop a standardized rifle cartridge suitable for use across all member nations within the North Atlantic Alliance to simplify logistics and ensure compatibility.

Initially, the **7.62x51 mm** NATO cartridge, heavily influenced by the United States, was adopted in 1954 due to its power and versatility. However, by the mid-1950s, it became evident that the 7.62x51 mm cartridge was too powerful and heavy for the evolving needs of modern warfare. This realization prompted the search for a smaller caliber cartridge. The .223 Remington emerged in 1957 as an experimental military cartridge and was officially adopted in 1964 as the **5.6 mm Ball M193**. This cartridge met the U.S. Continental Army Command's requirements for maintaining supersonic velocity and successful penetration of helmets at 500 yards (457 m), and compatibility with lightweight combat rifles.

Figure 1.1: FN Herstal 7.62x51mm NATO Cartridge [51].

In 1970, NATO members signed an agreement to select a second, smaller, caliber cartridge to replace the 7.62x51 mm NATO. The .223 Remington (M193) served as the basis for the new **5.56x45 mm** NATO cartridge, developed by FN Herstal and designated as SS109 in NATO and M855 in the U.S. This cartridge was standardized in October 1980, reflecting an international shift towards compact, lightweight, high-velocity military cartridges.

Since the adoption of the 5.56 mm NATO cartridge, the 7.62 mm has been somewhat overshadowed, making the 5.56 mm the most widely used ammunition worldwide. This widespread usage underscores the importance of studying its aerodynamic characteristics, making it a highly relevant subject for aerodynamics and ballistics research.

Additionally, ongoing research aims to develop a new intermediate cartridge that combines the advantages of both the 5.56 mm and 7.62 mm bullets [93, 126]. Even though an intermediate cartridge already exists (6.8 mm), it is not standardized yet. The 6.8 mm bullet, though promising, needs to undergo extensive testing and validation in various combat scenarios to ensure it meets all operational requirements and prove its superiority over existing calibers. Understanding the aerodynamic properties of the 5.56 mm NATO will provide valuable insights, as any new cartridge will need to match or exceed these characteristics to be effective in modern combat scenarios.

Modern Use of the 7.62x51 mm Cartridge

While the 7.62x51 mm cartridge (7.62 mm cal.) still serves in NATO countries, its application has shifted primarily to machine guns (Figure 1.2a) and sniper rifles (Figure 1.2b). Its virtues, including high stopping power, effective range, and armour-penetrating capabilities, are balanced by drawbacks such as increased recoil, higher weight, and production costs.

(a) FN MAG (Machine gun - 7.62 mm cal.) [52].

(b) SCAR-H PR (Precision rifle - 7.62 mm cal.) [53].

Figure 1.2: Modern applications of the 7.62x51 mm NATO ammunition. (a) Rapid Reaction Vehicle crews (RRV) of the Belgian 2nd battalion commando, and (b) Sniper of the Belgian Special Forces Group (SFG) [124].

1.2 Context and Motivations

The behaviour of a projectile in flight is significantly influenced by various environmental parameters such as pressure, temperature, air density, and humidity, as well as aerodynamic forces and moments. To facilitate the comparison of projectile performance, it is common to relate these forces and moments to their respective aerodynamic coefficients.

Several tools exist for initially estimating these coefficients, including numerical codes and wind tunnel tests. Following these initial estimations, it is essential to verify the projectile's behaviour through real flight conditions. There is a complementary relationship between numerical aerodynamic studies, wind tunnel tests, and field trials. Currently, live fire range tests data are often analyzed empirically, requiring an expert to iteratively adjust the aerodynamic coefficients and initial conditions in a flight simulation software to match observed flight data [27]. This method is laborious, time-consuming, and highly dependent on the expert's judgment. Consequently, considerable research is focused on developing methods to identify aerodynamic coefficients from flight test data [5, 27, 36]. These researches aim to derive aerodynamic coefficients directly from flight measurements, overcoming the limitations of empirical adjustments.

The primary methods for determining aerodynamic coefficients are :

- **Numerical Codes** : These codes fall into three categories. The first category allows for rapid calculations based on approximate models, suitable for parametric studies during the preliminary design phase. The second category uses semi-empirical methods combined with theoretical models or correlations from extensive databases, such as those from wind tunnel test campaigns. The third category comprises Computational Fluid Dynamics (CFD) codes, which are able to solve complex problems but require numerous calculations to represent an entire flight profile, as it consists of a succession of different flight scenarios.
- **Wind Tunnel Tests** : These tests determine aerodynamic coefficients by placing a scale model of the projectile in a controlled airflow. Wind tunnels offer flexibility by allowing variations in angle of attack, Mach number, and Reynolds number through pressure adjustments. However, wind tunnels only partially simulate real flight conditions and may disrupt the airflow around the projectile due to the mounting sting.
- **Live-Fire Tests** : These tests study projectile behaviour under real flight conditions. Currently, field test data analysis is empirical and arbitrary, involving iterative adjustments of aerodynamic coefficients and initial conditions in flight simulation software. This method is time-intensive and requires significant expertise.

Recently, the Royal Military Academy (Belgium) acquired a supersonic wind tunnel. The Department of Mechanics is conducting research to extract aerodynamic coefficients from wind tunnel tests, a goal shared by the Department of Ballistics, which faces its own challenges with experimental investigations in its 103.25 m indoor shooting range [114]. While wind tunnel tests provide reliable and repeatable results, it is relatively challenging in ballistic research due to factors such as barrel temperature variations, slight differences in standardized bullets, and changes in atmospheric conditions. Wind tunnel tests therefore offer significant advantages by allowing the reproduction of tests under consistent conditions. These facilities create a controlled environment to simulate various flight conditions. This enables researchers to move beyond much of the experimental methodology focused on managing environmental variables and concentrate on extracting the data of interest.

1.3 Objectives and Definition of the Framework

Objectives

The primary objective of this study is to determine the aerodynamic coefficients of the standardized 5.56x45 mm NATO projectile using both experimental and numerical approaches. The accurate prediction of these coefficients will allows for precise external ballistic calculations [35], as these coefficients significantly influence key performance metrics such as range, accuracy, and stability [13] (Figure 1.3).

Figure 1.3: Rapid Reaction Vehicle crews (RRV) of the Belgian 2nd battalion commando [102] equipped with GMG [61] chambered with tracers. This type of projectile is built with a small pyrotechnic charge in its base. When fired, it emits visible light, aiding shooters in tracking their trajectory and making real-time adjustments (especially in low-light conditions).

The study will employ a Force/Torque Sensor for experimental measurements and the commercial software STAR-CCM+ for numerical simulations. By combining these approaches, the study leverages the strengths of both methods to overcome their individual limitations. The findings will be validated against existing literature data.

In addition to determining the aerodynamic coefficients, this research will address the reliability, repeatability, and consistency of wind tunnel tests, which are critical for developing confidence in the new supersonic wind tunnel facility. A key objective also consists in establishing confidence in the measurements obtained from the wind tunnel instruments and the Force/Torque Sensor. Experimental data from wind tunnel tests will provide measurements of surface pressures, forces, and moments, which will be complemented by detailed numerical simulations to provide a comprehensive understanding of the aerodynamic characteristics of small-caliber supersonic projectiles.

Framework

The study focuses on the standardized 5.56x45 mm NATO projectile (Figure 1.4). The interpretation of this projectile's name is often confusing. It is important to clarify that the first number in the cartridge's name does **not** correspond to the bullet's caliber (cal.). Instead, it denotes the barrel diameter, which is slightly smaller than the one of the projectile. Using a slightly larger bullet diameter ensures a precise fit within the barrel, enhancing stabilization during flight. Additional information about bullet naming and stabilization can be found in Appendix A.

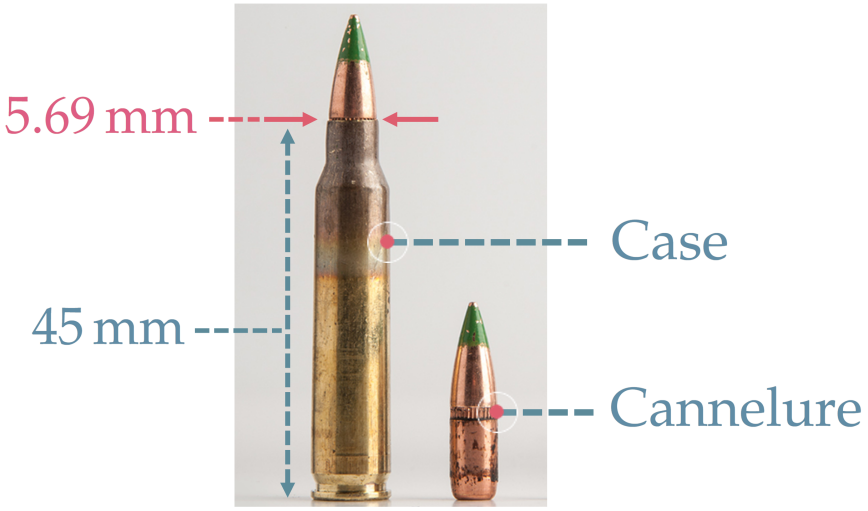

Figure 1.4: 5.56x45 mm NATO (M855) cartridge (left) and projectile (right), adapted from [6].

In modern bullets, a cannelure is indented into the bullet's circumference. However, the projectile was geometrically **simplified** by removing it. This simplification has been shown to effectively predict the aerodynamic characteristics of similar projectiles [121, 123, 130], although dynamic derivative and roll damping coefficients are more sensitive to striations [121, 123]. As these coefficients are not considered in this study, the simplification is justified. The geometry of the bullet is shown in Figure 1.5.

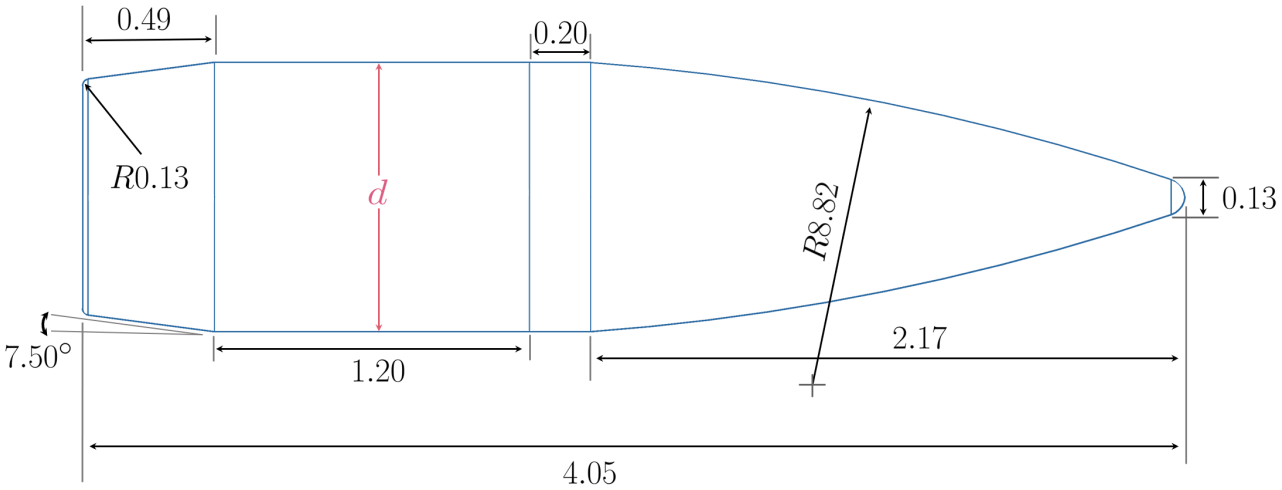

Figure 1.5: Dimensions of 5.56x45 mm NATO (M855), reproduced from [122]. All the dimensions are given in calibers $d = 5.69\,\mathrm{mm}$.

During the study, several other scales will be derived from the original geometry to discuss their potential influence on the results. The key dimensions of these projectiles are detailed in Table 1.1, with Scale 1 representing the original geometry.

Table 1.1: Key dimensions of the different projectile scales.

	Caliber [mm]	Length [mm]
Scale 1	5.69	23.04
Scale 1.5	8.53	34.56
Scale 2	11.38	46.08

Flight Scenario

The flight behaviour of small-caliber projectiles is well-known and can be effectively analyzed using software like PRODAS V3 [14]. Typical flight behaviour of small-caliber bullet is illustrated in Figure 1.6, where significant points are highlighted by small blue circles.

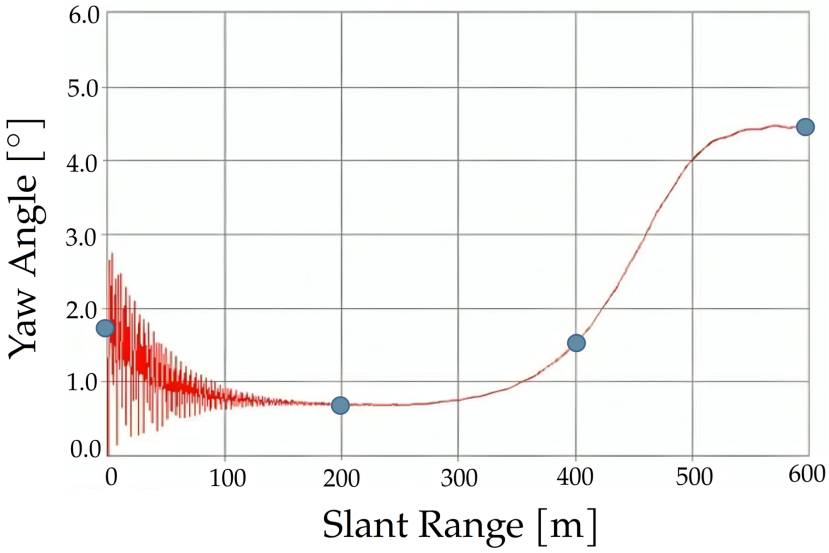

Figure 1.6: Yaw angle behaviour of small-caliber ammunition over its first 600 m of flight, adapted from [122].

The first point represents the muzzle conditions, where the projectile exits the muzzle with an angular rate that induces yaw. Due to the dynamic stability of the bullet, this yaw dampens over the first 100-150 meters of flight. The second point, at around 200 meters, is crucial for understanding the projectile's aerodynamic behaviour after the yaw has stabilized. Beyond this range, between 300 and 400 meters, dynamic instability begins, causing the yaw to increase. By 600 meters, a yaw limit cycle is expected to exist [122]. Table 1.2 lists the projectile's velocities at these various positions.

Table 1.2: Equivalent bullet locations with their corresponding Mach numbers, adapted from [122].

Location [m]	Mach [-]
0 (Muzzle)	2.6
200 m	2.2
400 m	1.7
600 m	1.2

Around 200 meters from the muzzle, the projectile is no longer affected by muzzle effects and enters its stable flight phase at Mach 2.2 with an angle of attack of less than one degree. For this study, the flight speed is approximated at Mach 2, and the negligible angle of attack is set to 0°. Focusing on a 0° angle of attack provides a baseline scenario with symmetrical flow over the bullet, simplifying the analysis and isolating key aerodynamic characteristics. This scenario closely mimics realistic operational conditions, ensuring the findings are directly applicable to practical use cases.

1.4 Structure of the Thesis

This thesis is structured to provide an investigation into the aerodynamics of the 5.56 mm NATO projectile using both numerical simulations and experimental methods. It begins with the **Introduction**, offering an overview of the study's objectives, significance, and the approaches employed, followed by a detailed outline of the thesis structure.

The **External Ballistics** chapter summarizes existing research on projectile ballistics and aerodynamics, reviews mathematical models, software, sensors, and numerical codes, and discusses methods for acquiring aerodynamic coefficients. This provides a solid foundation for understanding the context and background of the study.

The **Theoretical Background** chapter delves into the fundamental principles underlying the study. It covers the theoretical aspects of fluid dynamics, aerodynamic forces, and the specific computational and experimental methods used in this research. This chapter serves to ground the reader in the essential concepts that support the numerical and experimental investigations.

The **Experimental Investigation** chapter describes the experimental setup and procedures used to conduct the wind tunnel tests. This includes a detailed explanation of the equipment, data acquisition methods, and the process of measuring aerodynamic forces and pressures on the projectile. The chapter also addresses the challenges encountered during the experiments and the steps taken to mitigate these issues.

In the **Numerical Investigation** chapter, the computational setup and boundary conditions are described in detail. This chapter covers the meshing strategy, solver settings, and physical models used. Additionally, it presents complementary geometries examined to assess the influences of mounting and confinement on the projectile's aerodynamic behaviour.

The **Results and Discussion** chapter presents a detailed comparison between experimental results and numerical predictions to validate the numerical approach. This validation involves several key analyses, including Schlieren visualization, wall static pressure measurements, and drag coefficient comparisons. The chapter explores the implications of the force-balance mounting and bullet confinement on aerodynamic measurements and delves into the challenges associated with wind tunnel testing.

Finally, the **Conclusion** chapter summarizes the key findings from the numerical and experimental investigations. It discusses the implications of these results for future research and practical applications, and provides recommendations for further studies to enhance the understanding of projectile aerodynamics.

The thesis is supported by a list of **References** and additional technical details in the **Appendices**, such as the computation of uncertainties and detailed mesh quality assessments, along with supplementary figures and tables that support the main text.

Chapter 2 | External Ballistics

This chapter delves into the study of external ballistics, highlighting various techniques and methodologies aimed at understanding and predicting the flight behaviour of projectiles. It encompasses a comprehensive literature review, detailing existing research on projectile ballistics and aerodynamics, mathematical models, software tools, sensors, and numerical codes. The chapter further explores methods for aerodynamic coefficient acquisition, including both experimental and computational approaches. This examination provides a foundation for a better understanding of the context and background of the study.

2.1 Literature Review

The study of external ballistics (Figure 2.1) encompasses various techniques and methodologies aimed at understanding and predicting the flight behaviour of projectiles. In recent years, researchers and practitioners have employed diverse approaches to tackle the complexities of projectile motion in different environmental conditions.

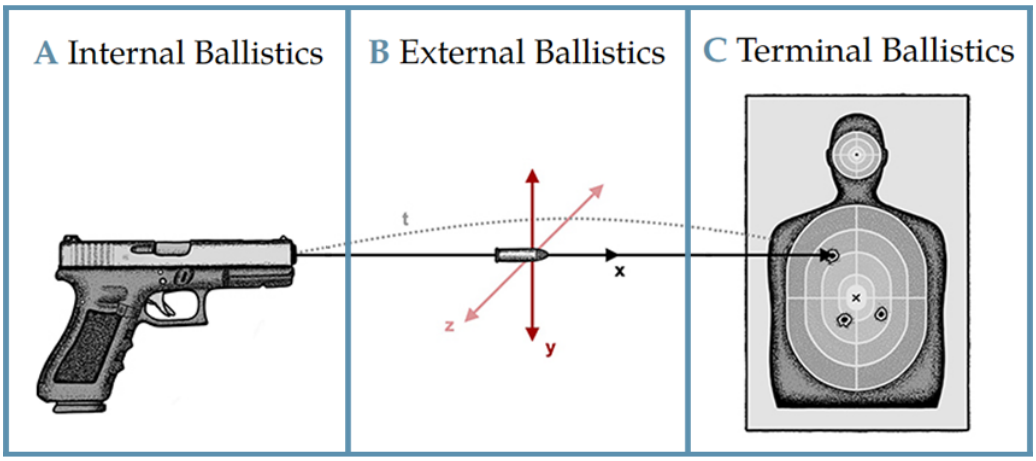

Figure 2.1: Different phases of Ballistics, reproduced from [19]. (A) Internal Ballistics takes place within the firearm. (B) External Ballistics covers the range after the projectile leaves the firearm and before it reaches the target. (C) Terminal or Wound Ballistics details the effects of the projectile once it has struck a target.

The characterization of an object flight behaviour using aerodynamic coefficients remains one of the most complex and extensively researched topics. Over recent decades, technological advancements have led to the development of experimental and theoretical methods for quantifying aerodynamic properties. Several tools are available for this purpose, including numerical codes, wind tunnel tests, and field trials. Each technique has its own set of advantages and disadvantages, but they can be used complementarily, forming a triangular exploration approach, as illustrated in Figure 2.2.

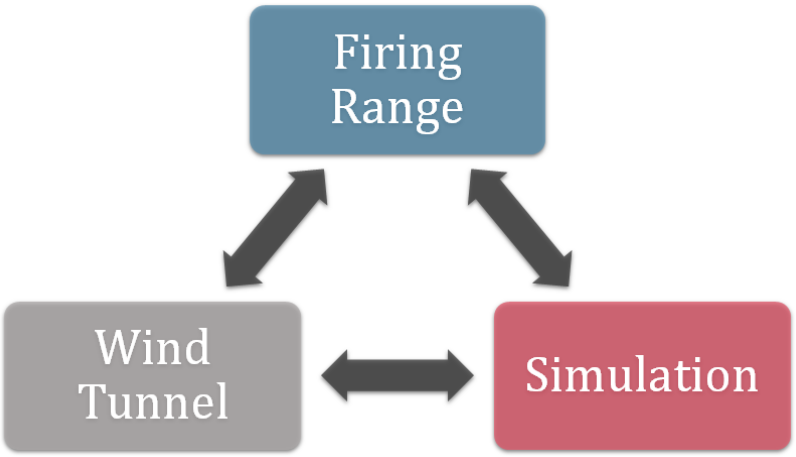

Figure 2.2: Triangular exploration approach for quantifying aerodynamic coefficients, reproduced from [5].

2.1.1 Mathematical models

One prominent avenue of research involves the development of **mathematical models** to describe the trajectory of projectiles. These models often integrate principles from classical mechanics and aerodynamics to simulate the effects of gravity, air resistance, and wind on the motion of the projectile. The following non-exhaustive list provides a brief overview of some of these mathematical models.

- **6-DoF Model & Numerical Integration Methods**

  This model uses Newton's laws for translational and rotational dynamics, requiring numerical integration methods like the fourth- or seventh-order Runge-Kutta scheme to solve its equations due to the absence of analytical solutions [36, 55, 77, 135].

- **Lieske-McCoy Model**

  Designed for rigid, rotationally symmetric projectiles, this model simplifies calculations compared to the 6-DoF model, making it suitable for symmetric bodies [68, 77].

- **Modified Point Mass Model (MPMM)**

  Extending the Lieske-McCoy approach, the MPMM simplifies calculations for dynamically stabilized projectiles, increasing the time step significantly [68, 69]. This model is standardized by NATO for spin-stabilized projectiles in STANAG/AOP-4355 [98, 99].

- **Point Mass Model (PMM)**

  The PMM simplifies trajectory calculations by assuming zero angle of attack and focusing on drag force [96]. Standardized in STANAG 4355, this model is effective for small-caliber and short-range applications [131].

- **Siacci's Method & Ballistic Coefficient Models**

  Using the ballistic coefficient (BC), this method simplifies trajectory calculations for flat-fire trajectories [77, 111]. The BC is defined as the ratio of the projectile's sectional density SD to its shape factor i (Equation 2.1). It is a key parameter in Ballistics, assessing the projectile's performance by accounting for both mass and drag. A higher BC indicates better aerodynamics, meaning the bullet retains speed more effectively and is less influenced by wind and gravity. Including mass is crucial because heavier bullets maintain momentum better, reducing drag impact and enhancing long-range accuracy. The G1 and G7 standards are commonly used, with the G7 providing a more accurate representation for modern long-range bullets [21, 35].

$$\text{BC} = \frac{SD}{i} = \frac{m/d^2}{C_D/C_G}\,, \tag{2.1}$$

  where the mass, the diameter, and the drag coefficient of the projectile are given by m, d, and C_D respectively, and where C_G is the drag coefficient of a **standard** projectile.

Many sniper teams use equipment based on the Siacci method, which can be field-calibrated for practical use. This highlights the importance of accessible aerodynamic data for practical applications. *Applied Ballistics*, developed by Bryan Litz, exemplifies this approach, primarily grounded in the definition of the ballistic coefficient [70, 71].

2.1.2 Numerical methods

Advancements in Computational Fluid Dynamics (CFD) have also contributed to the study of external ballistics. By employing **numerical methods** to solve the Navier-Stokes equations, researchers can simulate the flow around a projectile with high fidelity.

- *This method will be further explored in Chapter 3.*

2.1.3 Experimental techniques

Furthermore, **experimental techniques** play a crucial role in validating theoretical models and refining computational simulations. Yaw cards, Doppler radar systems, and instrumented test ranges enable researchers to observe and measure the flight characteristics of projectiles in real-time. These experimental data provide valuable benchmarks for assessing the accuracy of computational models.

- *This method will be further explored in Section 2.2.*

2.1.4 Software Tools and Calculators

In addition to theoretical and experimental approaches, specialized **software tools** and **calculators** have facilitated practical applications of external ballistics. These tools offer convenient means of predicting bullet trajectories based on user-provided input parameters. Below is a non-exhaustive list of existing software.

- **ARFDAS (Aeroballistic Research Facility Data Analysis System)**
  - Developed by the United States Air Force Aeroballistic Research Facility (ARF).
  - Used for determining aerodynamic coefficients from spark range experimental data and analyses of 6-DoF ballistic trajectories reconstructed from free flights [47].
  - Regularly used by the Army Research Laboratory in sessions on firing ranges [122].
- **PRODAS (Projectile Design and Analysis System)**
  - Commercial Software originated at General Electrics in 1972 and further developed by Arrow Tech Associates Incorporated [1] since 1991 [38].
  - Uses a 6-DoF core and semi-empirical functions for determining aerodynamic coefficients, and allows for rapid evaluation of ammunition characteristics.
- **NABK (NATO Armaments Ballistic Kernel)**
  - Component of the NATO Army Armaments Group AC/2252 [2] and based on STANAGs 4355 [96] and 4500 [94].
  - Performs ballistic computations to support indirect fire (howitzers, mortars, etc).
  - Integrated into operational cannon artillery fire control systems in service with the United States Army and Marine Corps [129].

[1] https://arrowtechassociates.com/
[2] https://diweb.hq.nato.int/naag/Pages/default.aspx

- **BALCO (Ballistic Code)**
  - Computer code implemented under cover of STANREC-4618 [95] and AOP-50 [134].
  - Standardizes high-fidelity 6/7-DoF trajectory models for conventional and precision-guided projectiles [97].
  - Developed by the Franco-German Institut Saint-Louis (ISL) and distributed to the S^4 NATO Community.

2.1.5 Integrated Sensor Technologies

The **integration of sensor technologies** into firearms and optics has enhanced real-time data acquisition and analysis. Tools like rangefinders with ballistic calculators, atmospheric sensors, and wind meters enable shooters to adjust their aim based on precise, real-time data. Here are two practical examples illustrated below.

- **Rangefinders with Ballistic Calculators**

  Rangefinders such as the *Leica Rangemaster CRF 2800.COM* (Figure 2.3) offer a compact solution for precision shooting. They feature Bluetooth connectivity for pairing with devices like the *Kestrel Elite weather meter*, allowing for quick and accurate firing solutions via *Applied Ballistics* software [11, 12].

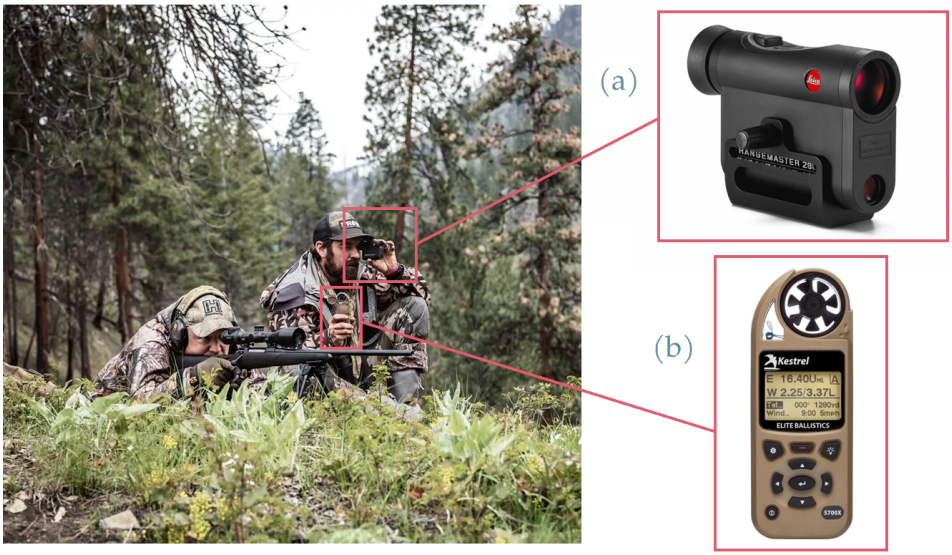

Figure 2.3: Real-time weather conditions measured by the spotter (right) to provide precise shot placement guidance for the shooter (left). (a) Leica Rangemaster CRF 2800.COM [66, 67] for precise distance measurements and (b) Kestrel Elite Weather Meter for real-time weather data and ballistics calculator [65].

- **Ballistic Calculator Integration**

  FN Elity has developed a ballistic calculator for FN SCAR-H PR precision rifles (Figure 2.4). This calculator considers range, wind, and environmental conditions to provide accurate ballistic solutions, enhancing precision and effectiveness.

Figure 2.4: FN Elity Weapon Ballistic Calculator [48, 50] composed of a ballistic solver with aeroballistic profiler from *ApexO* (AFS®) [10] and multiple sensors. It is here mounted on a SCAR-H PR [53].

2.2 Coefficients Acquisition Process

The importance of aerodynamic coefficients in accurately predicting trajectories and providing precise firing elements during operational phases has been emphasized in the concepts discussed so far (Section 2.1). Whether using a comprehensive 6-DoF model or a lighter MPMM model, these coefficients play a crucial role, minimizing the need for costly experiments. Projectile aerodynamics present unique challenges in the direct extraction of forces and moments coefficients, particularly when dealing with small projectiles. This section outlines the most common techniques employed to acquire these coefficients, covering both **Experimental measuring techniques** (live-range tests and wind-tunnel experiments) and **Software simulation techniques** (Computational Fluid Dynamics and Semi-Empirical Interpolation).

2.2.1 Test Shooting Range

The method commonly employed for studying long and high trajectories (artillery) is the test shooting range, also known as full-scale firing. This method was widely used when simulation techniques were less available and is still used nowadays [5, 27, 81, 136]. It involves various instruments such as muzzle velocimeters, Doppler radar, optical instrumentation, high-speed photography, and yaw measuring systems like yaw cards. Additionally, software like ARFDAS are used for trajectory reconstruction and coefficient extraction [47].

Instrumentation

As just introduced, there are numerous instruments available for acquiring aerodynamic coefficients. However, it has been decided to delve into the detailed explanation of only two of them.

- **Doppler Radar**

  Doppler radar measures bullet position, velocity, and drag deceleration by transmitting a radar beam and analyzing the frequency shift of the reflected beam due to the bullet's motion (Figure 2.5). This **highly effective** method is **costly** and requires **specialized facilities** and **expertise**, limiting its availability mainly to military sites. Annual tests at the U.S. Army Yuma Proving Ground have used Doppler radar for measuring ballistic coefficients under the Association of Firearm and Toolmark Examiners (AFTE) [24].

Figure 2.5: Experimental setup featuring a shooter, Doppler radar system, and the Hornady [3] engineering team conducting ballistic coefficient measurements [54].

[3] https://www.hornady.com/

- **Yaw Card**

  The yaw card method uses panels made of materials like paraffin, paper, or cardboard placed along the projectile's trajectory to capture imprints without disturbing its flight (Figure 2.6). These imprints provide data on roll velocity, position, and angles like pitch and yaw [30, 36, 86]. This method is considered as the most **economical** and **least sophisticated** of all measuring techniques for aerodynamic coefficients, yet it **remains** widely used [86].

Figure 2.6: Yaw cards at the DGA Tt shooting range in Bourges (FRA) during tests for Nexter Munitions [4] [36].

2.2.2 Aeroballistic Ranges

Aeroballistic Ranges, also known as Spark Ranges, represent experimental facilities designed for in-depth investigations into the aerodynamic behaviour of projectiles in flight (Figure 2.7). This method relies on the acquisition of multiple sequences of shadowgraphs, where two orthogonal cameras concurrently capture the projectile's velocity and orientation during flight. The subsequent application of sophisticated image processing techniques and computer algorithms enables the automated calculation of angles, facilitating the extraction of aerodynamic coefficients. Particularly effective for studying small to medium yaw angles, this approach has been fundamental in aerodynamic research.

[4] https://www.knds.fr/en/our-brand/nexter-munitions

Figure 2.7: Defence Research and Development Canada (DDRC) Valcartier Aeroballistics Range [31]. It houses a sophisticated 250 m instrumented firing tunnel capable of firing projectiles ranging from 5.56 mm to 155 mm at speeds of up to Mach 7. This state-of-the-art facility features 54 orthogonal indirect shadowgraphs (equivalent to 108 cameras) and four stations for Schlieren flow visualization.

2.2.3 Wind-Tunnel Experiments

In wind tunnel tests, **force balances** are used for the **Direct Force Measurement** of aerodynamic forces and moments acting on the model within the test section [89–91]. These force balances come in various types, ranging from one-component balances that measure a single force (e.g., lift) to more sophisticated three-component and six-component balances capable of measuring multiple forces (lift, drag, side force) and torques (pitch, roll, yaw).

Balance types are categorized based on the number of force/moment components measured simultaneously **and** their placement, distinguishing between *internal* and *external* balances [127].

- **Internal Force Balance**

  Placed **within** the model, the internal balance eliminates interference in the wind flow caused by its components (Figure 2.8) [88]. However, they require a mechanical support structure for the model (referred to as a *sting*), ensuring its stability within the test section and facilitating orientation changes. Given the high complexity associated with internal installation, this option **lacks flexibility** in testing various models.

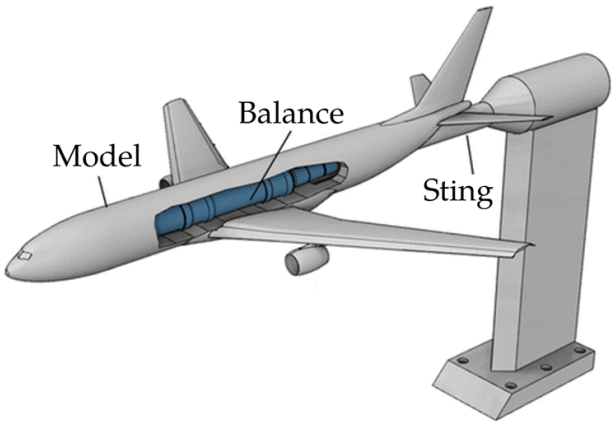

Figure 2.8: Internal Force Balance, adapted from [25]. The internal balance is located within the model, and connected to the sting.

- **External Force Balance**

  External balances can be positioned either outside or inside the wind tunnel test section, but consistently introduce some level of **interference** in the wind flow (Figure 2.9) [87]. Despite this interference, the advantage lies in the ease of changing test models, offering a **high degree of flexibility** to the wind tunnel facility. The complexity of these balances varies depending on the number of measurement channels, which can range from one to six [60]. *Strain gauge load cells* [5] are commonly used due to their quality, accuracy, and reliability [63].

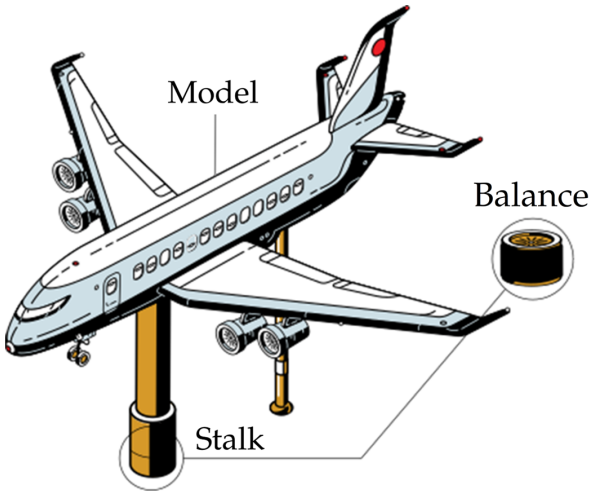

Figure 2.9: External Force Balance, adapted from [63]. The external balance is mounted in the floor of the wind tunnel, and connected to the scaled model by a "stalk" [64].

[5] A load cell is a force gauge that consists of a transducer that is used to create an electrical signal whose magnitude is directly proportional to the force being measured [108]. One type of load cell is the *Strain gauge*.

Note : In wind tunnel measurements, the presence of a sting (a rod or support structure holding the model) can introduce aerodynamic interference, potentially affecting force measurements. Despite potential uncertainties, wind tunnel facilities often employ techniques and corrections to ensure accurate measurements of aerodynamic forces, particularly drag, on tested projectiles. The influence of the sting on these measurements will be studied in this research to better understand and mitigate its effects.

Challenges for Small-Size Models

While the literature has extensively covered the topics of internal [18, 26, 34, 43, 74, 92, 104, 128] and external force balances [4, 45, 46, 57, 73, 112], challenges persist in measuring the aerodynamic forces of small-size model.

In general, the internal balance solution is preferred for this type of application because it does not disturb the flow, which is particularly crucial for small-size models. For small-caliber projectiles such as the 5.56 mm ammunition, challenges arise due to space limitations within the projectile that restrict the deployment of sensors. The literature emphasizes the necessity for advancements in sensor technology and measurement techniques. Innovative solutions involve the use of miniaturized sensors, such as MEMS (Micro-Electro-Mechanical Systems), strategically placed within the projectile for size compatibility and integration into confined spaces.

Despite advancements in sensor technology resulting in increasingly smaller sensors, there currently exist no sensors small enough to fit within the studied projectile. Therefore, one of the objectives of this thesis is to integrate an **external** force balance in the experimental setup to obtain the aerodynamic forces and moments applied to the projectile.

Although internal balances are preferred because they ensure that the desired measurements are not obscured by spurious contributions from disturbances induced by the force balance itself, the supersonic nature of the flow offers a distinct advantage for balance placement. Specifically, if the flow remains supersonic in the region of interest, downstream elements will not perturb the measurements. This inherent property of supersonic flows ensures more reliable data acquisition, providing greater confidence when using an external balance.

2.2.4 Computational Fluid Dynamics (CFD)

While this approach requires less equipment and practical implementation, a deeper understanding of fluid mechanics is essential. Therefore, this method will be further explained in Chapter 3, dedicated to Fluid Dynamics.

2.2.5 Semi-Empirical Interpolation Codes

Semi-empirical interpolation codes are used for predicting aerodynamic coefficients by interpolating among simplified theories or tabulated aerodynamic data for typical projectile designs and shapes. Various component-build-up techniques involve predicting coefficients by summing aerodynamic properties calculated for different parts of the projectile. Several notable semi-empirical interpolation codes include:

- **McDrag**
  - Developed by Robert McCoy and detailed in [75].
  - Suitable for determining zero-yaw drag coefficients for spin-stabilized projectiles.
  - Estimates drag coefficient to within 3% error at supersonic speeds, 11% error at transonic speeds, and 6% error at subsonic speeds.
  - Valid over a Mach number range from 0.5 to 5 and a projectile diameter range from 4 to 400 millimeters.
- **MISSILE**
  - Developed by ONERA (FRA) in the 1990s [103].
  - Estimates aerodynamic characteristics of missiles up to Mach 10.
  - Combines semi-empirical and theoretical methods, along with correlations from missile databases [36].
- **AeroFI**
  - Produced for the Finnish Army Material Command Headquarters [100, 116] and available to NATO members.
  - Used for creating aerodynamic input data for firing table computations and preliminary projectile design.
  - CFD computations are also implemented to complement some of the predictions.

2.3 Conclusion & Discussion on External Ballistics

Conclusion on External Ballistics

The chapter on External Ballistics has provided a comprehensive overview of the diverse techniques and methodologies employed to understand and predict the flight behaviour of projectiles. The exploration of mathematical models, numerical methods, experimental techniques, software tools, and integrated sensor technologies, underscores the multidisciplinary nature of external ballistics research.

Mathematical models, such as the 6-DoF model, Lieske-McCoy model, Modified Point Mass model, and Point Mass model, enable the calculation of projectile trajectories by incorporating principles from classical mechanics and aerodynamics. Numerical methods, like the Runge-Kutta scheme, facilitate the resolution of complex equations, offering a balance between accuracy and computational cost.

Experimental techniques, including test shooting ranges, aeroballistic ranges, wind tunnel experiments, and the use of specialized software tools (ARFDAS, PRODAS, NABK), play a crucial role in validating theoretical models and refining numerical simulations. These techniques provide valuable benchmarks for assessing accuracy and identifying areas for improvement.

The integration of sensor technologies into firearms, exemplified by Rangefinders with Ballistic Calculators and Ballistic Calculator Integration in firearms like the FN SCAR-H PR, allows real-time data acquisition and analysis in the field, enhancing shooting accuracy.

Additionally, the challenges posed by small-size models, especially for the 5.56 mm ammunition, highlight the need for innovative solutions in measurement techniques.

Finally, CFD and semi-empirical interpolation codes offer versatile alternatives to experimental methods, emphasizing the importance of combining theoretical models with experimental data for accurate trajectory computation.

The upcoming chapter will delve into the fundamental principles of *Fluid Dynamics*, laying the groundwork for a deeper understanding of the CFD method and its application in studying projectile aerodynamics.

Chapter 3 | Theoretical Background

This chapter aims to present the essential theoretical concepts to understand the aerodynamics associated with the analysis of the flow around the 5.56x45 mm bullet in a supersonic wind tunnel.

3.1 Basics of Fluid Dynamics

3.1.1 Main Dimensionless Freestream Parameters

Working with dimensionless quantities is advantageous, as it simplifies complex relationships and reduces experimental efforts. For a body at a given angle of attack α the resultant aerodynamic force R depends on freestream velocity V_∞, density ρ_∞, fluid viscosity μ_∞, body size (characteristic length l), and compressibility (speed of sound a_∞). Figure 3.1 illustrates this scenario.

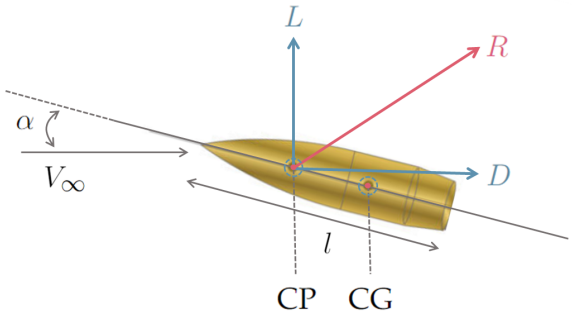

Figure 3.1: Resultant aerodynamic force R applied on the Center of Pressure (CP), which is offset from the Center of Gravity (CG) (adapted from [118]).

A general functional relation (Equation 3.1) is too complex for direct calculation. The application of the *Buckingham Pi theorem* streamlines equations, resulting in a reduced number of independent variables. This dimensional analysis reduces the number of variables from five to two : the **Reynolds number** and the **Mach number** (Equations 3.2 and 3.3). This simplification allows to efficiently vary parameters in wind tunnel tests, saving time and costs while capturing the essential flow behaviour. Without dimensionless quantities, the process

would involve systematically varying individual parameters.

$$R = f(\rho_\infty, V_\infty, l, \mu_\infty, a_\infty) \tag{3.1}$$

- The (freestream) **Reynolds number** is a measure of the ratio of inertia forces to viscous forces in a flow (Equation 3.2).

$$Re = \frac{\rho_\infty V_\infty l}{\mu_\infty}\,. \tag{3.2}$$

- The (freestream) **Mach number** is the ratio of the flow velocity to the speed of sound (Equation 3.3).

$$M = \frac{V_\infty}{a_\infty}\,. \tag{3.3}$$

These quantities can also be defined locally. For the local Reynolds number, the characteristic length is replaced by the longitudinal coordinate along the surface, and density, velocity, and viscosity are evaluated at the point of interest. Similarly, local flow velocity and local speed of sound are used to compute the local Mach number.

3.1.2 Flow Similarity

Flow similarity refers to the **dynamic similarity** of two flow, which is achieved when bodies and boundaries are geometrically similar, and Reynolds number Re and Mach number M are consistent [82]. This concept enables accurate wind-tunnel testing by ensuring that measurements such as lift, drag, and moment coefficients match those in real-world conditions, provided Re and M **match** those of the free flight scenario. However, other factors like freestream turbulence and blockage ratio, defined as the model's proportion of the test section's cross-sectional area, can affect aerodynamic testing accuracy. Managing these factors is crucial for maintaining validity in wind-tunnel simulations of free-flight conditions.

3.2 Projectile Aerodynamics

Aerodynamic Forces & Moments

A primary focus of this thesis is the study of the aerodynamic forces and moments acting on the projectile. These effects are quantified using established formulas with predetermined aerodynamic coefficients (see Section 2.2). While aerodynamic forces and moments can be classified as static or dynamic, this study specifically examines static ones.

For a **symmetric** projectile in straightforward motion and **excluding** angular rotations around its center of gravity, the primary static forces are **drag** and **lift**. These forces act at the center of pressure, distinct from the center of gravity. By convention, this distance is constant and equal to the projectile's caliber [35]. Consequently, these forces induce a **pitching moment** around the center of gravity. Figure 3.2 illustrates these forces and moment for a positive pitching moment. Equations 3.4-3.6 (taken from [35]) provide the expressions for lift, drag, and pitching moment, respectively.

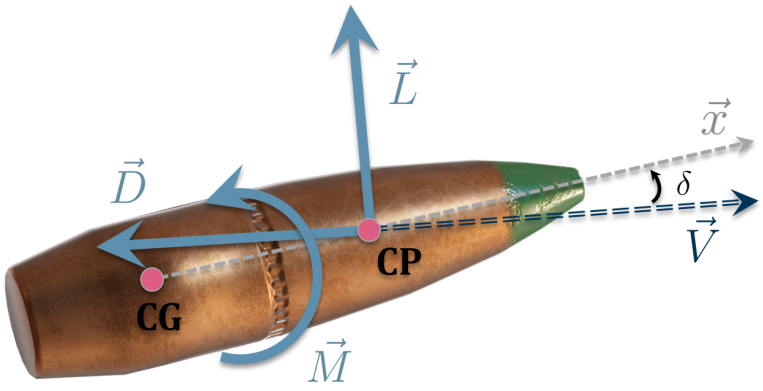

Figure 3.2: Static forces and moment on a projectile during motion at velocity $\vec{V}$ and angle of attack δ (adapted from [20]). Drag $\vec{D}$ and Lift $\vec{L}$ forces act at the center of pressure (CP), inducing a Pitching Moment $\vec{M}$ around the center of gravity (CG). The distance between CG and CP is intentionally exaggerated for the sake of clarity.

Static Aerodynamic Forces and Moment

$$\vec{D} = -\frac{1}{2}\rho V^2 \cdot \frac{\pi d^2}{4} \cdot C_D \cdot \vec{e}_V \,, \tag{3.4}$$

$$\vec{L} = \frac{1}{2}\rho V^2 \cdot \frac{\pi d^2}{4} \cdot C_{L_\delta} \cdot \left[\vec{e}_V \wedge (\vec{e}_x \wedge \vec{e}_V)\right] , \tag{3.5}$$

$$\vec{M} = \frac{1}{2}\rho V^2 \cdot \frac{\pi d^2}{4} \cdot d \cdot C_{M_\delta} \cdot (\vec{e}_x \wedge \vec{e}_V) \,, \tag{3.6}$$

where

- d is the projectile caliber.
- $\vec{e}_V$ is the unit vector in the direction of the velocity $\vec{V}$.
- $\vec{e}_x$ is the unit vector in the direction of the x-axis.

Complete expressions of the aerodynamic coefficients (C_D, C_{L_δ} and C_{M_δ}) are given by Equations 3.7-3.9 (taken from [35]).

Static Aerodynamic Coefficients

$$C_D = C_{D_0} + C_{D_{\delta^2}} \sin^2 \delta \,, \tag{3.7}$$

where

- C_{D_0} is the zero-yaw drag coefficient derivative.
- $C_{D_{\delta^2}}$ is the quadratic-yaw drag coefficient derivative.

$$C_L = C_{L_\delta} \sin \delta = C_{L_{\delta_0}} \sin \delta + C_{L_{\delta_3}} \sin^3 \delta \,, \tag{3.8}$$

where

- C_{L_δ} is the lift force coefficient derivative.
- $C_{L_{\delta_0}}$ is the zero-yaw lift force coefficient derivative.
- $C_{L_{\delta_3}}$ is the quadratic-yaw lift force coefficient derivative.

$$C_M = C_{M_\delta} \sin \delta = C_{M_{\delta_0}} \sin \delta + C_{M_{\delta_3}} \sin^3 \delta \,, \tag{3.9}$$

where

- C_{M_δ} is the pitch moment coefficient derivative.
- $C_{M_{\delta_0}}$ is the zero-yaw pitch moment coefficient derivative.
- $C_{M_{\delta_3}}$ is the quadratic-yaw pitch moment coefficient derivative.

Note: Coefficient derivatives, exemplified by $C_{D_{\delta^2}}$, illustrate how coefficients like drag C_D respond to changes in parameters such as yaw angle δ. They capture dependencies on factors like Mach number and angle of attack. In ballistics, C_{D_0} accounts for Mach number dependency, while $C_{D_{\delta^2}}$ incorporates yaw angle effects. For symmetric projectiles, lift force is zero at an angle of attack of 0°and can be approximated by a cubic function for large angles. While insignificant for small projectiles like the 5.56 mm, cubic dependencies become essential for larger ones due to high elevation angles [35]. Similarly, pitch moment derivatives indicate the sensitivity of the pitch moment to flight conditions (e.g., Mach number and yaw angle).

3.3 Supersonic Wind Tunnel

The main types of supersonic wind tunnels include blowdown, indraft, pressure-vacuum, and closed-circuit continuous flow [84]. However, the discussion will only focus on the ***blowdown*** *supersonic tunnel, since it is the type available at the Royal Military Academy.*

3.3.1 Blowdown Supersonic Wind Tunnel

A blowdown wind tunnel (Figure 3.3) operates by storing high-pressure air in a tank at its entry. When testing begins, a valve is opened, allowing air to flow from the tank through the tunnel. As air flows out of the tank, its total pressure and temperature decrease. Therefore, due to decreasing pressure in the tank, test times in blowdown tunnels are limited. Intermittent wind tunnels, such as blowdown tunnels, are favoured for their simplicity in design and construction, making them popular choices for academic institutions. However, their limited running times can restrict the amount and type of data collected. In contrast, continuous flow supersonic tunnels are larger, more expensive, and typically found in government laboratories [106].

Moreover, blowdown tunnels offer high Mach capability and are more cost-effective, yet they necessitate pressure regulator valves which adds complexity to the system and requires careful calibration to maintain stable conditions, and may be noisy during operation [85].

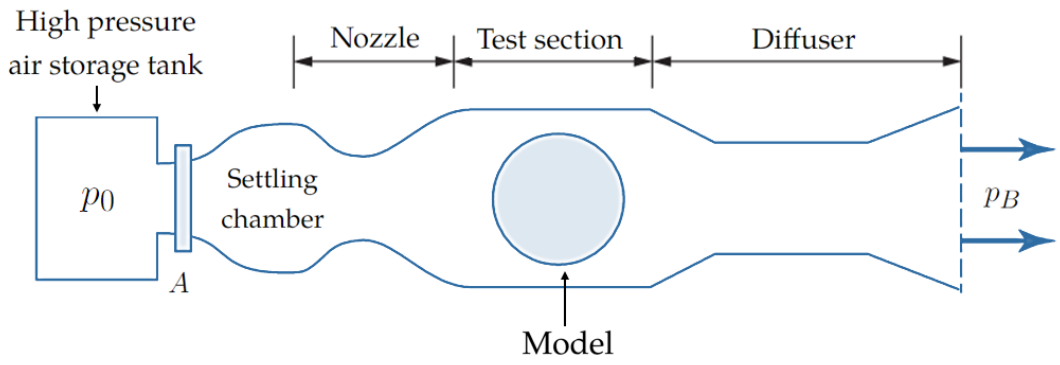

Figure 3.3: Sketch of blowdown supersonic tunnel, reproduced from [9].

3.3.2 Supersonic Flow Visualization

Schlieren photography is a widely used technique in wind tunnel testing for visualizing airflow. More precisely, it captures real-time images of **density changes** in the fluid, with darkened lines indicating areas of refracted light due to density gradients.

This method uses a light source, lenses, and a pinhole to generate a point-like light source. Placing the pinhole at the focal point of the first parabolic mirror results in a collimated beam of light that passes through the wind tunnel test section. A second parabolic mirror focuses the light beam onto a knife edge, and the resulting image is captured by a camera. This setup is depicted in Figure 3.4.

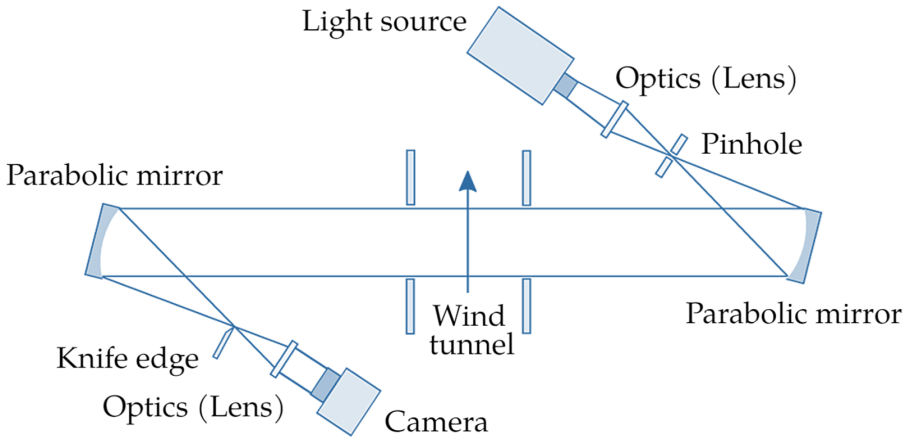

Figure 3.4: Z-Type Schlieren System setup, reproduced from [58].

The knife edge, which typically obstructs half of the incoming light when the wind tunnel is inactive, becomes a key element during operation. **Density gradients** in the fluid cause **deflection of light rays**, and depending on the knife-edge orientation, deflected rays are either allowed to pass or blocked. Consequently, density variations manifest as either *white* or *black* features in the Schlieren visualizations. In supersonic flow studies, shock waves are visualized as **dark lines** (Figure 3.5).

The sensitivity of the Schlieren system is influenced by the pinhole size. While an infinitely small pinhole would offer maximum sensitivity, it is not practical, as even minor density gradients would either completely block or allow the passage of light rays. To balance sensitivity and practicality, finite-sized pinholes are employed, enhancing the measurement range for flow visualization [58].

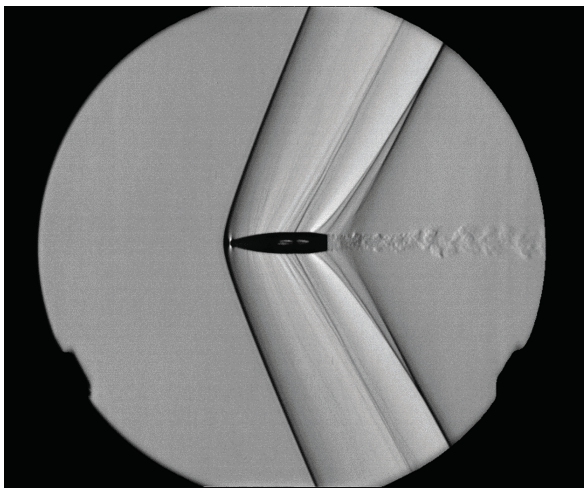

Figure 3.5: Single frame from a Schlieren image sequence showing a .50 caliber M33 (Ball) bullet [49] travelling at Mach 1.1, taken from [22].

3.4 Viscous Compressible Flow

'At large Reynolds numbers, one can consider external flow to be inviscid almost everywhere, except in a thin region adjacent to the body surface, called the boundary layer, and in the wake behind the body'. Ludwig Prandtl1, 1904 [8, 107].

3.4.1 RANS Modelling

The turbulence inside the wind tunnel's test section will be modelled using the Reynolds Averaged Navier-Stokes (RANS) approach. This method employs Reynolds and Favre averaging to decompose variables such as density ρ and velocity u_i into mean and fluctuating components [72, 137]. Reynolds averaging is used for density and pressure (Equation 3.10), while Favre averaging is applied to other quantities (Equation 3.11), yielding a set of equations known as the RANS equations (Equations 3.12-3.14, taken from [72]).

Reynolds and Favre averaging methods

$$\rho(x,t) = \overline{\rho}(x,t) + \rho'(x,t)\,. \tag{3.10}$$

$$u_i(x,t) = \widetilde{u}_i(x,t) + u_i''(x,t)\,. \tag{3.11}$$

Reynolds Averaged Navier-Stokes Equations (RANS Equations)

$$\frac{\partial \overline{\rho}}{\partial t} + \frac{\partial(\overline{\rho}\tilde{u}_j)}{\partial x_j} = 0\,, \tag{3.12}$$

$$\frac{\partial(\overline{\rho}\tilde{u}_i)}{\partial t} + \frac{\partial(\overline{\rho}\tilde{u}_i\tilde{u}_j)}{\partial x_j} = -\frac{\partial \overline{p}}{\partial x_i} - \frac{\partial \overline{\rho u_i'' u_j''}}{\partial x_j} + \frac{\overline{\tau}_{ij}}{\partial x_j}\,, \quad i = 1,2,3 \tag{3.13}$$

$$\begin{aligned}\frac{\partial(\overline{\rho}\tilde{e_0})}{\partial t} + \frac{\partial(\overline{\rho}\tilde{u}_j\tilde{e_0})}{\partial x_j} = \frac{\partial}{\partial x_j}\left(-\tilde{u}_j\overline{p} - \overline{\rho u_j'' h''} + \overline{\tau_{ij}'' u_i''} - \overline{1/2\rho u_j'' u_i'' u_i''}\right) \\ + \frac{\partial}{\partial x_j}\left[\tilde{u}_i(\overline{\tau_{ij}} - \overline{\rho u_i'' u_j''})\right]\,,\end{aligned} \tag{3.14}$$

with ρ the density, x_j the spatial coordinate in the j-direction, u_i the velocity component in the i-direction, p the pressure, $e_0 = e + 1/2\rho u^2$ the total internal energy, τ_{ij} the deviatoric stress tensor (Equation 3.15), and h the enthalpy.

$$\tau_{ij} = \mu\left(\frac{\partial u_i}{\partial x_j} + \frac{\partial u_j}{\partial x_i}\right) - \frac{2}{3}\mu\delta_{ij}\frac{\partial u_k}{\partial x_k}\,, \quad k = 1,2,3\,. \tag{3.15}$$

The terms highlighted in *softpink* in Equations 3.13 and 3.14 are known as **Reynolds stresses**. This term must be modelled in order to close the system, as well as extra terms known as the turbulent heat flux vector $\overline{\rho u_j'' h''} + \overline{\tau_{ij}'' u_i''} - \overline{1/2 \rho u_j'' u_i'' u_i''}$ in Equation 3.14.

These terms are the source of the **closure** problem, necessitating additional to close the system.

3.4.2 Boussinesq Assumption

The Boussinesq assumption, or Turbulent Viscosity Hypothesis, models turbulence by relating Reynolds-stress components to mean velocity gradients through an **isotropic scalar** defined as the turbulent viscosity ν_t. Despite its simplification as an isotropic scalar, this assumption is effective for shear flows dominated by a single turbulent shear stress component [35].

Boussinesq assumption

$$-\overline{\rho u_i'' u_j''} = \nu_t \left(\frac{\partial u_i}{\partial x_j} + \frac{\partial u_j}{\partial x_i} \right) - \frac{2}{3} \left(\rho k + \nu_t \frac{\partial u_k}{\partial x_k} \right) \delta_{ij} \,, \tag{3.16}$$

with ν_t the turbulent viscosity and k the turbulent kinetic energy (TKE).

3.4.3 k-ω SST Model

The k-ω Shear Stress Transport (SST) model, introduced by F.R. Menter [79], will be used in the Numerical Investigation to close the Reynolds stresses. This model is based on the Boussinesq assumption and combines k-ε and k-ω models using a blending function based on the flow region. This hybrid model improves the prediction of flow separation in adverse pressure-gradient boundary layers and resolves the free-stream sensitivity issue of the original k-ω model [41]. It also introduces two new transport equations for turbulent kinetic energy k and specific dissipation rate ω.

3.5 Conclusion on Theoretical Background

Conclusion on Theoretical Background

This chapter provides essential theoretical concepts for understanding the aerodynamics of the 5.56x45 mm bullet in a supersonic wind tunnel. It covers the basics of fluid dynamics, highlighting the importance of dimensionless parameters like Reynolds and Mach numbers to simplify complex relationships and reduce experimental efforts. Flow similarity principles are discussed to ensure dynamic similarity between wind tunnel models and real-world conditions. Projectile aerodynamics are examined, focusing on static aerodynamic forces and moments such as drag, lift, and pitching moment, using aerodynamic coefficients.

The chapter also describes the operation of blowdown supersonic wind tunnels, which the Royal Military Academy uses, explaining their advantages and limitations. Supersonic flow visualization techniques, such as Schlieren photography, are introduced to capture real-time density changes in the fluid, crucial for visualizing shock waves.

Turbulence modelling is addressed using the Reynolds Averaged Navier-Stokes (RANS) approach, involving Reynolds and Favre averaging to decompose variables into mean and fluctuating components. The Boussinesq assumption is employed to relate Reynolds-stress components to mean velocity gradients, providing an effective method for modelling turbulence. The chapter concludes with the introduction of the k-ω Shear Stress Transport (SST) model, which combines k-ε and k-ω models to improve flow separation predictions and resolve free-stream sensitivity issues.

In summary, this chapter lays the groundwork for analyzing the aerodynamic performance of the 5.56x45 mm bullet in supersonic conditions by integrating fluid dynamics principles, wind tunnel testing methodologies, and turbulence modelling.

This chapter concludes the essential groundwork required for the proper approach to this thesis. The next chapter will mark the beginning of the core study, focusing on Experimental and Numerical determination of forces and moments on the 5.56 mm NATO projectile in the supersonic wind tunnel from the Royal Military Academy.

Part I

Experimental and Numerical Determination of Aerodynamic Forces

Chapter 4 | Experimental Investigation

The experimental investigation detailed in this chapter was conducted using the advanced wind tunnel facility at the Royal Military Academy. This chapter describes the setup and execution of experimental procedures aimed at validating the numerical models developed in this study. It covers the critical components and operational capabilities of the wind tunnel, the methodologies employed for surface pressure and aerodynamic force measurements, and the various design considerations for ensuring accurate and reliable data. Emphasis is placed on the importance of achieving consistent and repeatable test conditions, given the inherent challenges associated with free-flight testing.

4.1 Wind Tunnel Facility

The Royal Military Academy (RMA) wind tunnel facility is a state-of-the-art blowdown supersonic wind tunnel (Figure 4.1) with a 2×2 inch (5.08×5.08 cm) test section spanning 7.25 inches (18.41 cm). One of the key features of this wind tunnel is its electronically controlled variable displacement nozzle block, which allows for precise adjustments of the Mach number within the range of $1.4 < M < 3.6$. This capability enables to simulate a wide range of supersonic flow conditions relevant to military applications.

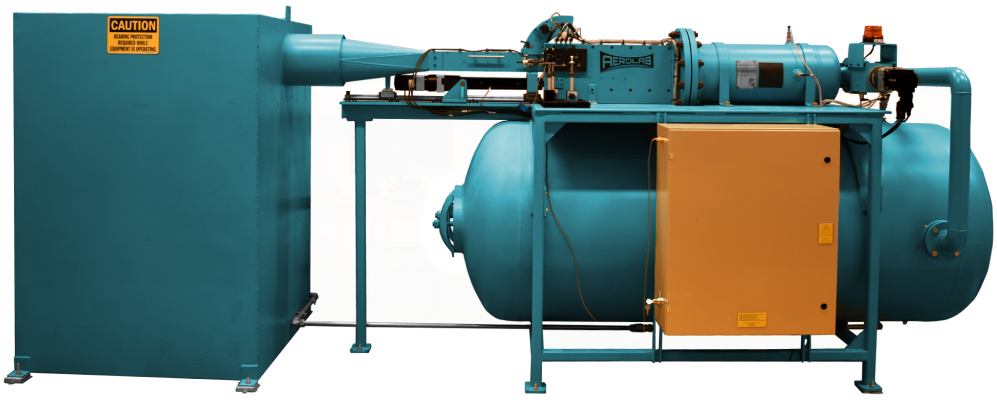

Figure 4.1: Supersonic wind tunnel of the Royal Military Academy (RMA).

The operation of the wind tunnel can be explained based on the following components, as illustrated in Figure 4.3.

- **Supply tank** : Stores compressed dry air delivered to the wind tunnel conduits. Dry air is crucial to prevent moisture condensation. As the flow expands in the nozzle, the temperature decreases, which can lead to condensation of moisture in the test section.
- **Stagnation tank** : Following the supply tank, the compressed air encounters the regulating valve, known as the *butterfly*, which precisely adjusts the airflow entering the tunnel according to operational requirements and reservoir conditions. After passing through the butterfly, the airflow enters the stagnation chamber, serving as an immediate air reservoir for the wind tunnel. The stagnation chamber includes two flow conditioning components : a *porosity plate* and three *turbulence-reducing screens*.
- **Test section** : The high-pressure air is then accelerated through a *converging-diverging nozzle* to attain the desired speed at the test section inlet. The converging-diverging nozzle, located upstream of the test section, features a variable throat area. Using a *sliding-nozzle-block* design, the wind tunnel allows adjustment of the lower block's position with respect to the upper block, as depicted in Figure 4.2. This design ensures that the test model, positioned downstream in the test section, encounters the intended supersonic speed.

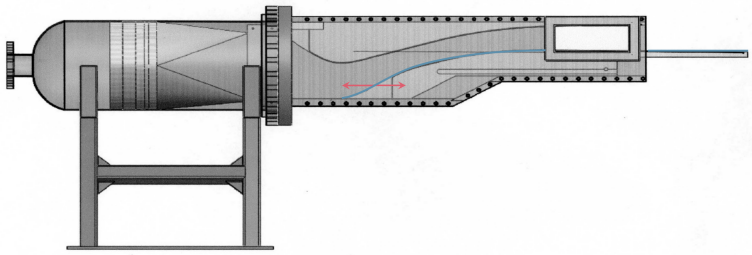

Figure 4.2: Moving lower nozzle block, highlighting the lower block position in blue and the sliding directions in soft pink(taken from [37]).

- **Diffusers** : Upon exiting the test section, the airflow proceeds to the first exit diffuser, commonly referred to as the *supersonic diffuser*. Here, it may decelerate to subsonic speeds after passing through one or a series of shock waves. Subsequently, in the second exit diffuser, known as the *subsonic diffuser*, the airflow undergoes further deceleration, reaching lower velocities at the outlet.

- **Silencer** : To minimize aerodynamic noise, an exhaust silencer is employed after the diffusers and before the airflow re-enters the atmosphere.

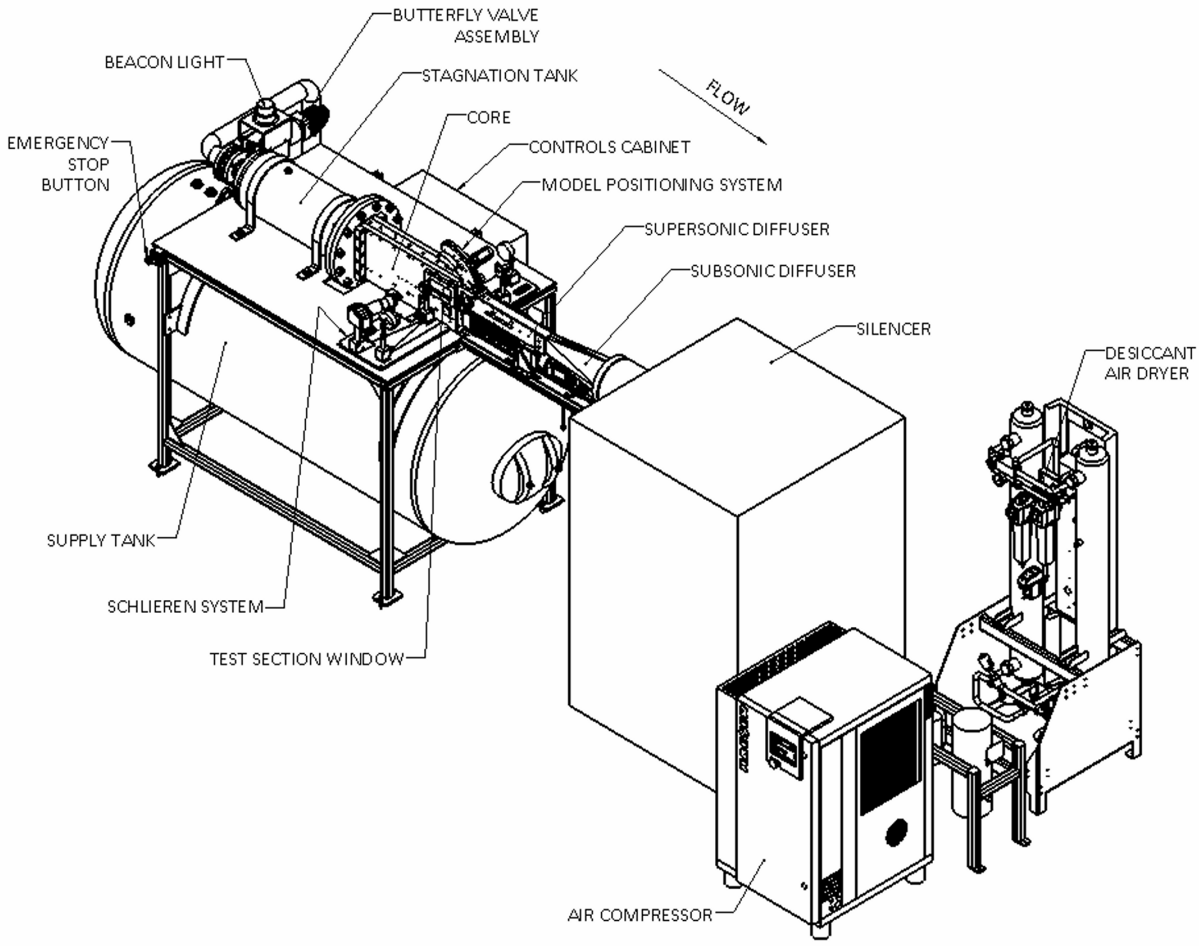

Figure 4.3: Wind Tunnel General Layout, taken from [3].

More details regarding the dimensions of the wind tunnel are provided in Appendix B.

4.2 Control and Capability

The wind tunnel operation is managed by a Programmable Logic Controller (PLC), which interfaces with MATLAB-based PC software (Figure 4.5) for control, data acquisition, and configuration. Specifically, it controls components such as the model positioning system, the nozzle block linear actuator, and the butterfly valve.

- **Model Positioning**: This system allows for setting the pitch angle of the test model while maintaining a **constant** centerline height.

- **Nozzle Block Linear Actuator**: As shown in Figure 4.4, it controls the position of the lower nozzle block (adjustable from 0 to 100%) based on the target Mach number. This position is solely and entirely determined by the Mach number.

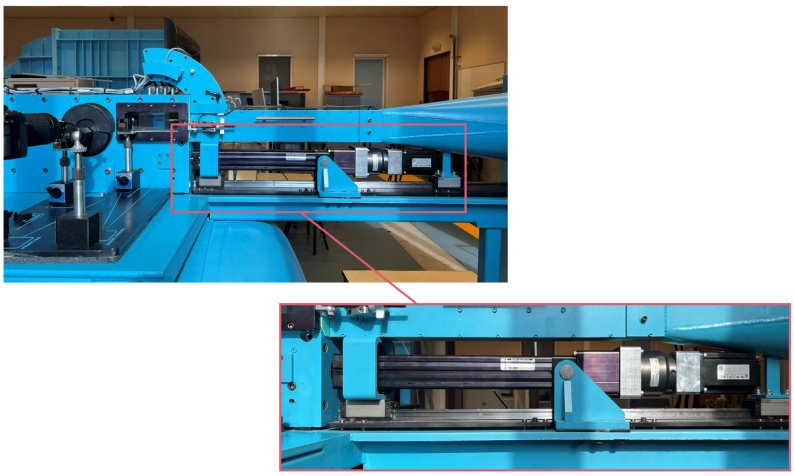

Figure 4.4: Close-up view of the linear actuator controlling the position of the lower nozzle block.

- **Butterfly Valve**: This component maintains the user-set target total pressure during runs.

Figure 4.5: AeroStream Control Interface, taken from [3].

To achieve steady supersonic speeds in the test section, the chamber pressure must be sufficiently high to eliminate the starting shockwaves in the tunnel [37]. Therefore, when setting the target Mach number on the AeroStream software, the suggested target total pressure is the minimum required to reach the prescribed speed (Figure 4.6a) with a shock-free test section. For a given Mach number, this pressure is computed using the following equation :

Stagnation Tank Pressure

$$\frac{p_0}{p} = \left(1 + \frac{\gamma - 1}{2} M^2\right)^{\frac{\gamma}{\gamma - 1}}, \quad \text{with} \quad \frac{p_0}{p} = \frac{p_{SC}}{p_{TS,1}} \tag{4.1}$$

and where p_0 is the total pressure in stagnation chamber, p is the static pressure, M is the (target) Mach number, γ is the specific heat ratio, p_{SC} is the pressure measured in the stagnation chamber and $p_{TS,1}$ is the static pressure measured at the furthest upstream wall part in the test section [a].

[a] The wind tunnel is equipped with an absolute pressure transducers to monitor four static pressures along the top wall of the test section [3].

After each run, the "plot last run wind data" button (Figure 4.5) allows for the verification of whether the target conditions have been met. This feature provides plots of upstream pressure, upstream temperature, test section pressure (from the four pressure taps on the test section top wall), Mach number, and main valve position. Verifying these conditions is a best practice adopted during testing.

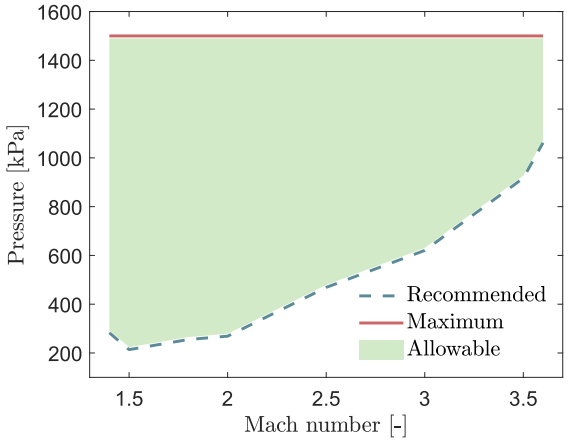

(a) Recommended pressure.

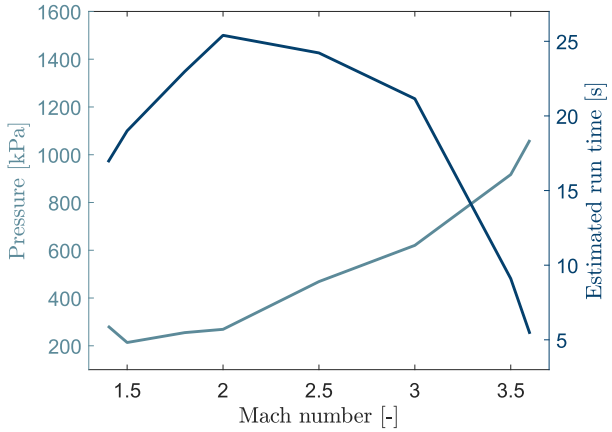

(b) Estimated run time.

Figure 4.6: Operational wind tunnel conditions for different Mach number. (a) Pressure map of recommended and allowable pressures and (b) Evolution of running time with the recommended pressure.

Figure 4.6b allows for discussion of the practical capacity of wind tunnel measurements. For speeds close to Mach 3.5, the test time is very limited, and it is more challenging to reach a stationary state. Therefore, achieving the conditions required for stationary measurements becomes increasingly complicated.

Given that the target velocity in this study is Mach 2, Figure 4.6a suggests a recommended pressure of **268 kPa**. Consequently, this pressure has been used for all wind tunnel tests conducted. Additionally, Figure 4.6b predicts a run time of 24 seconds, provided the tank is fully charged.

4.3 Reynolds Number Consideration

When testing in a wind tunnel, it is usually desirable to achieve free-flight conditions by matching the Reynolds number. Since it is intended to keep the same flight speed for the three different scales of the 5.56 NATO projectile, the Reynolds number should be adjusted by varying the pressure.

However, since this is a new wind tunnel at the RMA with newly integrated measurement setups (for pressure and force/moment extraction), it was decided to perform **all** the tests at the **lowest allowable pressure** prescribed by the AeroStream software. This cautious approach mitigates risks associated with high-pressure operations. As a result, the three different scales will have different Reynolds number when tested. However, as the critical Reynolds number is exceeded, the flow is fully turbulent, making the influence of the Reynolds number on aerodynamic coefficients less significant. Additionally, the design itself of these projectiles aims to maintain a consistent drag coefficient (and ballistic coefficient) over a wide range of Reynolds numbers [21, 80]. Therefore, moderate changes in Reynolds number due to variations in air density and viscosity do not significantly impact the drag coefficient.

Moreover, it has been proven that this hypothesis is relevant in a similar study conducted at Mach 2.4 with the same projectile and at 1.24 times the live-range Reynolds number [39]. It was determined that the Reynolds number falls within a reasonable range of dynamic similarity, with the Mach number being the most critical factor for this flow regime.

To illustrate the variation in Reynolds numbers between free-flight and wind tunnel conditions, the following table presents the Reynolds number based on the length of projectiles (Table 3.2). The free-flight scenario is computed under standard atmospheric conditions, while the wind tunnel scenario is computed with an imposed pressure of 268 kPa (recommended by AeroStream software at Mach 2) and a total pressure of 300 K.

Table 4.1: Reynolds number based on the length of projectiles in free-flight and wind tunnel conditions. The free-flight scenario is computed under standard atmospheric conditions, while the wind tunnel scenario is computed with an imposed pressure of 268 kPa and a total pressure of 300 K.

	Free-Flight	**Wind Tunnel**		
	Scale 1	Scale 1	Scale 1.5	Scale 2
$Re_L \times 10^6$ [-]	1.08	0.76	1.13	1.51

4.4 Choice of the Reference Projectile

Given the relatively small dimensions of the test section in the wind tunnel, it is important to evaluate the blockage ratios of the various calibers a priori planned for the experiments (Figure 4.7).

Figure 4.7: Three different scales of the 5.56 mm NATO bullet.

The *blockage ratio* refers to the ratio of the cross-sectional area of a test model A_{model} to the cross-sectional area of the wind tunnel test section A_{wt} (Equation 4.2). It indicates how much the model obstructs the flow of air in the tunnel. A smaller blockage ratio is preferred, as it minimizes disruption to airflow and ensures more accurate measurements. Generally, a blockage ratio between 5 and 10% [29, 133] is considered acceptable for supersonic wind tunnels. Table 4.2 outlines the blockage ratios induced by each of the three projectiles.

Wind Tunnel Blockage Ratio

$$\text{Blockage Ratio} = \frac{A_{\text{model}}}{A_{\text{wt}}}\,, \tag{4.2}$$

with

$$A_{\text{wt}} = 50.8 \cdot 50.8 = 2580.64\,\text{mm}^2\,.$$

Table 4.2: Blockage ratios of the different bullet scales.

	Caliber [mm]	Frontal area [mm^2]	Blockage ratio [%]
Scale 1	5.69	25.43	0.98
Scale 1.5	8.535	57.21	2.22
Scale 2	11.38	101.71	3.94

Another evaluated parameter concerns the presence of the sting at the rear of the model. While the sting minimizes interference with the model's flow field [83], it still affects the wake region behind the projectile. Typically, this interference can lead to discrepancies with the free-flight scenario as the wake region cannot develop freely at the rear of the projectile, which is especially true for small projectiles. The *linkage ratio* serves to assess this obstruction at the rear of the model. It is defined as the ratio between the cross-sectional area of the sting A_{sting} to the base section of the projectile A_{base} (Equation 4.3). Table 4.3 outlines the linkage ratios induced by each of the three projectiles.

Model Linkage Ratio

$$\text{Linkage Ratio} = \frac{A_{\text{sting}}}{A_{\text{base}}}\,, \tag{4.3}$$

with

$$A_{\text{sting}} = \frac{\pi \cdot 4.5^2}{4} = 15.9043\,\text{mm}^2\,.$$

Table 4.3: Linkage ratios of the different bullet scales.

	Base Caliber [mm]	Base area [mm^2]	Linkage ratio [%]
Scale 1	4.73	17.55	90.59
Scale 1.5	7.09	39.50	40.26
Scale 2	9.45	70.22	22.65

Experimental investigations have highlighted that in the presence of a turbulent boundary layer at the base of the model, the critical length of a sting (beyond which its influence on the flow around the model is negligible), is from 3 to 5 model base diameters [105]. This observation remains relatively unaffected by variations in Reynolds number [105]. Furthermore, it is advised that the diameter of the sting should not exceed approximately 30% of the model base diameter. Nonetheless, in wind tunnels subject to high dynamic pressures,

achieving this ratio may be impractical due to the substantial aerodynamic forces leading to undesirable deflections or stresses in the sting. In such scenarios, the use of shorter stings with larger relative diameters becomes necessary.

A practical rule of thumb is that to ensure minimal aerodynamic interference, particularly in wind tunnels characterized by high Reynolds numbers and dynamic pressures, the diameter d of the sting should ideally range from 30% to 50% of the model base diameter D. Additionally, the sting should have a length L of at least three times the diameter of the model base. These specifications align closely with the recommendations outlined for the AGARD-C calibration model [105].

When considering these two aspects together, it becomes apparent that selecting the most suitable projectile for analysis in the present study involves a trade-off. As depicted in Figure 4.8, the lower the blockage ratio of a projectile, the higher its linkage ratio tends to be. Therefore, since at this stage of research conducted at RMA, there is no intention yet to investigate the effects associated with excessively high blockage and linkage ratios, it was decided to opt for the **Scale 1.5** as the reference model. The latter emerged as the most optimal model for the intended purpose of this study.

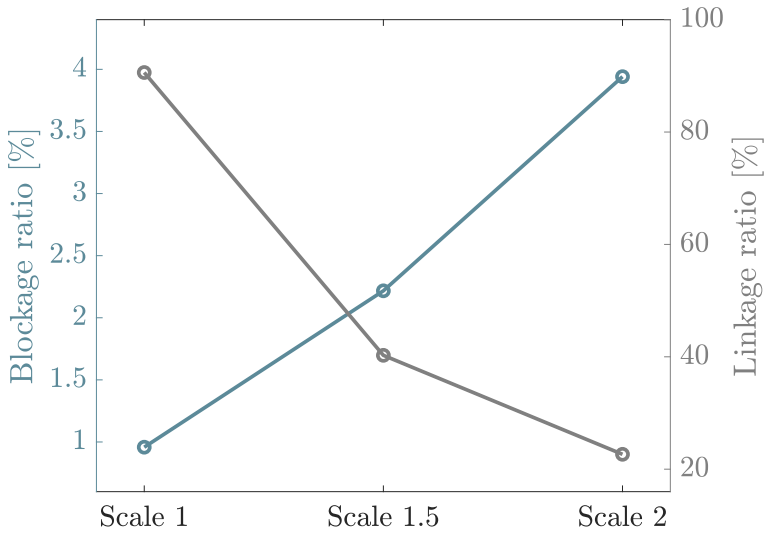

Figure 4.8: YY plot showing the relationship between blockage ratio and linkage ratio for different bullet scales, highlighting the necessary compromise to balance these factors effectively.

All analyses conducted throughout the remainder of this study will be performed using the 1.5-scale projectile, whose key characteristics are outlined below.

Reference Projectile

Scale 1.5: $d = 8.535\,\text{mm}$ and $L = 34.56\,\text{mm}$.

The bullet coordinate reference frame used in this study is depicted in Figure 4.9.

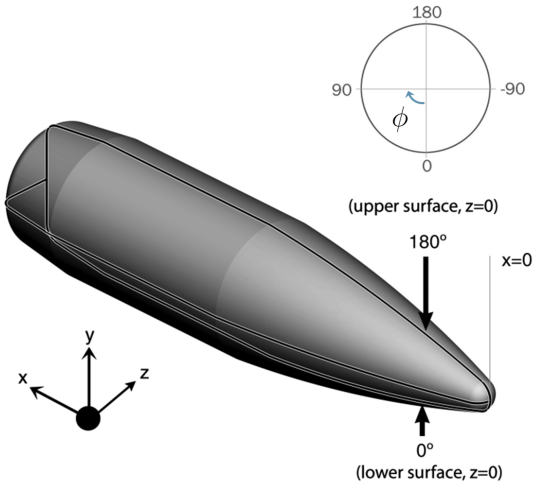

Figure 4.9: Bullet coordinate reference frame, adapted from [39].

4.5 Surface Pressure Measurements

Pressure data were obtained from ten pressure taps made of 1 mm holes communicating with pressure tubes. These tubes were inserted inside the model through holes in its base, glued in place. The locations of the pressure taps are shown Figure 4.10 and listed in Table 4.4.

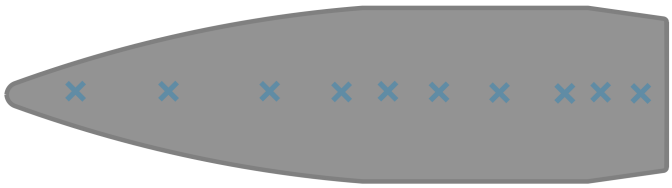

Figure 4.10: Pressure tap locations.

Table 4.4: Non-dimensional locations of the ten pressure taps.

	Tap									
	1	2	3	4	5	6	7	8	9	10
x/L [-]	0.1	0.25	0.4	0.51	0.57	0.65	0.75	0.85	0.91	0.97

To avoid interference from an excessive number of holes on the projectile surface, it was decided to measure a maximum of **four** pressures per model. Consequently, to obtain pressure readings for the 10 pressure taps, **three identical** models of the projectile at a 1.5 scale were used. The first one has four pressure tap on the *ogive*, the second, four on the *cylinder*, and the third, two on the *boat-tail* (see Figure 4.11). The arrangement of the pressure tap locations for the three models is as follows: top-bottom-left-right. Figure 4.12 illustrates the positions of the first four pressure taps, as well as the ducts used to measure the wall static pressure. While the same methodology was applied to the second model (4 taps on the *cylinder*), for the last model (only 2 taps on the *boat-tail*), the positions were limited to the top and bottom surfaces.

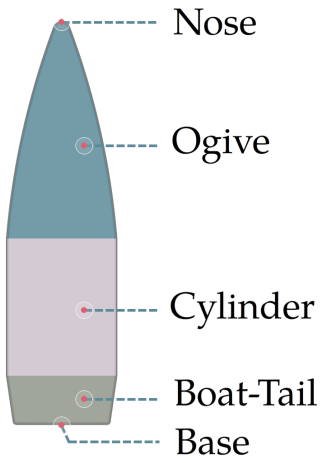

Figure 4.11: Geometric sections of the 5.56 mm bullet.

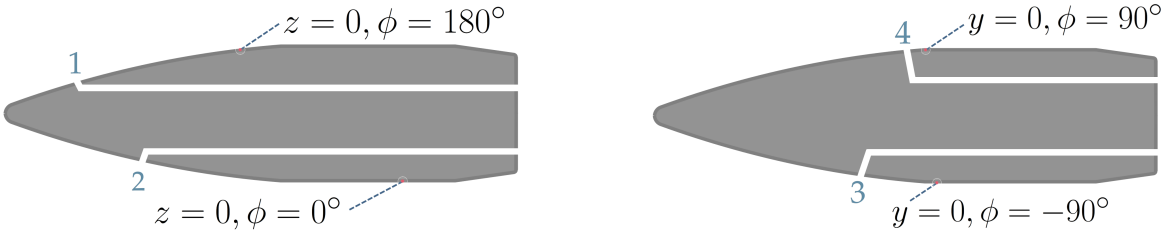

(a) First and second pressure tap ducts.

(b) Third and fourth pressure tap ducts.

Figure 4.12: Pressure ducts of the first four pressure taps.

In practical terms, these three projectiles were 3D printed using the *Formlabs Form 3+* 3D printer [1]. The material used was Formlabs Grey Resin and the models were printed with 100 µm thick layers (detailed characteristics of the resin are provided in Appendix C). The base of each projectile includes 4 (or 2) outlet holes to insert metal pressure tubes. Additionally, the base is perforated to allow a screw to fix the projectile to the sting (Figure 4.13). Yellow tape was used to secure the pressure metal tubes to the sting.

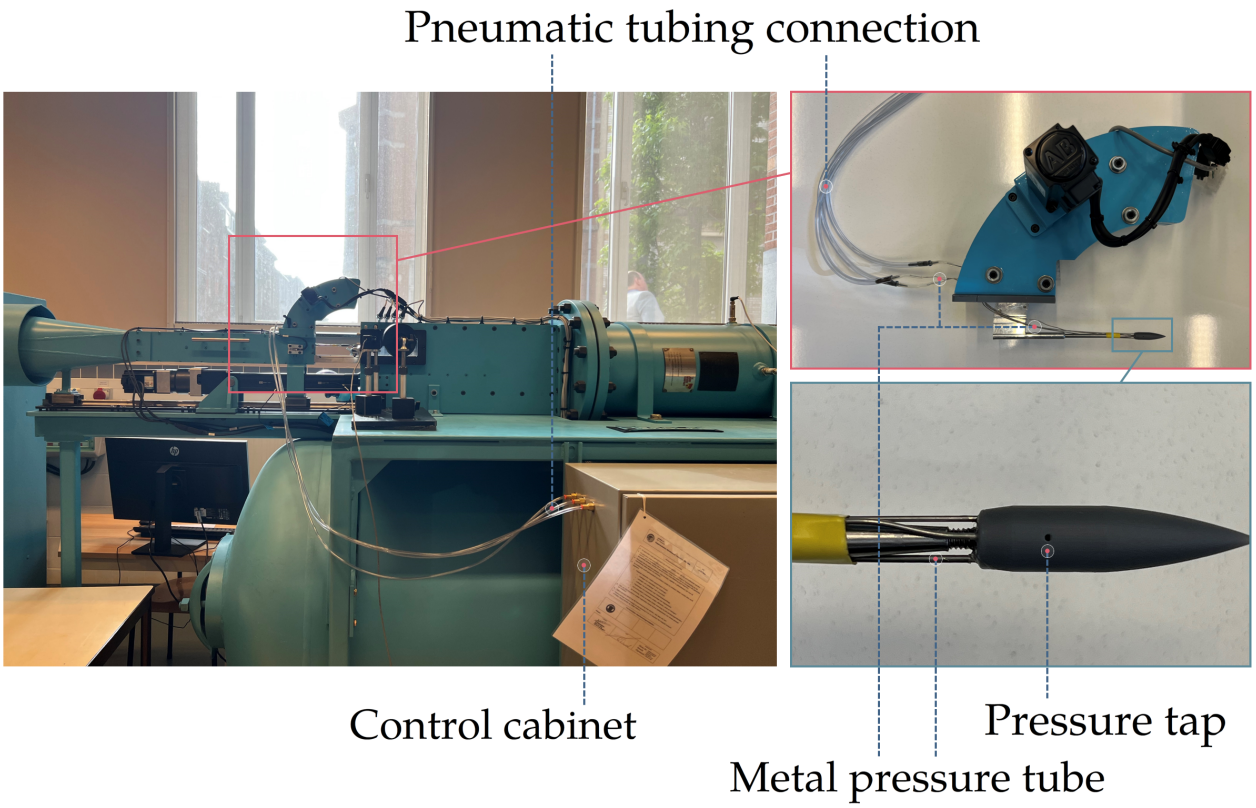

Figure 4.13: Experimental setup for pressure measurement.

Wall Static Pressure Extraction Procedure

The process of extracting pressures along the projectile's wall is relatively straightforward. Once the tubing is checked for leaks and the setup is installed in the tunnel, the tank can be filled. The test is then conducted for 6 to 10 seconds, allowing for the collection of sufficient steady data. At the end of the test, it is important to verify if the target conditions (such as Mach number) have been achieved before proceeding to post-process the obtained data and initiating another test. This procedure is illustrated in Figure 4.14.

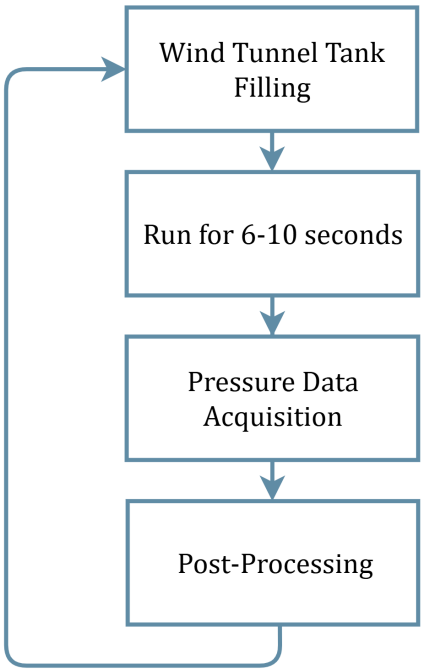

Figure 4.14: Workflow diagram for pressures acquisition procedure.

4.6 Aerodynamic Force Measurements

Aerodynamic forces were obtained from a sensor based on a strain gauge load cell (Figure 4.15). This type of sensor is ideal for measuring aerodynamic forces and moments due to its high sensitivity, accuracy, and robustness. Furthermore, the compact design of strain gauge load cells is particularly advantageous in confined spaces, such as the 2×2 inch wind tunnel, allowing them to be integrated into the experimental setup.

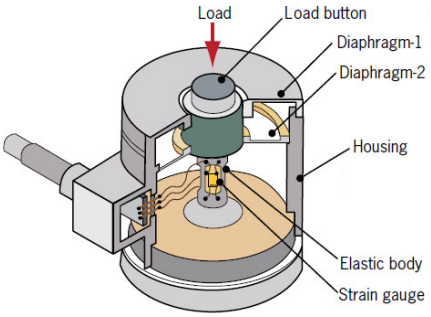

Figure 4.15: Typical strain gauge load cell architecture, adapted from [125].

More concretely, it uses a transducer to create an electrical signal proportional to the force being measured [108]. The cells operate by changing their electrical resistance in response to applied stress or strain. The linear relationship between electrical resistance and stress then simplifies the conversion of resistance readings into force measurements. Typically, strain gauge load cells consist of four strain gauges arranged in a *Wheatstone bridge* configuration (Figure 4.16).

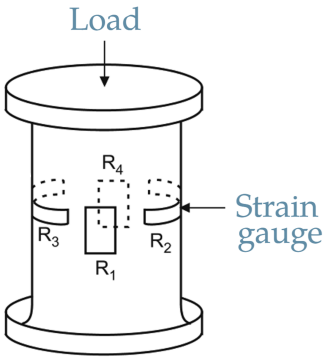

Figure 4.16: Typical strain gauge Westone bridge configuration, adapted from [78].

The sensor used in the present study is the F/T (Force/Torque) Sensor *Nano17-E* (Figure 4.17). Produced by ATI Industrial Automation, it is designed to measure all six components of force and torque. As the smallest commercially available 6-axis transducer, it has a diameter of 17 mm diameter (Engineering drawings are provided in Appendix D).

Figure 4.17: Force and Torque sensor Nano17-E, taken from [16].

The transducer also ensures high noise immunity and offers significant overload protection. Key features include **biasing** for offsetting tool weight and integral **temperature compensation** for accuracy over a wide range. This characteristic is crucial for ensuring reliable and consistent measurements, especially considering the significant temperature decrease within the test section during supersonic wind tunnel tests.

The manufacturer offers three distinct calibration ranges for the Nano 17-E sensor based on the following three characteristics :

- **Measurement range** : The range of force and torque values that the sensor is calibrated to measure accurately. Exceeding this range can cause potential damage or saturation error, resulting in invalid output values for all measured forces and torques [17].
- **Resolution** : The smallest detectable change in force or torque by the sensor.
- **Single-axis overload** : The maximum load a sensor can withstand in one direction before experiencing permanent damage [17].

Following preliminary investigations conducted before the beginning of this study, the decision was made to adopt the *SI-12-0.12* calibration, with its detailed characteristics provided in Table 4.5, alongside the associated reference frame depicted in Figure 4.18. Despite its limited operational range, this calibration offers exceptionally high resolution. However, given that the selected calibration is on the same order of magnitude as the expected forces, it is crucial **not** to exceed this calibrated range to prevent saturation errors.

Table 4.5: ATI Nano 17-E (SI-12-0.12) Forces and Torques characteristics [16].

	Forces [N]			**Torques [Nmm]**		
	Fx	Fy	Fz	Tx	Ty	Tz
Sensing Range	12	12	17	120	120	120
Overload	250	250	480	1600	1600	1800
Resolution	1/320	1/320	1/320	1/64	1/64	1/64

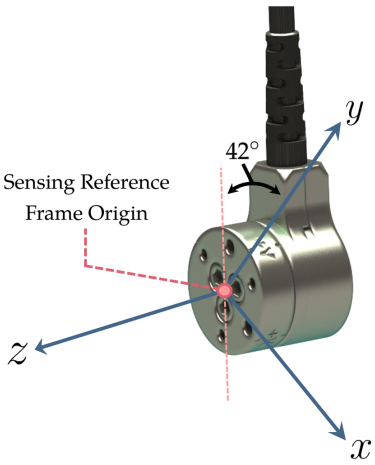

Figure 4.18: CAD representation of the Nano17-E sensor with its sensing reference frame.

In practical terms, the integration of the force balance required modification of the initial setup used for pressure measurements. One of the major changes was splitting the sting into two parts to accommodate the force balance (Figure 4.19). To that end, the rear sting has been fixed to the rear fastening washer, which is screwed to the back of the force balance. Similarly, the front fastening washer has been screwed to the front of the force balance and attached to the front sting. This configuration ensures that the forces generated on the bullet are transmitted directly to the front sting, which subsequently transfers them to the force balance.

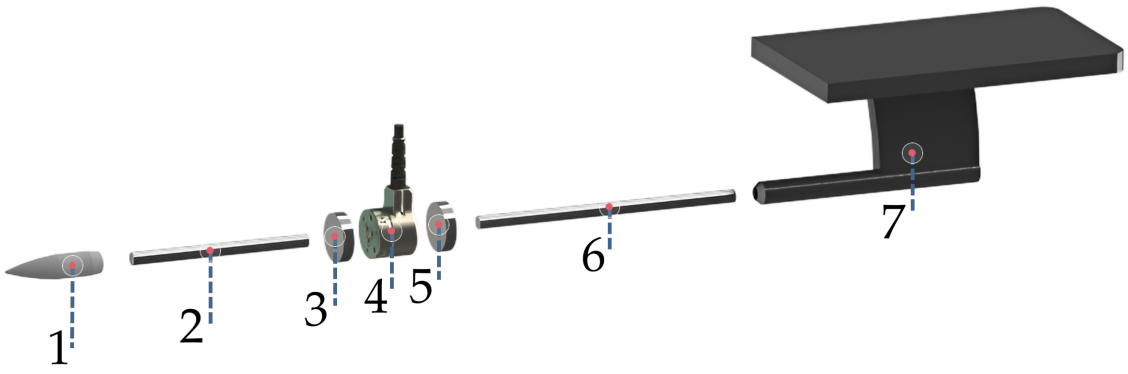

Figure 4.19: Exploded view of the aerodynamic forces measurement setup: (1) Projectile, (2) Front sting, (3) Front fastening washer, (4) Force balance, (5) Rear fastening washer, (6) Rear sting, and (7) Model positioning support.

4.6.1 Shield Design

While ensuring that the Nano17 remains within its calibration range is crucial to avoid saturation errors, efforts have been made to mitigate drag induced by the sensor's frontal area. Drawing inspiration from aerodynamic practices in sports, a *drafting* system has been implemented to minimize this drag. This approach mirrors the innovative technique observed in Figure 4.20, where an ice skater is seen accompanied by a car and a shield positioned strategically in front of him. This shield creates a low-pressure area behind it, allowing the skater to experience reduced air resistance as he skates closely behind it. Whether it is a car serving as a mobile barrier or a stationary shield, both redirect airflow to create regions of reduced pressure. This setup exemplifies the concept of drafting, a technique involving the strategic positioning of objects to reduce aerodynamic drag.

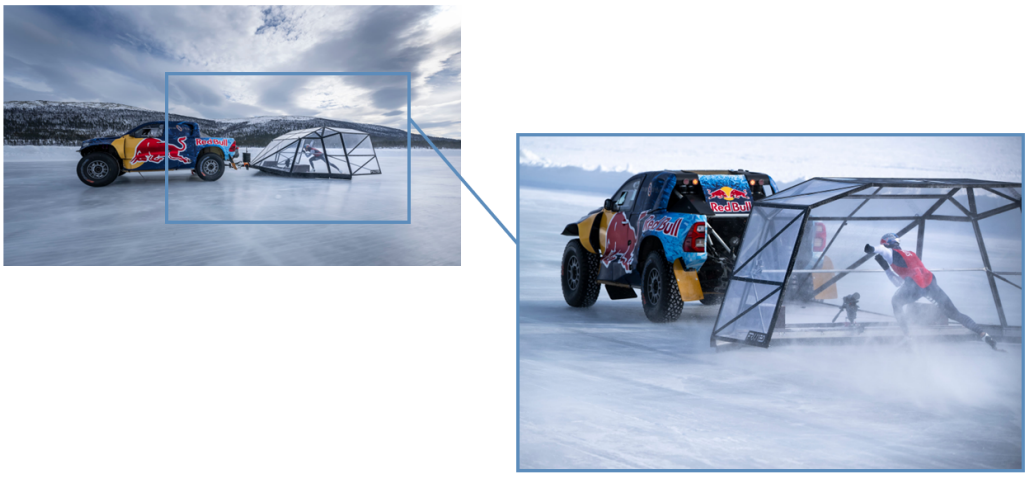

Figure 4.20: Aerodynamic drafting in speed skating, taken from [109].

Therefore, in order to avoid saturation, a streamlined profile for the front face of the force balance was designed. Based on Figure 4.21, which presents a qualitative comparison of 9 nose shape designs, it appears that the most ideal shape at Mach 2 is the *Von Kármán* nose. It should be noted that this performance chart is provided for $L/R = 6$, where L represents the length of the nose and R denotes the radius of its base.

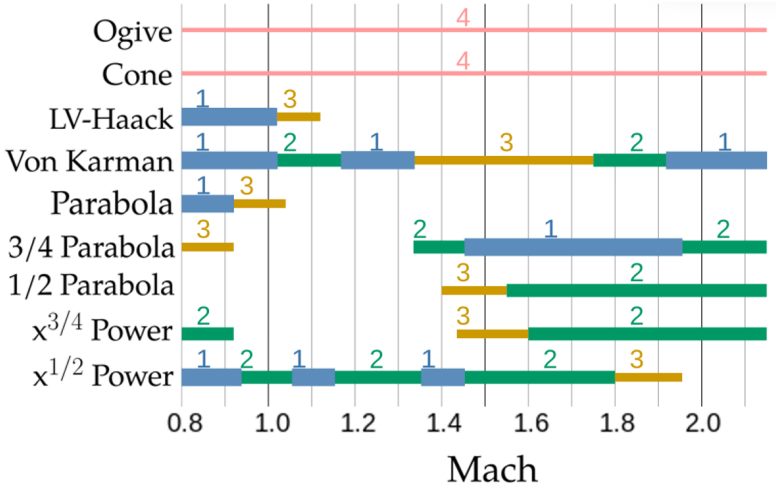

Figure 4.21: Qualitative comparison of 9 nose shapes for $L/R = 6$. Rankings are: (1) superior, (2) good, (3) fair, and (4) inferior (adapted from [28, 56]).

The Von Kármán nose belongs to the Haack series family (Equations 4.4 and 4.5) and corresponds to the particular case where $C = 0$. Its graphical representation is illustrated in Figure 4.22, alongside other specific values of C.

Haack series shapes

$$y(\theta, C) = \frac{R}{\sqrt{\pi}} \sqrt{\theta - \frac{\sin(2\theta)}{2} + C \sin^3(\theta)}\,, \tag{4.4}$$

where

$$\theta(x) = \arccos\left(1 - \frac{2x}{L}\right)\,. \tag{4.5}$$

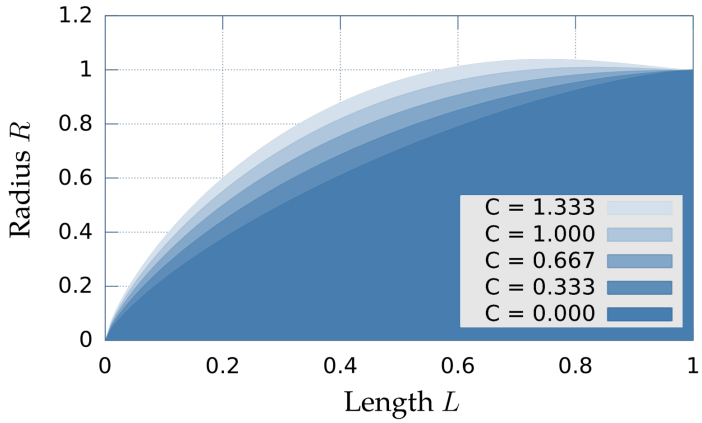

Figure 4.22: Haack series nose cone shapes, adapted from [7]. Particular values of C include : $C = 0$ for Von Kármán (LD-Haack), $C = 1/3$ for LV-Haack and $C = 2/3$ for Tangent.

Based on the Von Kármán nose profile, several shields were designed, differing primarily in their fineness ratio as defined by Equation 4.6. To ensure a precise fit with the sensor, the diameter was fixed at 17 mm, matching the diameter of the force balance. However, a compromise was necessary regarding its length. While a high fineness ratio (slender body) tends to reduce drag, it simultaneously increases lift due to the setup inside the test section not being perfectly centered in height. This arrangement allows for changes in the pitch angle of the test model while maintaining a **constant** centerline height.

Shield Fineness Ratio

$$\text{Fineness Ratio} = \frac{L_{\text{shield}}}{d/2}\,, \tag{4.6}$$

where L_{shield} is the length of the shield and d the diameter of the shield at its base.

Figure 4.23 illustrates the various shield designs tested. Just like the projectile, they were all 3D-printed with the same precision of 100 µm thick layers. It is important to note that all shield designs adhere to the criterion related to the critical length of the sting, which must

range between 3 and 5 model base diameters. This criterion is considered by measuring the distance from the base of the projectile to the nose of the shield. However, the FR6 shield is at the very limit of this requirement (and potentially non-compliant), as the distance is only 2.6 model base diameters. Despite being aware of this requirement violation, it was decided not to dismiss the FR6 shield a priori.

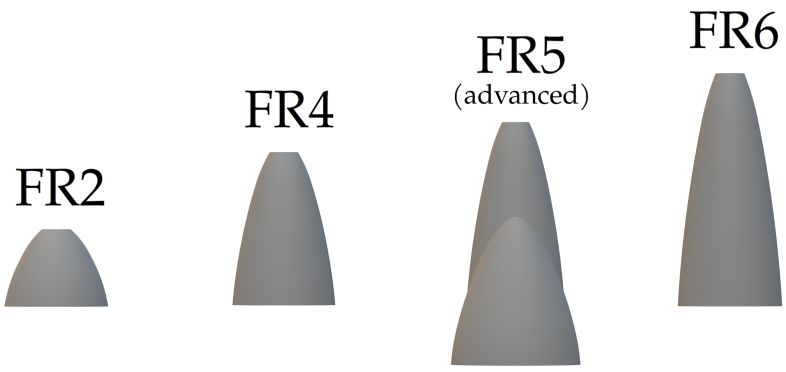

Figure 4.23: Shields tested during wind tunnel experiments for aerodynamic forces extraction. The shields vary in their fineness ratios (FR). Additionally, an advanced shield with a fineness ratio of 5 (FR5 advanced) was tested to evaluate its aerodynamic performance.

Ultimately, the **FR4 shield** (Figure 4.24a) was selected to balance the reduction of drag (enhanced by the FR6) and lift (enhanced by the FR2).

Regarding the FR5 advanced shield (Figure 4.24b), it was designed with a secondary shield above the primary one to prevent the formation of a normal shock on the metallic mount connected to the cable of the force balance. However, this design resulted in an excessive blockage ratio.

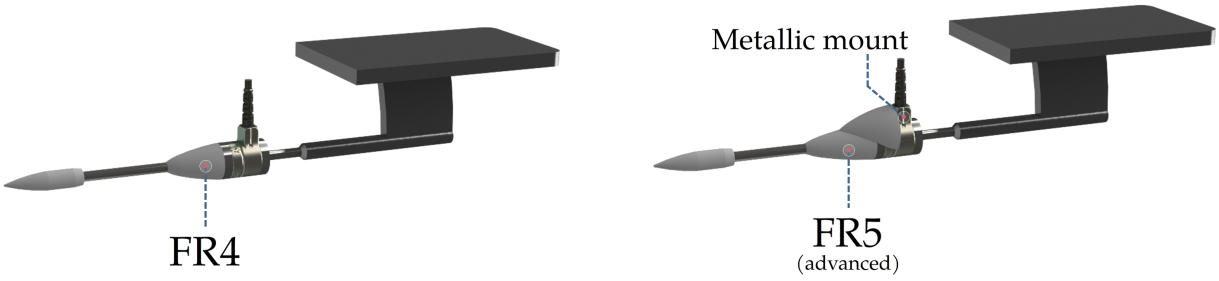

(a) FR4 shield.

(b) FR5 advanced shield.

Figure 4.24: CAD representation of the force measurement setup with the integration of shields : (a) FR4 and (b) FR5 advanced shield.

4.6.2 Blockage Ratio Limit

Generally, a blockage ratio between 5% and 10% is often considered acceptable for supersonic wind tunnels. However, during the initial design trial for integrating the force balance into the setup, 20 mm fastening washers were tried (Figure 4.25).

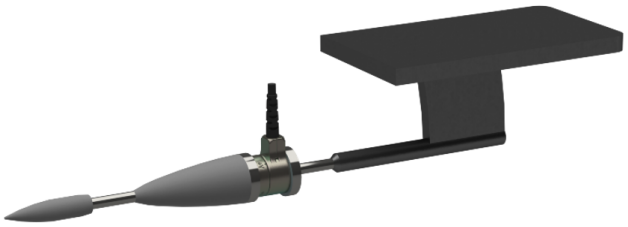

Figure 4.25: CAD representation of the initial force measurement setup with the integrated shield (FR6). The front and rear fastening washers had a diameter of 20 mm, and the shield was adapted accordingly.

This resulted in a blockage ratio (BR) of:

$$\mathrm{BR}_{20\,\mathrm{mm}} = \left(\frac{\frac{\pi \cdot 20^2}{4}}{50.8 \cdot 50.8} \right) \cdot 100 = 12.2\% \,. \tag{4.7}$$

The wind tunnel test conducted under these conditions highlighted the limitations of the wind tunnel regarding the blockage ratio. While best practices suggest not exceeding 10%, it was observed that this setup prevented achieving the desired flow in the wind tunnel's test section (verified with the "plot last run wind data" button). Concurrently, CFD predictions indicated the presence of a shock upstream of the test section, followed by flow separation at the lower wall of the wind tunnel. This manifested as undesirable vibrations of the setup, generating spurious forces that saturated the sensor.

In the second and final design iteration, a finer setup was developed using fastening washers with a diameter equal to that of the sensor (17 mm). This resulted in a blockage ratio (BR) of:

$$\mathrm{BR}_{17\,\mathrm{mm}} = \left(\frac{\frac{\pi \cdot 17^2}{4}}{50.8 \cdot 50.8} \right) \cdot 100 = 8.8\% \,. \tag{4.8}$$

The tests conducted with this setup showed no deficiencies regarding the flow conditions. Consequently, it was concluded that the maximum allowable blockage ratio for this wind tunnel is between 8.8% and 12.2%.

4.6.3 Aerodynamic Forces Extraction Procedure

The procedure for measuring aerodynamic forces begins with **warming up** the sensor. Since strain-gaged instruments inherently drift upon power-up, it is essential to allow the sensor to warm up for 30 to 45 minutes to equalize its temperature and reduce output drift.

Following the sensor warm-up, the compressor charges the tank. Once the necessary pressure for sustained steady measurements is reached, the wind tunnel is ready for testing. Just before starting a run, it is crucial to **bias** the sensor. The manufacturer strongly recommends biasing the sensor before each measurement period to mitigate output drift effects. Temperature gradients can induce drift, as can the weight of the setup itself, necessitating frequent biasing to maintain accuracy. This is particularly important because, during a test, as the flow expands, the temperature decreases.

Each test runs for 6 to 10 seconds, a duration found to be optimal for collecting sufficient data without completely depleting the tank after each run. Verifying the wind tunnel data after each test is a best practice before proceeding to post-process the data. This procedure is summarized in Figure 4.26 and the setup is illustrated in Figure 4.27.

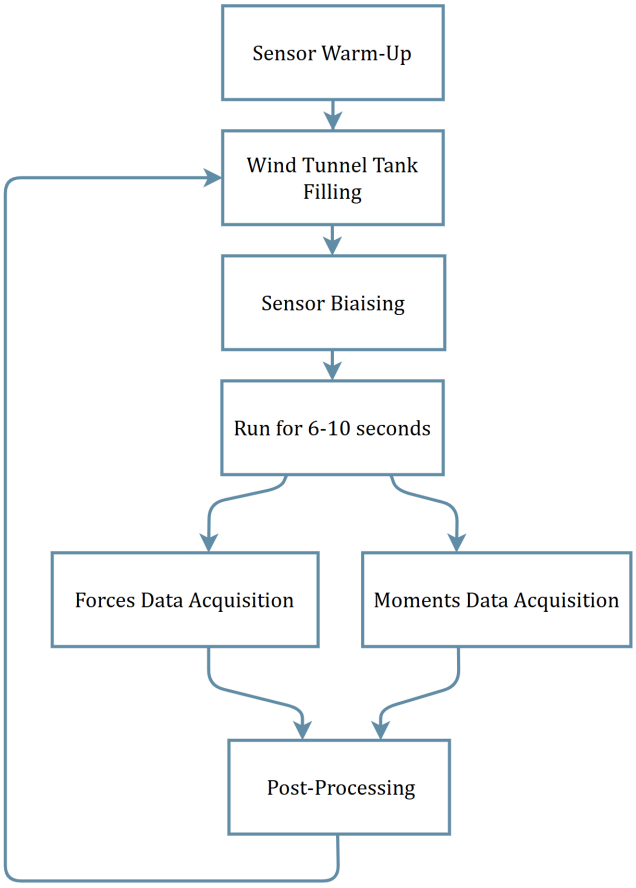

Figure 4.26: Workflow diagram for forces acquisition procedure.

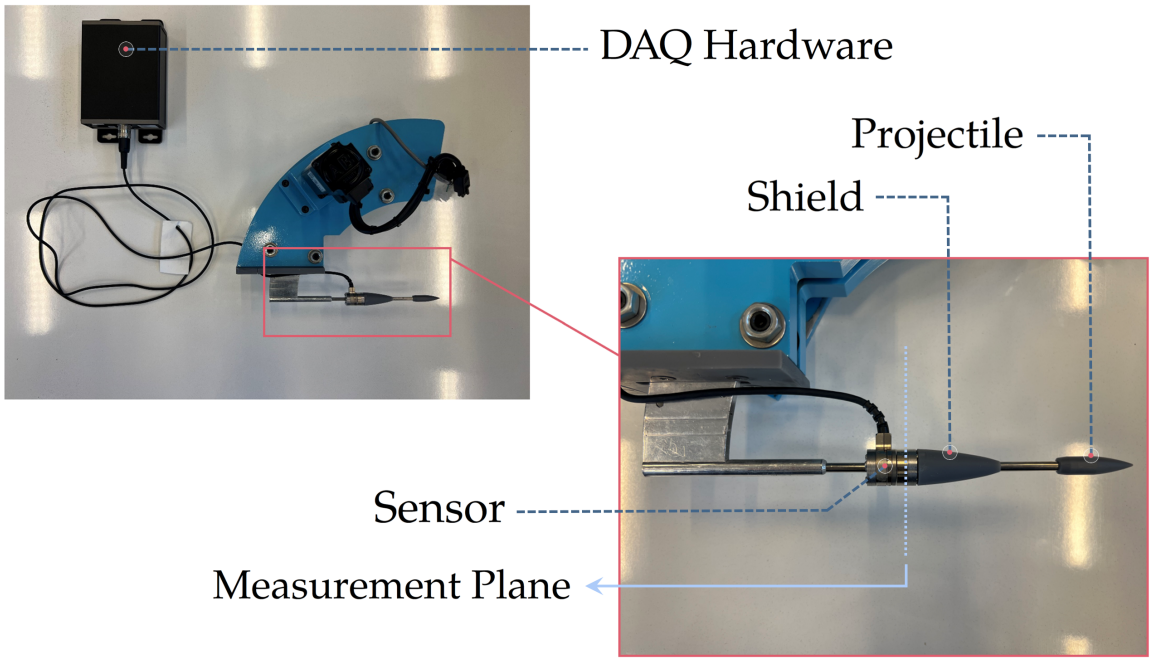

Figure 4.27: Experimental setup for aerodynamic forces extraction, including data acquisition (DAQ) hardware, sensor, shield, and projectile. The measurement plane of the sensor is represented by a dotted line (· · ·).

4.7 Conclusion on Experimental Investigation

Conclusion on Experimental Investigation

This chapter presented the comprehensive experimental setup and methodologies employed in the supersonic wind tunnel at the Royal Military Academy. Detailed descriptions of the wind tunnel components, control systems, and measurement techniques for surface pressure and aerodynamic forces were provided. Critical considerations, such as the adjustment of Reynolds numbers, blockage ratios, and linkage ratio, were discussed to ensure accurate and reliable data collection.

Through meticulous design and execution of these experimental procedures, the groundwork has been laid for validating the numerical models in subsequent chapters. The careful approach to managing wind tunnel conditions and measurement setups is essential for obtaining high-quality data that will support the study's objectives.

Chapter 5 | Numerical Investigation

This chapter details the numerical investigation using Simcenter STAR-CCM+. Supported by the Royal Military Academy's high-performance computing cluster, simulations were conducted to analyze the 5.56 mm NATO projectile aerodynamics. The computational setup, including domain definition, boundary conditions, and mesh strategies, is comprehensively described. Emphasis is placed on mesh refinement, solver settings, and physical models. Complementary geometries are examined to assess mounting and confinement influences. All the investigation is carried out at Mach 2, 0° angle of attack and at a Reynolds number of 1.13×10^6.

5.1 Software and Computing Capability

This numerical study is conducted using Simcenter STAR-CCM+ (version 2310, October 2023), a multiphysics computational fluid dynamics (CFD) software [120]. The Royal Military Academy supports its research activities with state-of-the-art facilities, including a high-performance computing (HPC) cluster comprising 904 cores [113]. For the present study, all simulations were performed on this HPC cluster using 80 cores.

5.2 Computational Domain and Boundary Conditions

The computational domain encompasses the nozzle, the test section, and the diffusers of the wind tunnel (Figure 5.1). Since the projectile under consideration is non-rotating, a three-dimensional half-model is used to leverage the problem's symmetry. It should be noted that the force balance wire was simplified to facilitate meshing. The finer details of the cable above the metallic mount were smoothed out.

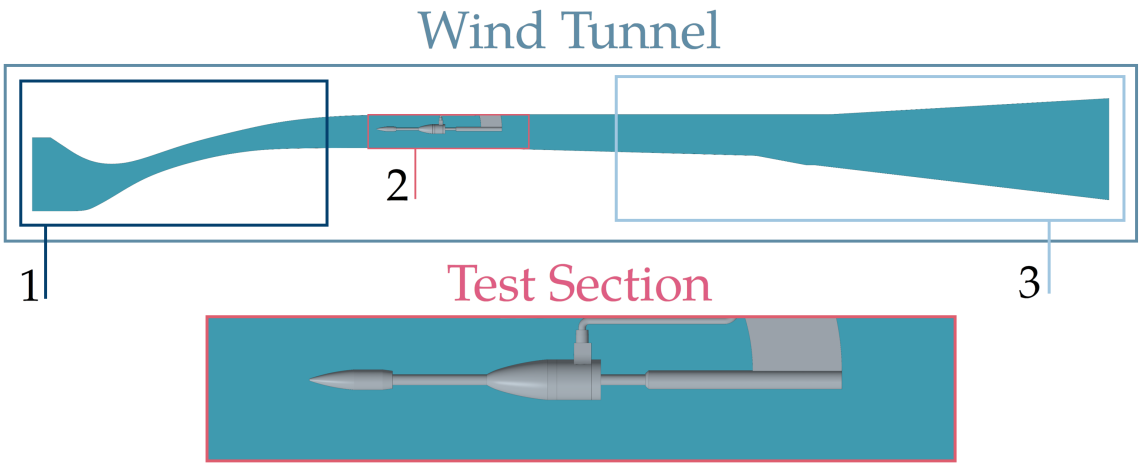

Figure 5.1: Geometry of the wind tunnel and definition of (1) the nozzle, (2) the test section, and (3) the diffusers.

While a distinction was previously made between the front and rear components of the stings and fastening washers in the experimental setup, no such differentiation will be made in this chapter. Components downstream of the sensing frame origin are not relevant in the current analysis due to the supersonic nature of the flow. Therefore, the front sting and front fastening washer will be simply referred to as the sting and fastening washer, respectively.

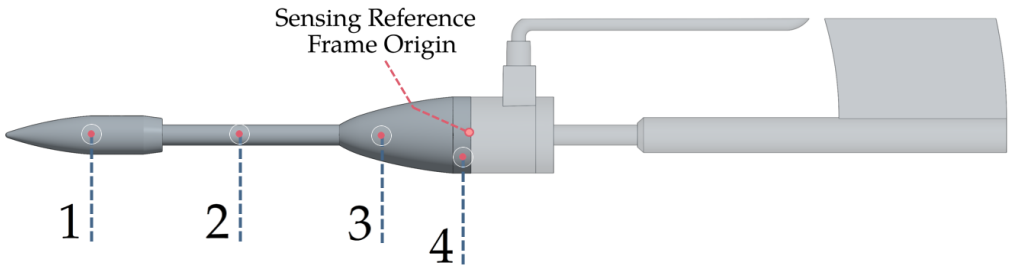

Figure 5.2: Highlighting key components for numerical analysis. (1) projectile, (2) sting, (3) shield, and (4) fastening washer.

Boundary Conditions

To accurately replicate experimental tests, it is essential to impose boundary conditions that closely match the experimental condition. This approach ensures that the numerical model faithfully represents reality, enabling meaningful comparisons with experimental results. The boundary conditions illustrated in Figure 5.3 and detailed below have been applied to achieve this fidelity.

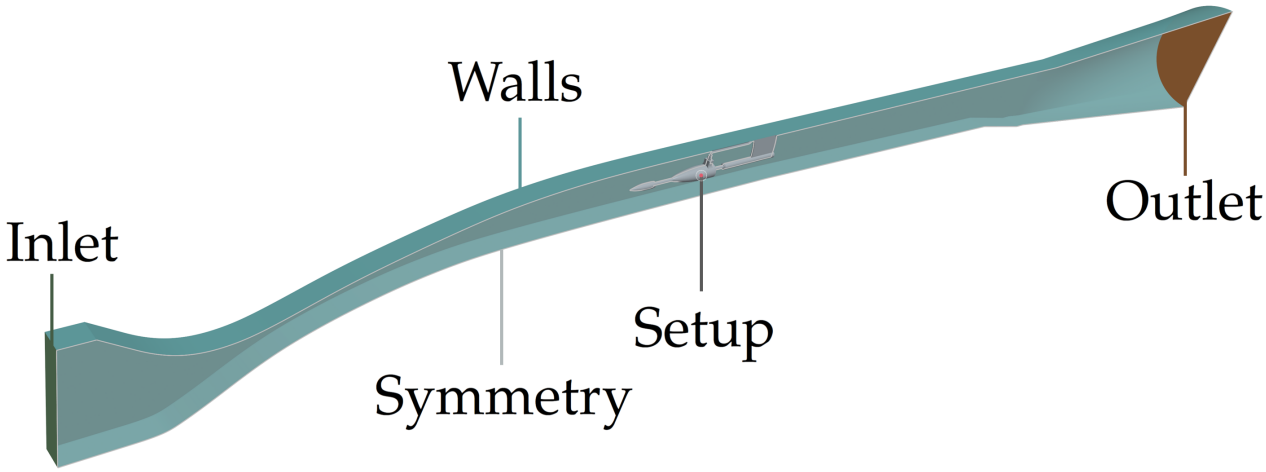

Figure 5.3: Identification of different surfaces within the computational domain.

- **Inlet** : The *Stagnation Inlet* boundary type is applied at the entry of the tunnel. It is an appropriate condition for compressible flows, representing an imaginary plenum far upstream where the flow is completely at rest. This boundary type has been parameterized as follows :
  - The **flow direction** is set to *boundary-normal*.
  - The **total pressure** is set to $268 \cdot 10^3 - 101325 = 166675$ Pa, *i.e.*, the gauge total pressure is set to 166675 Pa. This pressure was imposed to comply with the pressure recommended by Aerostream and imposed during the experimental tests. The **total temperature** is maintained at 300 K.
  - The **turbulence conditions** are imposed with the *turbulence intensity* and the *viscosity ratio*. The turbulence intensity is set at 1%, which is the upper bound typically observed in high-quality wind tunnels [119]. The viscosity ratio is set to 10, aligning with the upper limit commonly recommended for wind tunnel flows.
- **Wall** : The *Wall* boundary type is applied to all the surfaces of the domain. It represents an impermeable surface. The following settings have also been set :
  - The **surfaces properties** is set to *adiabatic* and *smooth* wall, with *no-slip* condition.
- **Symmetry** : The *Symmetry Plane* boundary type is applied at the symmetry of the tunnel. The solution obtained using a symmetry plane boundary is identical to the solution obtained by mirroring the domain about the symmetry plane. No additional boundary properties was necessary.

- **Outlet** : The *Pressure Outlet* boundary type is set at the exit of the tunnel. It is used for compressible and internal flows where the pressure is specified. Here :
  - The **backflow specification** is set to *extrapolated*, which extrapolates the flow direction from the interior of the domain.
  - The **gauge pressure** is imposed at 0 Pa, and the **static temperature** at 300 K.
  - Similar to the inlet boundary condition, the **turbulence conditions** are set with a turbulence intensity of 1% and a viscosity ratio of 10.

5.3 Mesh Generation and Analysis Focus

5.3.1 Meshing Process

For three-dimensional simulations, the meshing process is divided into three main parts : the *Surface Remesher*, the *Boundary Layer Mesher* and the *Core Volume Mesher*. It was decided to use **Triangular** elements for the surface remesher, **Advancing Layer Mesher** for the boundary layer mesh and **Polyhedral** elements for the core mesh.

The Advancing Layer Mesher interacts with the Surface Remesher to generate a polygonal surface mesh from the initial triangulated surface. It then extrudes this mesh to create prismatic cell layers in the volume region. This approach reduces dependency on topology, resulting in thicker, more uniform layers compared to other methods. Additionally, it improves mesh quality by adjusting faces and edges. Furthermore, it ensures consistent layer thickness in narrow gaps, offering better control over y^+ values.

Polyhedral meshes, like those used in the core mesh, are *unstructured*, offering greater flexibility in capturing the geometry efficiently.

5.3.2 Meshing Convergence Strategy

The meshing strategy employed involves a two-step process to ensure accurate capture of both micro and macro flow characteristics. First, near-wall treatment is performed to accurately capture the effects of small-scale turbulence within the boundary layer. This involves refining the mesh near the walls to resolve the steep gradients in velocity and other quantities. Subsequently, attention is directed towards the overall mesh sensibility by evaluating the influence of varying surface and volumetric discretization. These steps ensure that both local and global flow features are adequately resolved. This approach balances the need for detailed turbulence modelling with the requirement for efficient computation.

5.3.3 Meshing Refinement Procedure

The mesh refinement procedure involves using the previous mesh to generate the subsequent one. This method is time-efficient as it leverages the solution from the previous (coarser) mesh as the starting point for the new (finer) mesh, rather than starting a new simulation from scratch each time. This transition from one mesh to another typically causes a peak in residuals during the initial iterations for all variables, which gradually return to converged values.

To account for computational time during convergence, it was decided to evaluate the *Meshing CPU Time* rather than the total simulation CPU time, as is commonly done. Despite this focus on meshing CPU time, it is still possible to discern trends in overall computational time. A longer meshing time will invariably lead to a longer overall simulation time.

To evaluate mesh convergence, a relative difference is calculated between successive meshes. The goal is to determine the point at which further mesh refinement no longer significantly alters the solution. Depending on the sensitivity of the modified mesh parameters, convergence is considered when the relative difference falls below a certain threshold, typically 1%. In other words, the maximum allowable variation between successive meshes is 1%. However, for certain parameters, this criterion may be adjusted to account for slight but still significant changes relative to the observed range of previous variations. In this study, this relative difference will be used to evaluate the variation of the drag coefficient (Equation 5.1).

$$\delta_{C_{D,\,\mathrm{Mesh}_i}} = \left| \frac{C_{D,\,\mathrm{Mesh}_i} - C_{D,\,\mathrm{Mesh}_{i+1}}}{C_{D,\,\mathrm{Mesh}_i}} \right| \cdot 100 \;, \quad \text{with } i = 1, 2, 3, 4, 5 \,. \tag{5.1}$$

5.3.4 Quantities of Interest

Since the study focuses on determining the aerodynamic forces acting on the projectile at 0°angle of attack, the main concern is on the drag. Therefore, the convergence study was centered on the components of this force. Specifically, a viscous quantity (skin-friction coefficient) and a pressure-related quantity (dimensionless wall static pressure) were selected alongside the drag coefficient itself. It should be noted that the dimensionless wall static pressure is derived by normalizing the wall static pressure with the free stream static pressure upstream of the projectile, as commonly done for projectile [110].

5.4 Mesh Convergence Study

STAR-CCM+ provides the option to define a reference length known as the *Base Size*, upon which several other dimensions can be based, such as target surface size, maximum and minimum surface sizes, prism layer thickness, etc. These dimensions are then defined as percentages of this reference length. The chosen Base Size (BS) was **50 mm**, reflecting the dimensions of the test section (50.8×50.8 mm). This value remains **constant** throughout the convergence study. The box below outlines the mesh configuration at the beginning of the convergence study.

Mesh Parameters at the Onset of Convergence Study

- Number of Prism Layers : 36
- Prism Layer Stretching : 1.12
- Prism Layer Thickness : 2.0% of BS
- Surface Growth rate : 1.1
- Target Surface Size : 1.6% of BS
- Volume Growth Rate : 1.16

5.4.1 Near-Wall Requirement

Firstly, the prism layer stretching, which determines the thickness of each cell layer as a ratio of the previous layer, was set to 1.12. Secondly, the total thickness of the prismatic cell layers, specified as a percentage of the base size, was set to 2.0% (equivalent to 0.001 m). Therefore, the remaining parameter needed to fully define the boundary layer mesh was the number of prism layers. To ensure a consistent relative difference computation, a scaling factor of 1.2 for the number of prism layers between each successive mesh was chosen. It should be noted that a significant number of meshes were investigated to observe the influence of different y^+ values (where the target is $y^+ \sim 1$) on convergence, specifically targeting $y^+ > 5$, $5 > y^+ > 1$, and $y^+ < 1$. Figure 5.4 qualitatively illustrates the influence of this parameter on the quantities of interest, while Table 5.1 provides a quantitative analysis where the converged mesh is selected based on δ_{C_D} given by Equation 5.1 (for i ranging from 1 to 7).

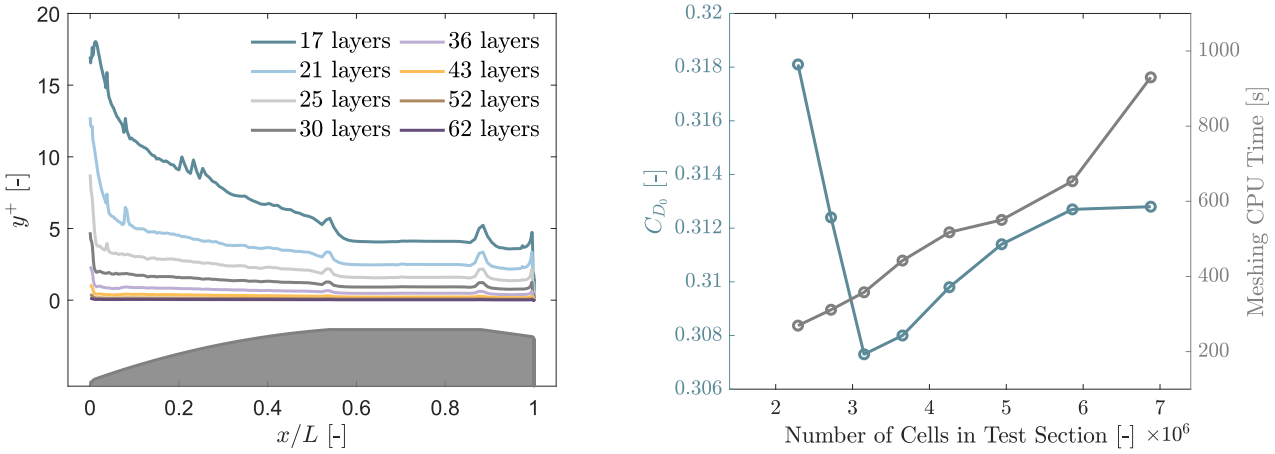

(a) Dimensionless distance from the wall.

(b) Drag coefficient and meshing CPU time.

(c) Dimensionless wall static pressure.

(d) Skin-friction coefficient.

Figure 5.4: Convergence analysis of the boundary layer mesh by varying the number of prism layers.

Table 5.1: Boundary layer mesh convergence with varying number of prism layers (N_{layers}), highlighting changes in mean dimensionless distance from the wall ($\overline{y^+}$), number of cells in the test section ($N_{\text{cells}_{\text{TS}}}$), meshing CPU time ($\text{CPU}_{\text{meshing}}$), and drag coefficient (C_D). The line representing the converged selected mesh is highlighted in bold.

	Characteristics				Convergence	
Mesh	N_{layers} [-]	$\overline{y^+}$ [-]	$N_{\text{cells}_{\text{TS}}} \times 10^6$ [-]	$\text{CPU}_{\text{meshing}}$ [s]	C_D [-]	δ_{C_D}[%]
1	17	7.15	2.29	269.21	0.3181	1.79
2	21	3.79	2.72	311.4	0.3124	1.63
3	25	2.22	3.15	357.85	0.3073	0.23
4	30	1.24	3.65	442.28	0.3080	0.58
5	36	0.62	4.26	517.60	0.3098	0.52
6	**43**	**0.28**	**4.94**	**550.48**	**0.3114**	**0.42**
7	52	0.10	5.86	653.41	0.3127	0.03
8	62	0.03	6.88	930.00	0.3128	–

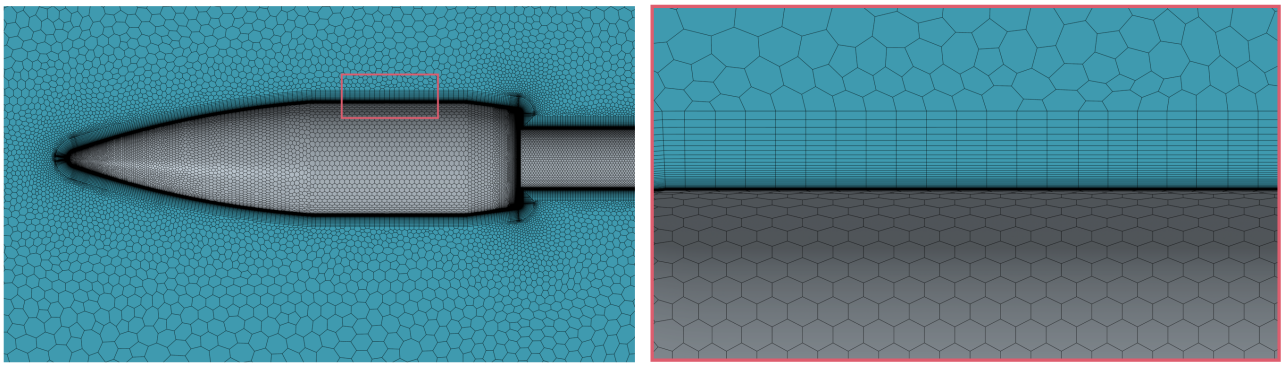

Figure 5.5: Boundary layer mesh applied on the solid surfaces of the domain. The figure includes a zoomed view of the mesh on the bullet surface, highlighting the detailed mesh structure in the boundary layer region.

5.4.2 Surface Mesh

It was found that variations in cell size on the domain surfaces have a negligible effect on the quantities of interest. However, it was decided to halve the size of the surface elements to achieve better surface discretization and obtain smoother plots. The cell size is therefore set to 0.8% of the base size. Given that the suggested range for surface growth rate (SGR) is between 1.1 and 1.6, a value of 1.1 was maintained to ensure low mesh anisotropy. Although

surface discretization does not significantly impact results, the cell size was reduced by a factor of four at critical edges, such as geometric transitions along the projectile, the intersection between the shield and the sting, and the edges of the metal mount for the sensor. The cell size at these critical edges is set to 0.2% of the base size. Figure 5.6 illustrates the surface mesh on the projectile. It should be noted that the base of the projectile has a higher density than the rest of the body due to the activation of the curvature refinement option.

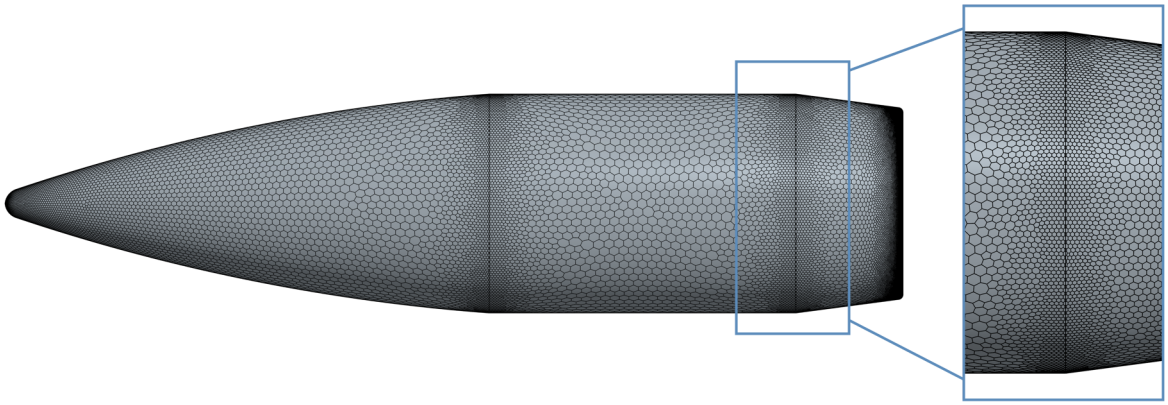

Figure 5.6: Surface mesh of the projectile with cell sizes of 0.8% of the base size (BS =50 mm) and 0.2% at geometric transitions.

5.4.3 Volume Mesh

The influence of the volume growth rate (VGR), which specifies the cell transition from the boundaries to the core mesh, was studied by halving its value with each new mesh iteration. The recommended range of this parameter is within the range 1.0 to 2.0. Figure 5.7 qualitatively illustrates the impact of this parameter on the quantities of interest, while Table 5.2 quantitatively summarizes its influence. The choice of the converged mesh is based on the computation δ_{C_D} given by Equation 5.1.

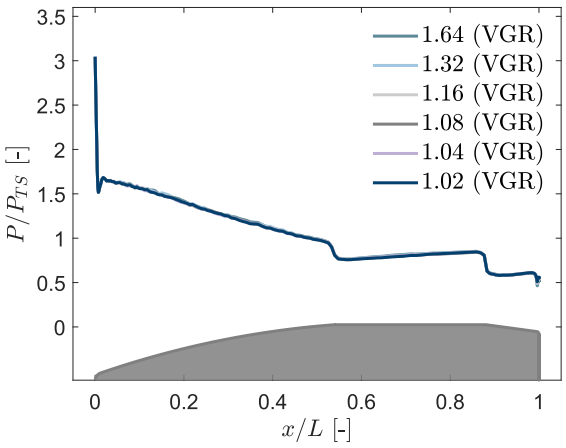

(a) Dimensionless wall static pressure.

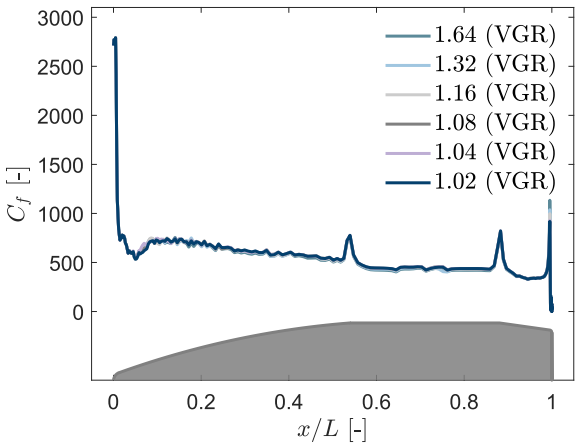

(b) Skin-friction coefficient.

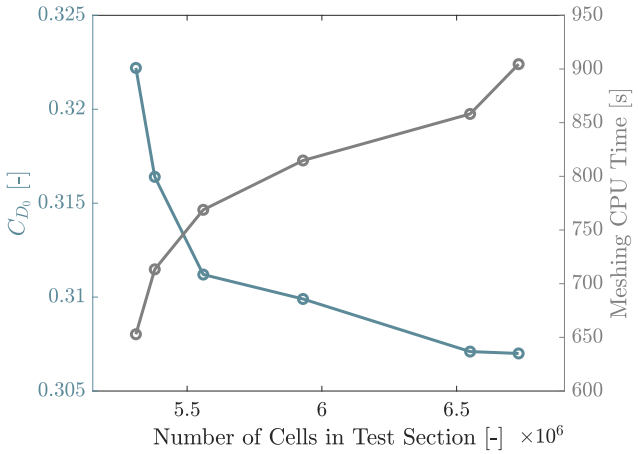

(c) Drag coefficient and meshing CPU time.

Figure 5.7: Convergence analysis of the volume mesh by varying the volume growth rate (VGR).

Table 5.2: Volume mesh convergence with varying volume growth ratio (VGR), number of cells in the test section ($N_{\text{cells}_{\text{TS}}}$), meshing CPU time ($\text{CPU}_{\text{meshing}}$), and drag coefficient (C_D). The line representing the converged selected mesh is highlighted in bold.

	Characteristics			Convergence	
Mesh	VGR [-]	$N_{\text{cells}_{\text{TS}}} \times 10^6$ [-]	$\text{CPU}_{\text{meshing}}$ [s]	C_D [-]	δ_{C_D} [%]
1	1.64	5.31	652.89	0.3222	1.80
2	1.32	5.38	713.36	0.3164	1.64
3	1.16	5.56	768.81	0.3112	0.42
4	1.08	5.93	814.75	0.3099	0.90
5	**1.04**	**6.55**	**858.12**	**0.3071**	**0.03**
6	1.02	6.73	904.49	0.3070	–

Figure 5.8 illustrates the converged mesh retained for the subsequent study, featuring a volume growth rate of 1.04. It should be noted that the surface mesh of the projectile has been deliberately omitted from the visualization, and the symmetry of the tunnel has been leveraged to depict the *real* geometry of the tunnel. However, it is important to highlight that only **half** of the tunnel is included in the computational domain.

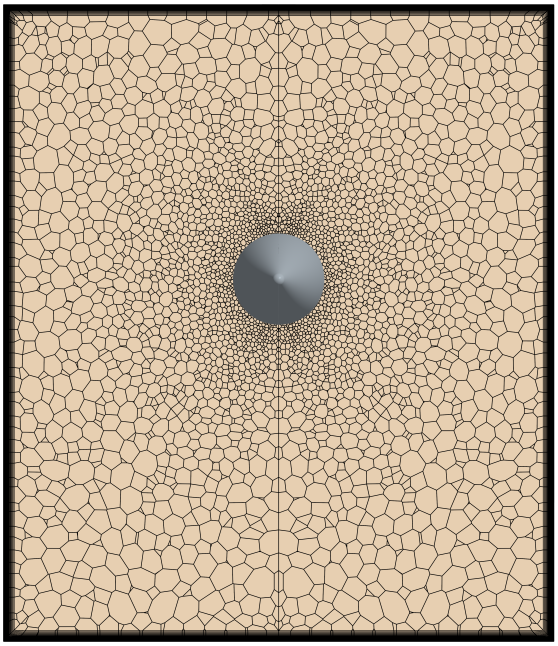

Figure 5.8: Core mesh of the tunnel with a volume growth rate of 1.04, shown at a cross-section at the middle of the sting.

5.4.4 Mesh Quality Enhancement (Post-Treatment)

With the converged mesh defined, it was decided to tighten certain constraints related to mesh quality. To achieve this, the following improvements have been applied :

- Transition from triangular elements to "enhanced quality triangles", which generate triangle surfaces of higher quality. These elements align better with curvature and boundaries (feature edges, part boundaries), and are more adept at capturing the geometry accurately.
- Increase in the minimum cell quality threshold, which ranges from 0.0 to 0.2. This threshold allows the mesher to ignore or modify feature edges when face quality falls below the minimum range. Previously set at 0.05, it has been increased to 0.2.
- Increase in number of core mesh optimization cycles, which ranges from 1 to 8. These cycles are performed by the mesher to enhance the quality and suitability of the volume mesh for the geometry. The number of cycles has been increased from 5 to 8.
- Additionally, the quality threshold, which specifies the maximum cell quality aimed for during the core mesh optimization cycles, ranging from 0.4 to 1.0, has been elevated from 0.7 to 1.

5.4.5 Final Mesh

The final mesh configuration was determined at the end of the last convergence study. Detailed pictures of the final mesh are provided in Appendix G. Table 5.3 summarizes the main characteristics, including the number of prism layers in the boundary layer mesh (N_{layers}), the associated mean dimensionless distance from the wall ($\overline{y^+}$), the surface and volume growth rates (SGR and VGR, respectively), the number of cells in the test section and in the overall computational domain ($N_{\text{cells TS}}$ and $N_{\text{cells Tot}}$, respectively), and finally, the meshing CPU time ($\text{CPU}_{\text{meshing}}$).

Table 5.3: Parameters for the final mesh configuration at the end of the convergence study.

N_{layers} [-]	$\overline{y^+}$ [-]	SGR [-]	VGR [-]	$N_{\text{cells TS}}$ [-]	$N_{\text{cells Tot}}$ [-]	$\text{CPU}_{\text{meshing}}$ [s]
43	0.28	1.1	1.04	$8.43 \cdot 10^6$	$1.23 \cdot 10^7$	1465.69

5.5 Mesh Quality Assessement

Simcenter STAR-CCM+ offers a range of cell metrics that are instrumental in assessing the overall quality of the mesh. The available metrics include: Face Validity, Cell Quality, Volume Change, Cell Skewness Angle, Chevron Quality Indicator, Least Squares Quality, and Cell Warpage Quality (refer to Appendix F for detailed explanations on these mesh quality terms). Table 5.4 summarizes the mesh quality metrics used for the mesh quality evaluation.

Table 5.4: Mesh Quality Metrics based on STAR-CCM+ User Guide recommendations [119].

	Bad	Fair	Good	Perfect
Face Validity	<1	-	1	-
Cell Quality	$<$ 1e-5	-	$<$1	1
Volume Change	$<$ 1e-2	-	1	-
Cell Skewness Angle	$>85°$	-	$<85°$	-
Chevron Quality	1	-	0	-
Least Squares Quality	$<$ 1e-3	-	$<$1	1
Cell Warpage Quality	<0.15	-	$<$1	1

The following figures present the results of the various mesh metrics evaluated (Figure 5.9). When computing the midpoint for histograms of mesh metrics, the software determines it as the midpoint of each bin or interval. These intervals divide the mesh metrics into specific ranges. For each interval, it calculates the midpoint by averaging the lower and upper bounds. Subsequently, it plots the histogram with mesh metric values on the x-axis and the frequency (number of cells in each bin) on the y-axis. The width of the bars in the histogram indicates the concentration of cells within the intervals: narrower bars signify that the cells are concentrated in a smaller range of values, while wider bars indicate a broader interval.

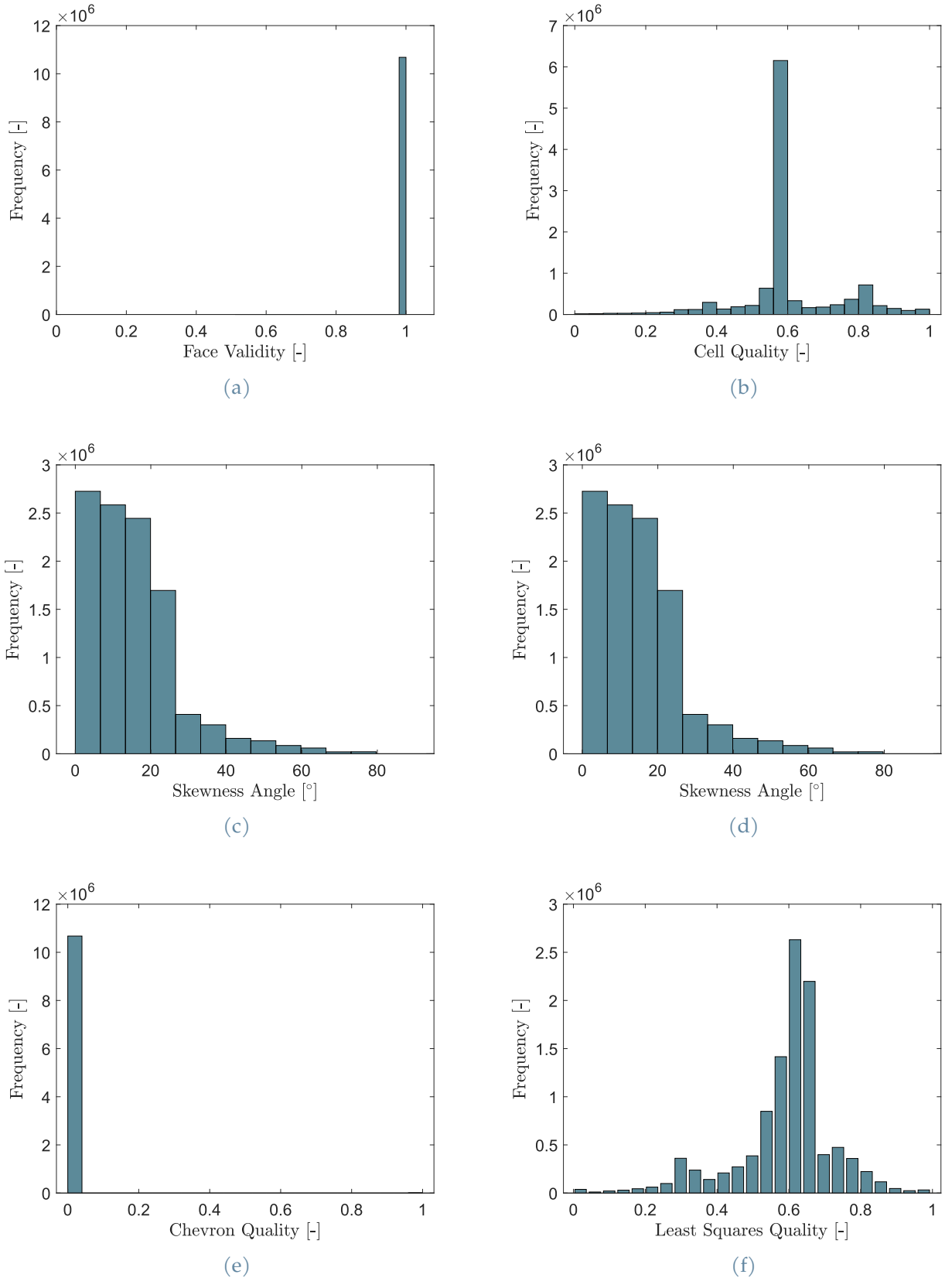

Figure 5.9: Mesh quality assessment.

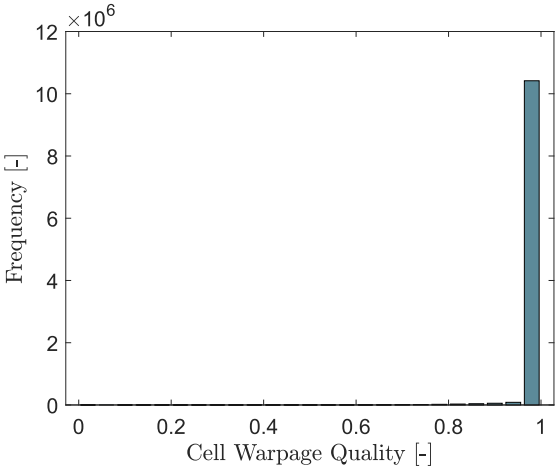

(g)

Figure 5.9: Mesh quality assessment (*continued*).

The evaluation of the various mesh metrics indicates that the mesh is of relatively good quality, as none of the cells are considered *bad* (according to the criteria provided in Table 5.4).

5.6 Physics

The wind-tunnel flow is modelled as an ideal, compressible gas governed by the RANS conservation equations. Due to the non-rotating nature of the projectile, a three-dimensional half-model is employed to exploit the symmetry of the problem.

5.6.1 Solver Settings

- **Steady Simulation**: A steady simulation approach is selected, as the study's primary goal is to compute aerodynamic forces and moments without focusing on transient effects. The flow is assumed to be steady in the region of interest.
- **Coupled Flow Solver**: The conservation equations are solved using coupled flow model (*density-based*). This solver is suitable for compressible flow applications, solving all equations simultaneously to ensure accurate results.
  - **Implicit Integration**: The implicit integration method is used. It is known to enhance stability for steady-state simulations.
  - **Hybrid MUSCL 3rd-Order/CD**: A blend scheme between a MUSCL (Monotone Upstream-Centered Schemes for Conservation Laws) 3rd-order upwind scheme and the 3rd-order central-differencing reconstruction scheme is used to discretize

the convective terms. It provides improved (reduced) dissipation when compared with the second-order scheme, and improves the stability and accuracy of high-speed flows [119].

- **Secondary Gradients**: Enabled to improve the accuracy of gradient calculations.
- **Coupled Inviscid Flux (AUSM+FVS)**: The AUSM+FVS (Advection Upstream Splitting Method with Flux Vector Splitting) scheme is employed for inviscid flux calculations. This scheme is recommended for supersonic due to its accuracy and robustness in handling compressible flows [32, 119].

5.6.2 Air Properties

- **Ideal Gas**: The ideal gas assumption simplifies modelling and reduces computational costs while capturing variations in density, temperature, and pressure in supersonic flows. This assumption is deemed acceptable for the current configuration [59] as even at Mach 4.5, the difference between ideal and real gas models does not imply a significant deviation in the value of the aerodynamic coefficients [35]. Selecting the ideal-gas model automatically enables the *energy coupled* equation to be solved.
- **Sutherland's Law for Viscosity**: The Sutherland's law (*Three Coefficient Method*) is applied to account for the variation of viscosity with temperature. This law relates dynamic viscosity to temperature, providing a more accurate representation under varying thermal conditions (refer to Appendix E for more details).
- **Constant Properties**: While density and viscosity are parameterized to account for temperature variations, specific heat c_p and thermal conductivity k are held constant. This is a standard practice in scenarios absent of chemical reactions, dissociation, or ionization, facilitating the modelling process.

5.6.3 Turbulence Model

- ***k*-*ω* SST Model**: The Shear Stress Transport (SST) k-ω model is used for simulating the flow due to its proven accuracy and reliability in high-speed aerodynamic applications. This model effectively predicts flow separation and adverse pressure gradients, crucial for the current application. By blending the strengths of the k-ϵ and k-ω models, the k-ω SST model offers robust near-wall treatment and free-stream accuracy.
  - **2nd Order Convection** : The turbulence equations are discretized using a second-order scheme, the highest accuracy provided by the solver.

- **Compressibility Correction** : Enabled to enhance the model's performance in high-speed flows. It allows accounting for dilatation dissipation and enhances the prediction of flows where compressible effects are dominant (refer to Appendix E for more details).

These settings collectively ensure that the simulations are accurate, efficient, and well-suited for the high-speed aerodynamic conditions encountered in this study.

5.6.4 Reference Values and Initial Conditions

In STAR-CCM+, all pressures are defined relative to a user-specified **reference pressure**. In this case, the reference pressure was set to 101325 Pa. This pressure represents the absolute pressure relative to which all other *gauge* pressures are defined.

The imposed **initial conditions** include a gauge pressure of 0 Pa, a static temperature of 300 K, a turbulence intensity of 0.01, a turbulent viscosity ratio of 10, and a velocity of 500 m/s (approximately Mach 2 given the inlet conditions). Additionally, the turbulent velocity scale which is a representative velocity that is required to convert the specified turbulence quantities to the transported turbulence quantities is set equal to the initial velocity as typically done [119].

5.7 Solver

The Coupled Implicit solver is configured with several specific settings to ensure robust and efficient simulations. These settings are chosen based on their proven effectiveness in high-speed aerodynamic applications [119].

- **CFL Control Method** : *Automatic CFL*
  The Courant–Friedrichs–Lewy (CFL) number is automatically controlled by the solver. This method adjusts the CFL number dynamically in response to the convergence behaviour of the linear algebraic solver. This approach accelerates convergence while preserving stability [15].
- **Relaxation Methods** : *Constant Explicit Relaxation*
  Explicit relaxation is set to a constant value. This method scales all corrections explicitly before applying them to the variables. The default value of 0.3 is used, which applies 30% of the corrections, providing a good balance between stability and convergence speed.

- **Linear Solver** : *Algebraic Multigrid (AMG) with F-Cycle*
  The AMG method accelerates solver convergence by efficiently reducing numerical errors through a hierarchy of successively coarsened linear systems. The *F-cycle* is employed due to its balance between computational demand and convergence properties. It combines the efficiency of the V-cycle with the robust convergence of the W-cycle, making it effective for handling complex error components with fewer computations. More information regarding this cycle is provided in Appendix E.

- **Initialization** : *Expert Initialization with Grid Sequencing*
  Grid sequencing initialization is used and begins from the imposed initial conditions. This approach constructs a sequence of coarse meshes, progressively refining them until the final mesh is obtained. It starts with a very coarse mesh and computes the inviscid flow solution. The results are then interpolated onto the next mesh, continuing until convergence is achieved on the finest mesh. This approach ensures the inclusion of important flow features such as shocks in the initialization. Since it operates on a sequence of coarse meshes, this approach enables a relatively quick attainment of the initial condition [32].

- **Convergence Acceleration** : *Continuity Convergence Accelerator (CCA)*
  The CCA is used to minimize mass imbalance for each cell at each iteration. This method formulates and solves a pressure-correction equation using density-based Riemann flux discretization, which is effective for high-speed compressible flows and significantly speeds up the simulation while maintaining accuracy.

- **Turbulence Model Relaxation**

  - $k-\omega$ **Turbulence Model Under-Relaxation (k and ω)** :
    The turbulence equations are set with an under-relaxation factor of 0.7. This reduces the probability of divergence in the turbulence model by tempering the updates to the turbulence variables turbulent kinetic energy k and the specific dissipation rate ω, ensuring stable convergence.

  - $k-\omega$ **Turbulent Viscosity Under-Relaxation (ν_T)** :
    The turbulent viscosity is set with an under-relaxation factor of 0.4. This further stabilizes the solution by controlling the rate at which the turbulent viscosity ν_T updates.

These settings collectively ensure that the solver operates efficiently and stably, providing accurate and reliable results for the high-speed aerodynamic simulations required in this study.

5.8 Monitors

5.8.1 Residuals

The STAR-CCM+ user manual cautions that when using *grid sequencing*, the residuals may **only** decrease by 2-3 orders of magnitude [119]. This occurs because grid sequencing initialization provides a better initial estimate of the flow field compared to initialization with uniform conditions. Therefore, the residuals for continuity, momentum components, energy, and turbulent quantities (ν_T, k, and ω) are tracked with a convergence criterion set at $1 \cdot 10^{-2}$. Figure 5.10 illustrates a typical plot of the residuals obtained during the simulations.

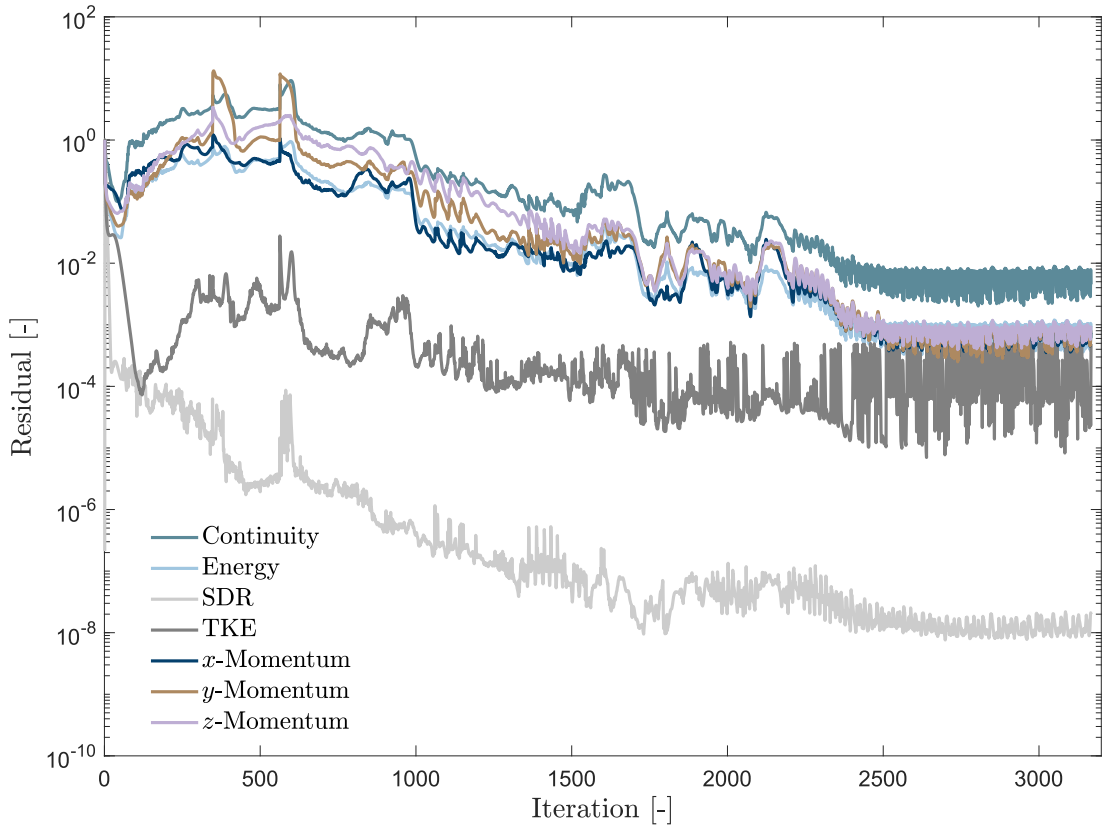

Figure 5.10: Typical plot of residuals. The residuals include continuity, energy, specific dissipation rate (SDR), turbulent kinetic energy (TKE), and x-, y-, and z-momentum components.

Furthermore, while these residuals collectively represent the discrepancies across the entire computational domain (reflecting the deviations from the exact solution of the governing equations), it is important to note that they are computed individually for each cell. Upon closer inspection of *continuity* (which typically exhibits the highest residual values), it be-

comes evident that it is influenced by relatively high residuals in the rear part of the wind tunnel (Figure 5.11). However, since this portion of the flow is not pertinent to the quantities of interest in the study, caution is warranted when interpreting these relatively "high" residuals, particularly for a fundamental quantity like continuity.

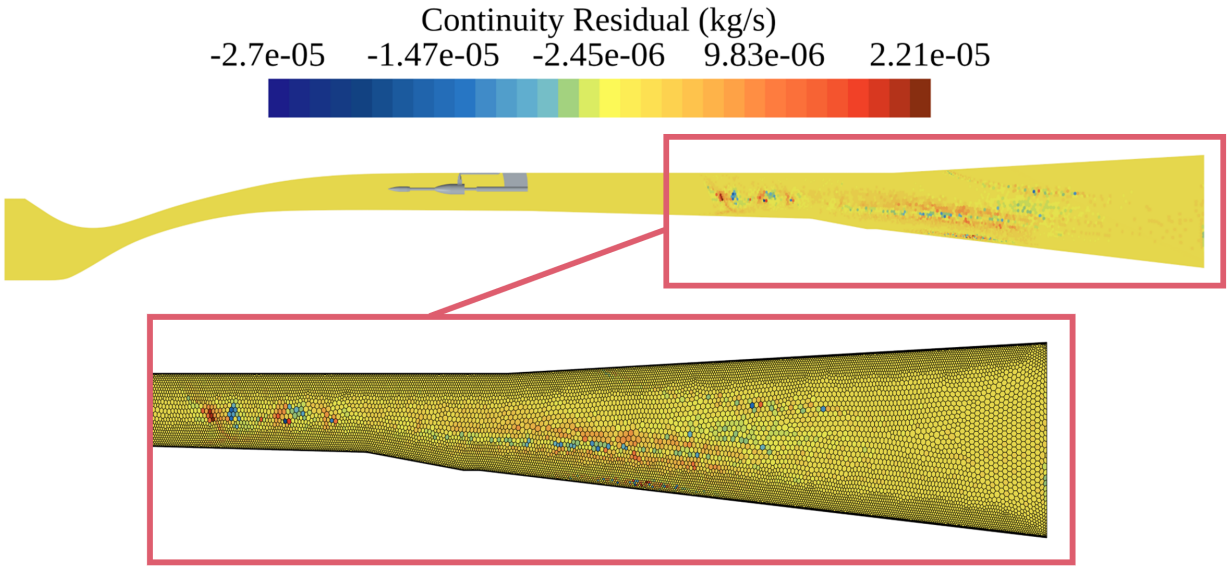

Figure 5.11: Typical distribution of cell residuals within the computational domain at a specific iteration during the simulation. The close-up view shows the mesh to associate the contour plot with specific cells. Note that this contour plot evolves throughout the iterations.

5.8.2 Stopping Criterion

The stopping criterion used for the simulation is the *asymptotic monitor*. This criterion allows the simulation to stop once it reaches an asymptotic limit. It defines a range within which the values can fluctuate over a specified number of iterations. This feature is particularly useful when the exact limiting value is unknown, but the maximum allowable change in the monitored value for sufficient convergence is known.

The limit is established by selecting a maximum permissible change in the monitored value over a given number of successive iterations. For this study, the chosen difference is $|\text{min} - \text{max}| = 0.0001$ over the last 250 iterations, and it is applied to the drag coefficient.

It is important to note that this criterion is monitored in parallel with the convergence of residuals, and the trend of the residuals is also taken into account.

5.9 Complementary Geometries

To assess the potential influence of the mounting on the aerodynamic forces to be measured, two additional geometries were constructed. The first geometry consists of the bullet supported only by the sting and the model positioning support. It was designed to evaluate the impact of integrating the force balance and the shield. This configuration is referred to as the *Sting-Mounted Projectile*.

The second geometry considers only the bullet (without any fixtures) in the test section to assess the influence of the sting and model positioning support. This configuration is referred to as the *Confined Free Flight Projectile*.

For both geometries, the projectile remains at the same position as for the *Sensor-Mounted Projectile* geometry.

5.9.1 Sting-Mounted Projectile

The same mesh as that used for the force balance mounted configuration is employed. The geometry under study is depicted in Figure 5.12.

Figure 5.12: Close-up view of the Sting-Mounted geometry within the test section of the wind tunnel.

5.9.2 Confined Free-Flight Projectile

While the case of confined free-flight is not practically feasible in the wind tunnel, it nevertheless allows for the examination of various aspects of the flow. Firstly, it facilitates the exploration of the blockage ratio issue and ensures that the induced blockage ratio does not influence the results. If this is the case, no sidewall effects are expected, and conditions similar to those of free-flight could be achieved. Secondly, it will shed light on the effect of the sting at the rear of the projectile. The geometry under study is depicted in Figure 5.13.

Figure 5.13: Close-up view of the Confined Free-Flight geometry within the test section of the wind tunnel.

Special Mesh Refinement Region

The same mesh as that used for the force-balanced mounted projectile configuration is used for this setup, except for the rear of the projectile. While the wake was adequately captured by the boundary layer mesh of the front sting in the force-balanced and sting-mounted configurations, a second convergence study is necessary for the confined free flight scenario to ensure accurate representation of this region. Indeed, the expected recirculation at the rear of the projectile can now develop freely, whereas in the force-balanced and sting-mounted configurations, it was obstructed by the sting.

The first parameter investigated is the length of the refinement region in the wake. Based on the projectile length L, a series of meshes were derived, with the length increasing by a factor of 2 each time. The element size in the wake was set to 0.8% of the base size. Figure 5.14 and Table 5.5 present the results obtained regarding the sensitivity of the drag coefficient to the length of the wake refinement region behind the projectile. The choice of the converged mesh is based on the computation δ_{C_D} given by Equation 5.1.

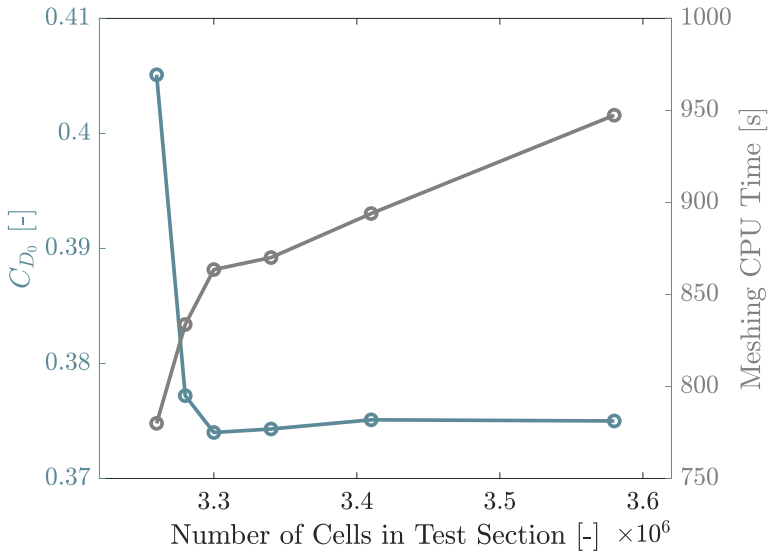

Figure 5.14: Convergence study of the wake refinement length on the drag coefficient C_{D_0}. The plot shows the influence of the number of cells in the test section on the drag coefficient (left y-axis) and the CPU time required for meshing (right y-axis).

Table 5.5: Confined free flight mesh convergence with varying wake length l_{wake} normalized by the projectile length L, alongside the associated variation in number of cells in the test section ($N_{\text{cells}_{\text{TS}}}$), meshing CPU time ($\text{CPU}_{\text{meshing}}$), and drag coefficient (C_D). The line corresponding to the converged selected mesh is highlighted in bold.

	Characteristics			Convergence	
Mesh	Wake Length $[l_{\text{wake}}/L]$	$N_{\text{cells}_{\text{TS}}} \times 10^6$ [-]	$\text{CPU}_{\text{meshing}}$ [s]	C_D [-]	δ_{C_D}[%]
1	0.125	3.26	779.95	0.4051	6.89
2	0.25	3.28	833.67	0.3772	0.85
3	0.5	3.30	863.51	0.3740	0.08
4	1	3.34	870.05	0.3743	0.21
5	**2**	**3.41**	**893.97**	**0.3751**	**0.03**
6	4	3.58	947.39	0.3750	–

With the wake length determined, the influence of cell size within the wake region can be explored. To achieve this, the element size was halved with each subsequent mesh refinement. The results are illustrated qualitatively in Figure 5.15 and quantitatively in Table 5.6, where the choice of the converged mesh is based on the computation δ_{C_D} given by Equation 5.1.

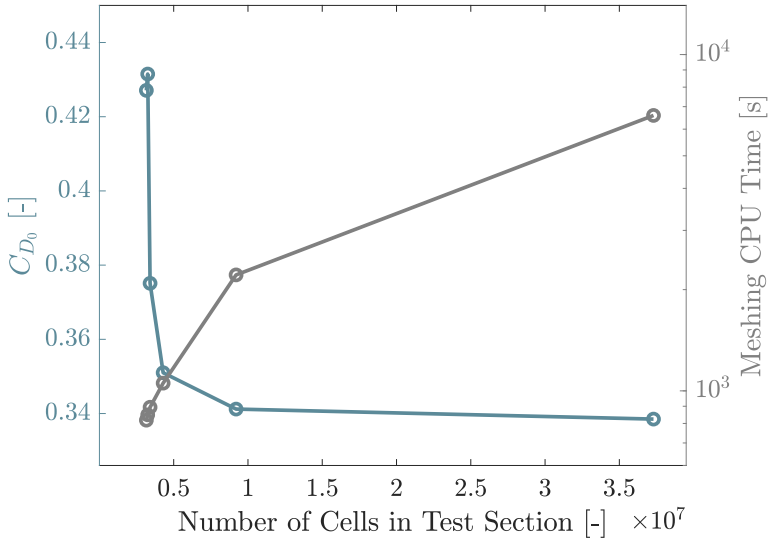

Figure 5.15: Convergence study of the wake cell size on the drag coefficient C_{D_0}. The plot shows the influence of the number of cells in the test section on the drag coefficient (left y-axis) and the CPU time required for meshing (right y-axis).

Table 5.6: Confined free flight mesh convergence with varying cell size in the wake given as a percentage of the Base Size, alongside the associated variation in number of cells in the test section ($N_{\text{cells}_{\text{TS}}}$), meshing CPU time ($\text{CPU}_{\text{meshing}}$), and drag coefficient (C_D). The line corresponding to the converged selected mesh is highlighted in bold.

	Characteristics			**Convergence**	
Mesh	Cell Size [% of BS]	$N_{\text{cells}_{\text{TS}}} \times 10^6$ [-]	$\text{CPU}_{\text{meshing}}$ [s]	C_D [-]	δ_{C_D}[%]
1	3.2	3.16	818.12	0.4271	1.03
2	1.6	3.25	848.62	0.4315	13.07
3	0.8	3.41	893.97	0.3751	6.42
4	0.4	4.29	1054.29	0.3510	2.79
5	**0.2**	**9.20**	**2211.99**	**0.3412**	**0.79**
6	0.1	37.3	6591.51	0.3385	–

5.10 Conclusion on Numerical Investigation

Conclusion on Experimental Investigation

This chapter provided a detailed the numerical investigation conducted using Simcenter STAR-CCM+, supported by the Royal Military Academy's high-performance computing cluster. The study centered on the aerodynamics of a 5.56 mm NATO projectile, specifically at Mach 2, 0° angle of attack, and at a Reynolds number of 1.13×10^6.

The chapter described the computational setup, including the definition of the domain, boundary conditions, and mesh strategies. Significant emphasis was placed on the process of mesh refinement to ensure accurate capture of both micro and macro flow characteristics. Detailed explanations of solver settings and physical models were provided, highlighting the use of advanced techniques to enhance simulation accuracy and efficiency. Additionally, complementary geometries were introduced to assess the influences of mounting and confinement on the projectile's aerodynamic forces.

Through this numerical investigation, the chapter set the foundation for the subsequent analysis and discussion of results.

Part II

Results and Discussion

Chapter 6 | Results and Discussion

This chapter presents a detailed comparison between experimental results and numerical predictions to validate the numerical approach used in this study. The validation process involves several key analyses, including Schlieren visualization, wall static pressure measurements, and drag coefficient comparisons. This chapter also explores the implications of the force-balance mounting and bullet confinement on aerodynamic measurements and delves into the challenges associated with wind tunnel testing. All results presented were carried out at Mach 2, 0° angle of attack and at a Reynolds number of 1.13×10^6.

6.1 Experimental Validation of the Numerical Approach

This section details the results used to validate the numerical approach through experimental data. Techniques such as Schlieren visualization, wall static pressure measurements, and drag force comparisons are employed to verify the computational model's accuracy and reliability. By systematically comparing experimental results with numerical predictions, this validation aims to confirm the robustness of the model and establish a solid foundation for subsequent analyses.

6.1.1 Schlieren Visualization

One key aspect to investigate is the qualitative analysis of the flow using Schlieren visualization obtained in the wind tunnel. This method allows for the visualization of density changes within the flow, highlighting phenomena such as shock waves and expansions. Figure 3.4 illustrates the comparison between numerical predictions and a snapshot taken during a wind tunnel test.

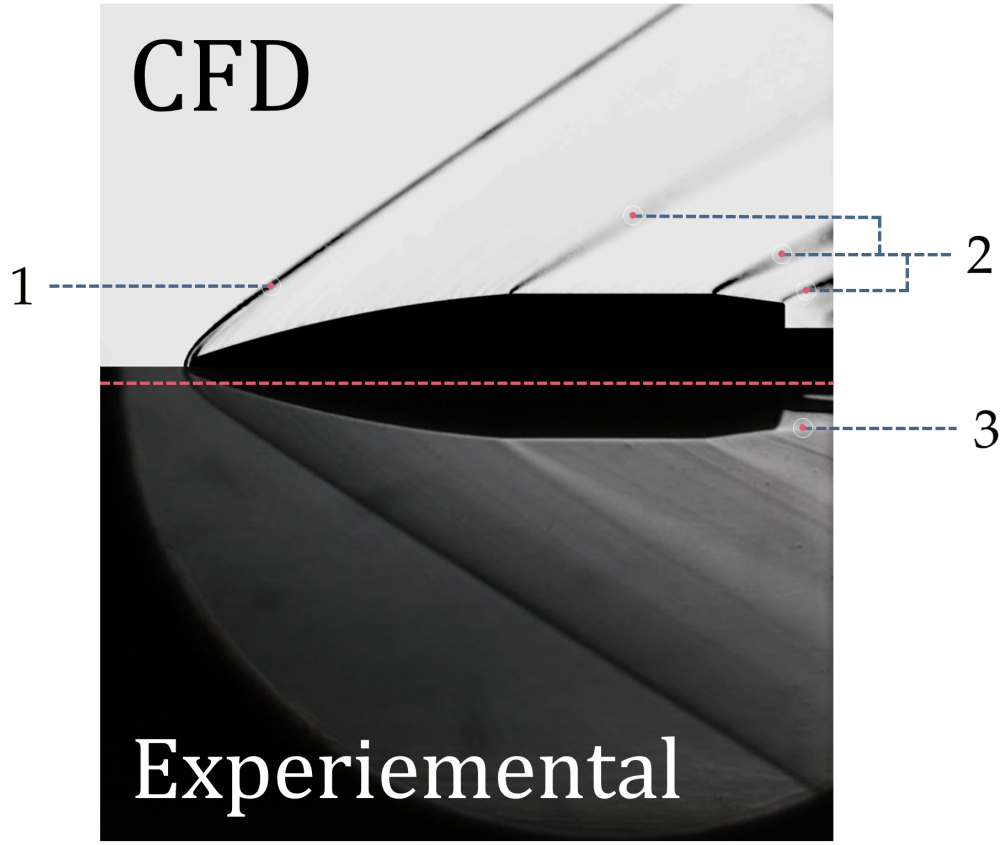

Figure 6.1: Comparison of Schlieren visualization between numerical (CFD) and experimental instantaneous picture, highlighting key flow features : (1) bow shock, (2) expansion waves, and (3) shear layer.

Figure 6.1 first illustrates the detached bow shock around the ogive forebody. Following this, three expansion waves can be observed : the first occurring at the intersection between the ogive and the cylindrical section, the second at the junction between the cylindrical section and the boat-tail, and the third between the boat-tail and the base. Then, the experimental capture clearly highlights the shear layer, which is the region where the high-velocity flow over the projectile surface meets the lower-velocity wake behind it. This interaction creates a layer of intense velocity gradients, leading to significant turbulence. The shear layer forms just aft of the projectile's base, where the airflow separates from the surface and transitions into a turbulent wake.

This first comparison demonstrates good agreement in terms of the angles of shock waves and expansion waves, providing an initial validation between the experimental and numerical solutions. With a qualitative understanding of the flow features, the next step involves a quantitative comparison of wall static pressure measurements to further validate the numerical model.

6.1.2 Wall Static Pressure

The data collected during the wind tunnel tests, which aimed to determine the static pressure along the projectile, were post-processed for normalization and subsequently compared with numerical predictions. To achieve this, the pressures obtained from the pressure taps were normalized by the free stream static pressure, as is standard practice for projectile applications [110]. This reference pressure was measured using the first pressure tap (the most upstream) in the test section along the upper wall of the tunnel. Additionally, the uncertainties associated with these measurements were calculated to assess the reliability of the obtained data. Detailed explanations regarding the computation of these uncertainties are provided in Appendix H. Figure 6.2 highlights the comparison between the experimental data obtained from wind tunnel measurements and the numerically CFD predictions.

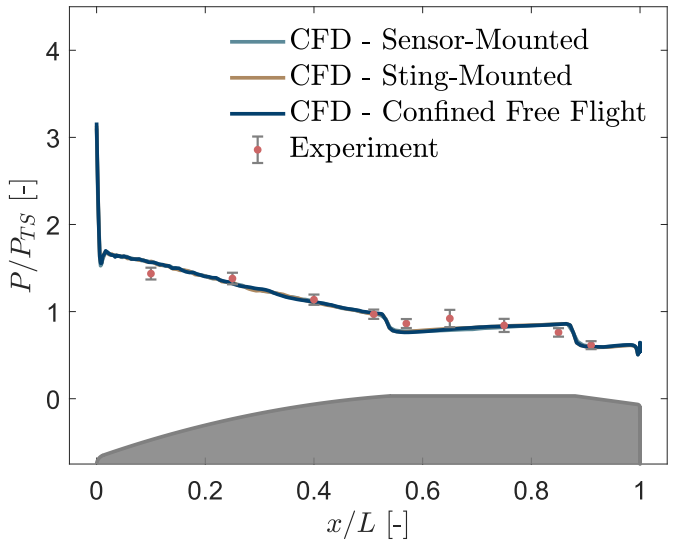

Figure 6.2: Experimental and numerical comparison of the normalized wall static pressure along the NATO 5.56 mm projectile at scale 1.5.

First, Figure 6.2 demonstrates that the numerical results accurately predict the experimental observations. Additionally, the three geometries investigated numerically (confined free-flight, sting-mounted projectile, and sensor-mounted projectile) yield identical pressure distributions along the projectile. This is because the flow is supersonic in the region around the projectile. In such flows, information cannot travel upstream, rendering the downstream setup insignificant to the measurements made on the projectile.

Although the k-ω SST model used in CFD accurately predicts the pressure distribution along the bullet, it is worth noting that even inviscid models, can correctly predict this distribution [110]. Therefore, analyzing quantities that involve viscosity would further enhance confidence in the robustness and reliability of the numerical approach. Nonetheless, this initial comparison has provided valuable confidence in the wind tunnel measurement tools and ensured the consistency of the numerical investigations.

6.1.3 Drag

The primary objective of this study is to extract key aerodynamic factors, such as the aerodynamic coefficients of the projectile, from experimental wind tunnel measurements. A significant advancement in this study was the integration of a sensor able of measuring the forces acting on the projectile. However, these measurements also include contributions from the shield and the sting, though to a lesser extent. Therefore, the advantage of the numerical investigation conducted alongside the experimental campaign is that, once validated by the force measurements obtained in the wind tunnel, it allows isolating the contribution of the projectile alone. The capability of CFD to provide the contribution of the projectile independently is a significant asset for the overall objective of this study.

Consequently, the second quantity compared between experimental and numerical results, which now includes a viscous contribution, is the drag (D). To achieve this, the data obtained from the sensor (Figure 6.3) are compared to the numerical predictions (Figure 6.4).

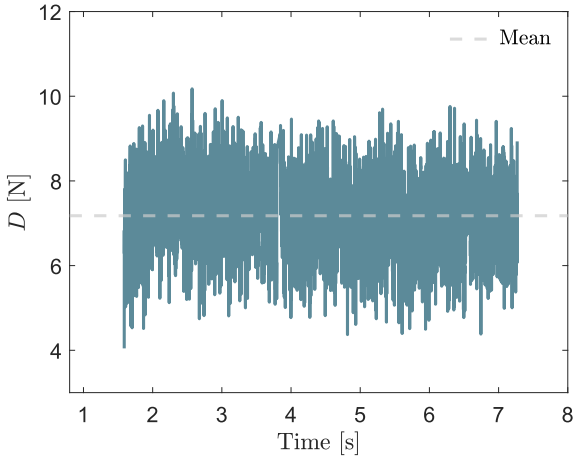

Figure 6.3: Typical sensor output.

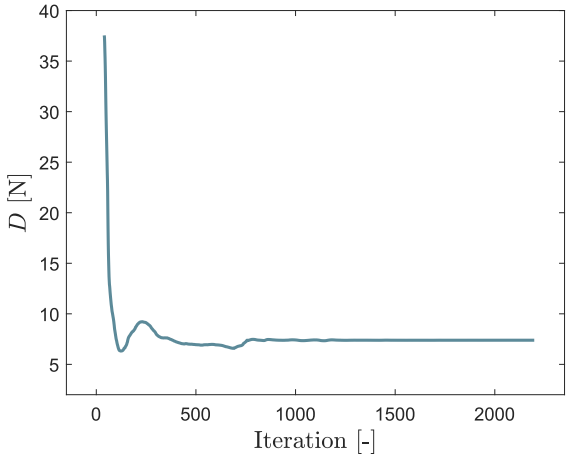

Figure 6.4: k-ω SST prediction.

To acquire a comprehensive set of experiments sufficient to extract a significant number of samples for comparison with numerical predictions, a series of wind tunnel experiments was conducted. Ten of the conducted experiments are depicted in Figure 6.5 alongside the CFD prediction derived from the numerical investigation. It is noteworthy that a tolerance interval of 10% relative to the numerical prediction value has also been plotted to facilitate the interpretation of the figure. Moreover, more detailed explanations regarding the computation of the uncertainties are provided in Appendix H.

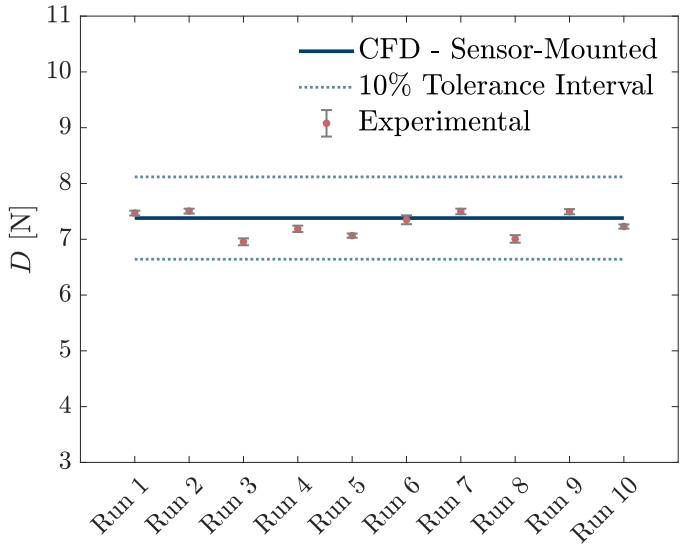

Figure 6.5: Comparison of drag (D) between force balance sensor measurements (10 samples) and numerical prediction.

The comparison between the drag measured by the force balance and the CFD predictions shows a good match. This result increases confidence in the use of the force balance and validates the numerical approach. It was observed during these tests that a significant bias emerged over time. One reason for this offset is the change in temperature and the cooling of the test section during the runs. This aspect needs to be taken into account during test campaigns, and special attention should be given to zeroing the sensor before each measurement session.

Additionally, several tests (not included in Figure 6.5) were conducted with the addition of adhesive tape around the shield and the fastening washer to improve the connection between these two components. However, this resulted in an increase in drag by approximately 1-2 N. This increase appears to be due to the imperfect application of the adhesive tape around the shield, which obstructs the airflow. In the case without adhesive tape, the flow follows the shield's profile, whereas with the adhesive tape, the flow is obstructed by the tape's folds. In

some instances, this even led to the tape detaching during the test, resulting in an immediate halt of the ongoing test. Due to the difficulty in applying the tape without creating folds and the potential detachment during testing, it was decided to abandon this approach.

Drag Breakdown

One of the advantages of the numerical approach is its ability to isolate the contributions of each component. This capability can be used to identify and optimize components that have excessively high contributions to aerodynamic forces. In the present case, it allows for the extraction of the drag on the projectile, and subsequently, the derivation of its drag coefficient, which is a more informative metric. Figure 6.6a presents the drag predicted by CFD for each component, while Figure 6.6b evaluates the contributions of each component to the total drag predicted by CFD (*Force Balance Measurement*: $D_{\text{tot}} = 7.39\,\text{N}$).

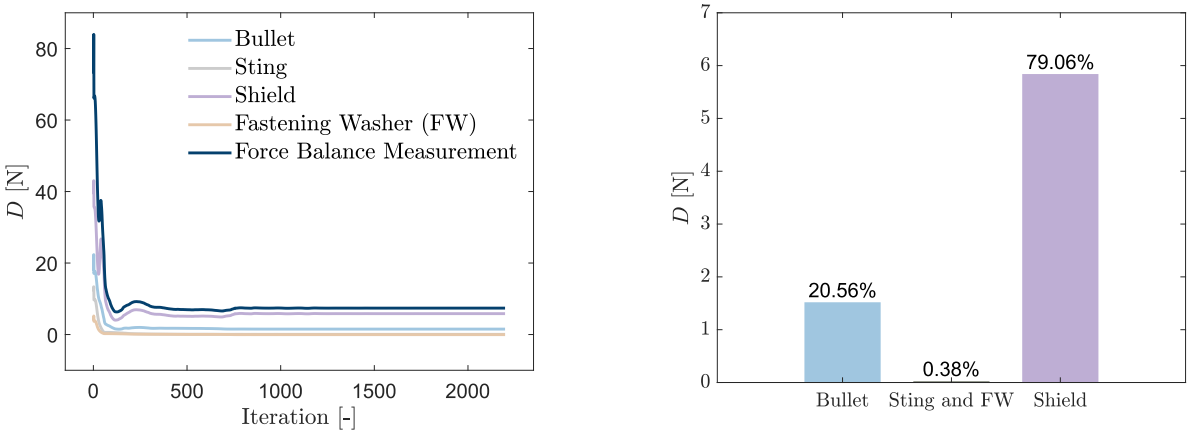

(a) Breakdown of the drag by setup components.

(b) Contributions of each component.

Figure 6.6: Breakdown of the drag (D) obtained from CFD as a function of the setup components and evaluation of their contributions.

First, Figure 6.6b highlights the significant contribution of the shield to the total drag. This outcome was anticipated and is a necessary compromise to prevent sensor saturation. Without this shield, the sensor would saturate, and a strong normal shock would form on the force balance's front face.

Furthermore, it appears that the projectile's contribution is approximately 20%. This result is particularly noteworthy as it implies that if a 1.5-scale projectile is tested at Mach 2, 0° angle of attack, and with a pressure of 268 kPa, the projectile's drag can be estimated at 20% of the experimental measurement. A more in-depth numerical investigation within a speed range

around Mach 2 could study the evolution of this contribution over a broader range of speeds and develop ratios to provide a preliminary estimate of the projectile's drag during wind tunnel tests. It should be noted that, like speed, the influence of pressure is also a parameter potentially worth investigating.

Finally, the contributions of the sting and the fastening washer were combined as their contributions are so minimal that separating them would not provide further insights into the analysis. The fact that these components contribute negligibly to the total drag allows the focus to remain solely on determining the contributions of the shield and the projectile, thereby simplifying future research efforts. Therefore, to obtain an initial estimation, it will be essential to determine the contribution of the shield to deduce that of the projectile, or alternatively, the contribution of the projectile to deduce that of the shield.

Another approach to analyse numerical results is to decompose the drag into its pressure and shear contributions. Figure 6.7a illustrates the pressure and shear contributions of the predicted drag. Figures 6.7b and 6.7c present the sources of drag for the ball and the shield, respectively, which are the most significant contributors to the overall drag. It is important to note that the decomposition of drag for the sting and the fastening washer was not performed because their contributions are negligible to the total drag and consist entirely of shear contribution, with zero pressure contribution.

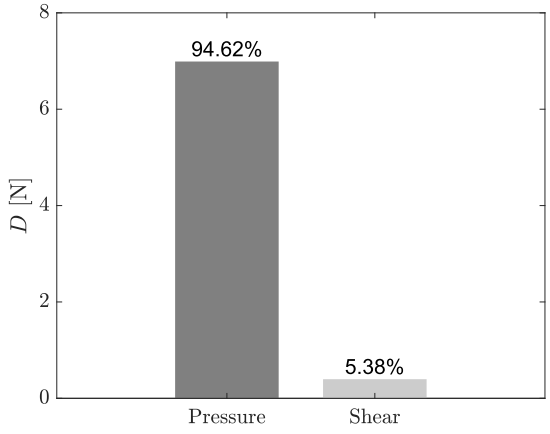

(a) Overall drag decomposition ($D_{\text{tot}} = 7.39\,\text{N}$).

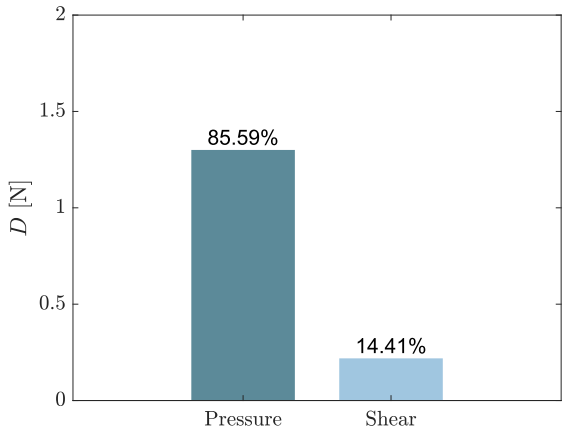

(b) Bullet drag decomposition ($D_{\text{bullet}} = 1.52\,\text{N}$).

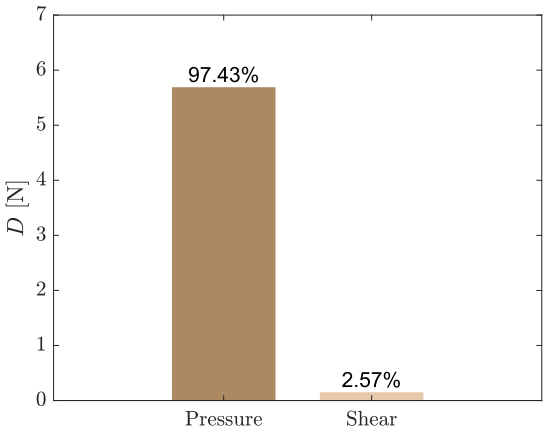

(c) Shield drag decomposition ($D_{\text{shield}} = 5.84\,\text{N}$).

Figure 6.7: Decomposition of drag into its pressure and shear components for (a) the total drag, (b) the bullet, and (c) the shield.

Figure 6.7 highlights the significant contribution of the pressure component to the overall drag. It can also be observed that this contribution is relatively less pronounced for the projectile compared to the shield. This can be attributed to the fact that the projectile has a more streamlined profile than the shield, which induces a larger shear component. It can be suggested that as the fineness ratio of the shield increases, the viscous contribution becomes more significant.

With the drag force accurately measured and validated, attention is now directed towards determining the drag coefficient, a key aerodynamic parameter that provides further insights into the projectile's performance.

6.1.4 Drag Coefficient

Initially, the only data available to validate the numerical results from wind tunnel tests were the wall static pressure and aerodynamic forces. With increased confidence in these results, CFD can now be employed to delve deeper into the study.

The focus is subsequently shifted to the projectile itself, aiming to determine its drag coefficient and compare it with data obtained from an extensive testing campaign conducted by Silton and Howell on firing ranges [122]. The data from this campaign were analyzed using the ARFDAS software [47], which facilitates the extraction of aerodynamic coefficients during flight. This comparison is further supplemented with previous measurements from McCoy [76]. Both testing campaigns were conducted in the Aerodynamic Experimental Fa-

cility (AEF) at the U.S. Army Research Laboratory (ARL) [23]. Given that McCoy's initial aerodynamic data were limited to only seven rounds, Silton & Howell expanded upon this dataset by conducting additional tests.

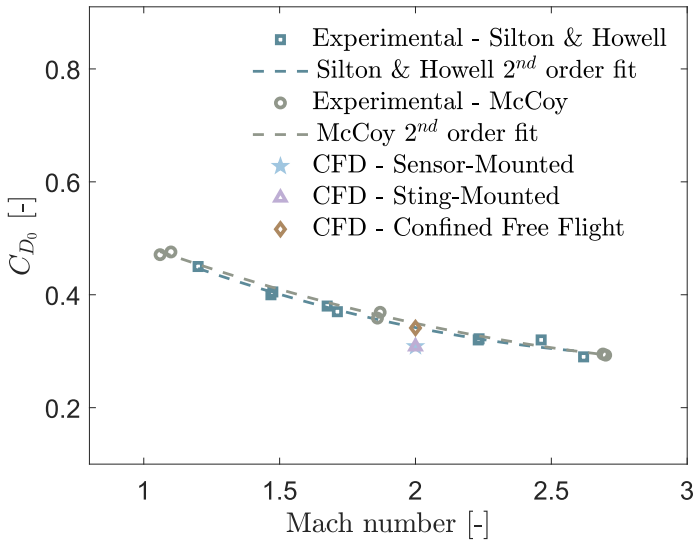

Figure 6.8: Comparison of drag coefficient (C_{D_0}) as a function of Mach Number for experimental data and numerical predictions. The experimental data from Silton & Howell and McCoy are shown alongside their respective second-order fits. Numerical predictions include CFD results for sensor-mounted, sting-mounted, and confined free-flight configurations.

The analysis of Figure 6.8 reveals two key observations. Firstly, there is a discrepancy between the configurations involving a sting and the confined free-flight (CFF) configuration. Consequently, the sting has a significant impact on the aerodynamic measurements. Secondly, it highlights the match of the drag coefficient for the confined free-flight case with the experimental data. This observation provides confidence in the CFD results. Given that the parameters are identical across the three studied geometries (sensor-mounted, sting-mounted, and confined free-flight) except for the mesh refinement in the wake region for the confined free-flight scenario, the same reliability can be attributed to all scenarios considered in the numerical investigation. Table 6.1 presents the experimental drag coefficients along with the numerical predictions.

Table 6.1: Comparison of drag coefficient (C_{D_0}) between experimental data and numerical predictions.

	Experimental		Numerical		
	Silton & Howell	McCoy	Sensor-Mounted	Sting-Mounted	CFF
C_{D_0} [-]	0.3419	0.3494	0.3084	0.3082	0.3412

The successful matching of the confined free-flight configuration with the experimental data not only finalizes the validation of the numerical approach but also provides two additional insights. Firstly, it confirms that the blockage induced by the projectile in the wind tunnel does not lead to side wall effects that could alter the flow and potentially lead to different results. Secondly, this model confirms that the difference in Reynolds number between the free-flight case and the wind tunnel case is negligible. In future investigations, once confidence in handling the wind tunnel has been established, it will be possible to conduct tests at higher pressures and consequently higher Reynolds numbers. At that point, it will be necessary to re-evaluate the influence of Reynolds number on the aerodynamic coefficient.

This fourth and final comparison has enabled the comprehensive validation of the numerical approach. In retrospect, the initial qualitative analysis using Schlieren visualization, the normalized wall static pressure measurements, the drag measurements, and finally the drag coefficient comparisons with test campaigns from the U.S. Army have provided robust support for the validation of the numerical model. With both qualitative and quantitative aspects in agreement, the model can now be used with a high degree of confidence to further extend the study.

6.2 Exploration of the Numerical Model

This section delves deeper into the analysis of the numerical model used in this study. By examining various aspects such as the influence of mounting configurations, the challenges associated with wind tunnel measurements, and the evaluation of lift and pitching moments, this exploration seeks to evaluate the robustness of the computational predictions beyond the quantities already validated. Through this comprehensive examination, valuable insights are obtained into the accuracy and reliability of the numerical model under different experimental conditions.

6.2.1 Analysis of the Mounting Influence

It was observed that a significant difference exists between the drag coefficient of the setups with a sting (sensor- and sting-mounted) and the confined free-flight scenario. Quantitatively, an increase of approximately 10% was observed when the projectile is in confined flight. Analyzing the contributions of pressure and shear (omitted here for brevity), it was found that the shear component remained constant while the pressure component increased, causing this discrepancy. Figure 6.9 illustrates this observation with a much larger low-pressure zone in the case without a sting.

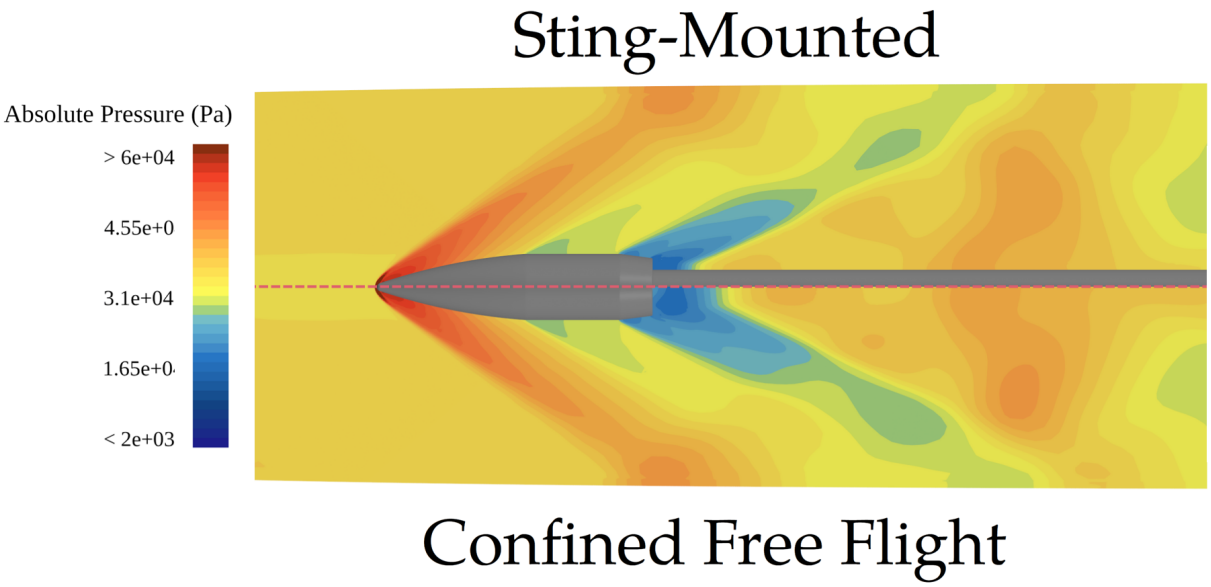

Figure 6.9: Comparison of the absolute pressure between the sting-mounted and confines free-flight scenario.

The increase in drag is explained by the higher pressure in the wake of the projectile when it is mounted on a sting. The sting obstructs the free recirculation of the flow, preventing the pressure drop. This known phenomenon was notably studied in free-flight drag tests of 40 mm shell conducted by the National Advisory Committee for Aeronautics (NACA) for the Ballistic Research Laboratories (BRL) of the U.S. Army [132]. These tests demonstrated a drag reduction at supersonic speeds of approximately 20% by combusting in the wake of the projectile in flight, a technique known as *base bleed*.

The shape of the bullet itself has been studied to minimize drag related to the wake. In ballistics, this contribution is so significant and important to handle that it is separated from the pressure drag of the bullet's profile. The three sources of drag are therefore : pressure drag (excluding the base contribution), skin friction drag, and base drag [33, 115]. The study by

Cummings et al. (1992) aimed to optimize the boat-tail angle, determining it to be 7.5° [33]. Today, this finding has become a standard and is applied to all long-range projectiles.

Challenges in Wind Tunnel Drag Measurements

At the current stage of research conducted at the Royal Military Academy, a method to directly account for this effect in measurements has not yet been developed. As a result, the drag measured in the wind tunnel will always be lower than what is expected in free-flight. To better represent reality, it is necessary to develop a method that accounts for this effect.

Currently, one of the experimental methods being tested involves scaling up the original 5.56 mm NATO projectile. By increasing the scale, the influence of the sting becomes less significant. However, an optimal balance must be found between increasing the scale and the induced blockage ratio. To remain below the 10% blockage ratio threshold, the maximum scale for the projectile that can be tested is 3:1. This would also ensure staying well below the suggested linkage ratio range of 30-50% (ideally under 30%). However, the feasibility of such tests with a larger caliber remains a question. Testing at a larger scale implies achieving a higher Reynolds number for the same imposed pressure. Therefore, it will be essential to ensure that the tests remain within a range of dynamic similarity to compare these results with Silton & Howell and McCoy test campaign data accurately. If the Reynolds number difference proves too significant to ignore, considering a change in scale might be necessary. In this study, all tests were conducted at the recommended pressure, the minimum required to maintain a shock-free test section. Therefore, reducing this pressure to lower the Reynolds number and approximate free-flight conditions might render such tests unfeasible.

Nevertheless, with the knowledge already acquired, analyzing a broader range of speeds could help develop correlations that account for the obstruction effect of the projectile base and the percentage of drag originating from the bullet. This would allow for an approximate drag coefficient value of the tested projectile to be obtained directly from force measurements using the sensor.

6.2.2 Lift and Pitching Moment

This study focuses on the force-balance mounting geometry to gain deeper insights into the experimental setup. This allows for the consideration of any discrepancies relative to the desired free-flight configuration and highlights any necessary precautions to be taken with the setup. These aspects can be accounted for in future explorations.

Although no convergence studies have been conducted on the lift and pitching moment,

the confidence gained during the validation of the model allows for their analysis with a reasonable degree of reliability. To maintain rigour, if future investigations involve non-zero angles of attack and the lift and pitching moment become significant quantities to consider, it will be necessary to include these quantities in the convergence study.

Lift

Following the same analysis procedure used during the validation of the numerical approach, Figure 6.10 illustrates the numerical predictions of the lift, as well as a quantitative evaluation of the contribution of each component. The total lift predicted by the CFD is given by the *Force Balance Measurement* : $L_{\text{tot}} = -2.97\,\text{N}$.

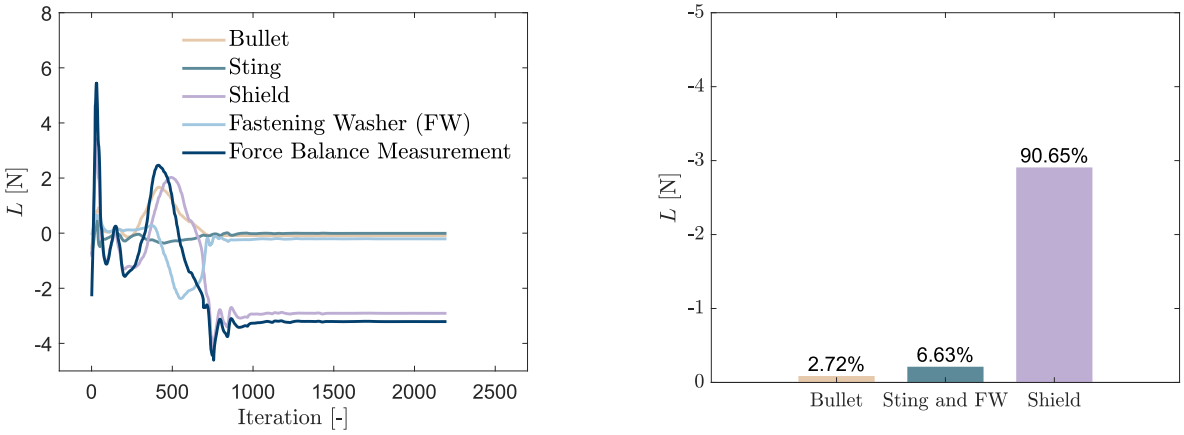

(a) Breakdown of the lift by setup components.

(b) Contributions of each component.

Figure 6.10: Breakdown of the lift (L) obtained from CFD as a function of the setup components and evaluation of their contributions.

First, Figure 6.10a shows that lift requires more iterations to converge than drag. This is likely due to the greater sensitivity of lift to small changes in flow conditions. Figure 6.10b indicates that the majority of the lift is generated by the shield. This can be explained by the asymmetrical positioning i of the setup in the vertical direction within the test section. Consequently, this asymmetry increasingly influences the flow as the cross-section of the shield enlarges.

The contributions of the sting and fastening washer may seem surprising, but these contributions actually stem from the asymmetry of the flow rather than their shape. Finally, the contribution of the projectile is relatively minor, which is advantageous. Despite the setup not being perfectly centered in the test section's height, this asymmetry has a limited impact on the projectile's lift.

Having experimental measurements of lift obtained through the force balance, it is appropriate to compare them with the numerical predictions. However, it is important to note that in this case, there is an uncertainty related to the exact positioning of the force balance in the wind tunnel. Due to constraints associated with the positioning of the force balance cable within the wind tunnel, the sensor had to be oriented at a 45° angle to allow for more space in the test section (Figure 6.11). Although precautions were taken regarding this angle of rotation, uncertainties persist regarding the exact definition of the angle.

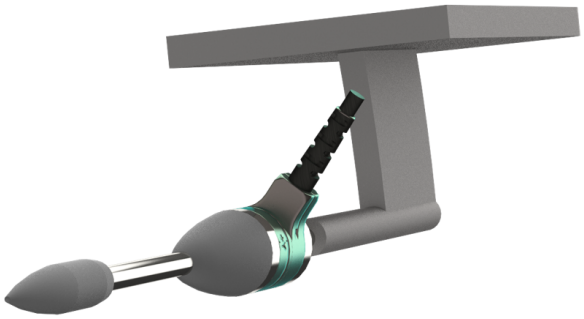

Figure 6.11: Actual orientation of the force balance in the test section, tilted approximately 45° to accommodate the wire of the sensor.

However, this angle is crucial as it allows the derivation of the actual lift from the forces calculated in the balance's reference axes (refer to Figure 4.18). These axis transformations were performed in post-processing, but their uncertainties, being difficult to quantify, were not included in the comparison. A method needs to be defined to account for this properly.

It is also worth noting that this rotation was not considered in the numerical model because it would not have impacted the drag measurements and would not have allowed for the symmetry of the domain to be used. Figures 6.12 and 6.13 respectively present a typical output of the lift measured by the force balance and the lift prediction by the CFD analysis.

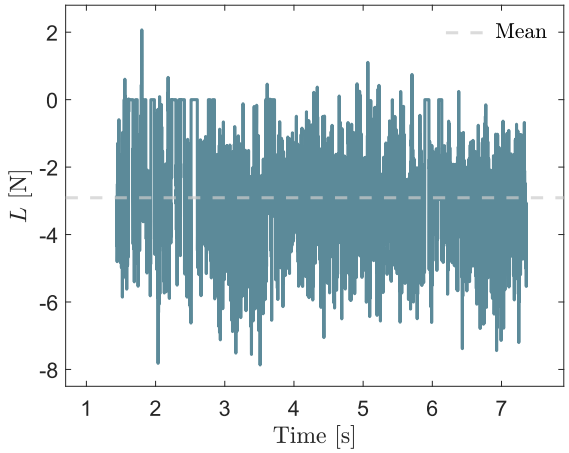

Figure 6.12: Typical sensor output.

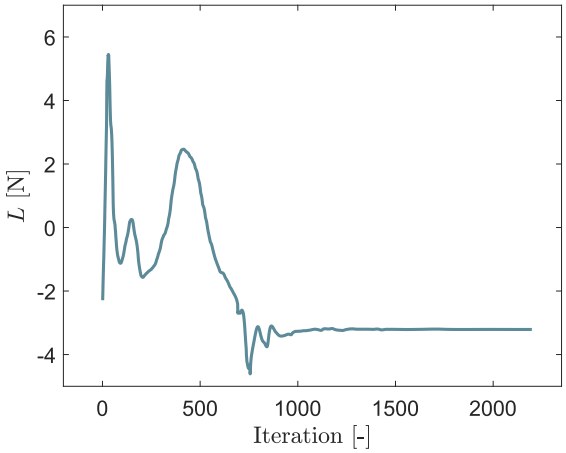

Figure 6.13: k-ω SST prediction.

Both approaches predict a negative lift, which makes sense given that the setup is closer to the upper wall than the lower wall. Consequently, a pressure difference inducing a downforce was expected. Figure 6.14 presents the results obtained for the lift during the test campaign alongside the CFD prediction.

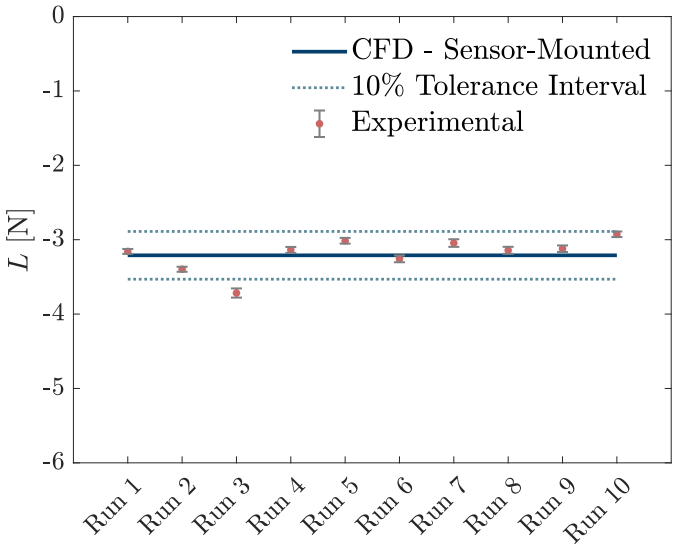

Figure 6.14: Comparison of lift between force balance sensor measurements (10 samples) and numerical prediction.

Although there is higher uncertainty compared to the drag measurements previously investigated, the CFD appears to accurately predict the measured lift. While experimental drag coefficient values are well-documented (fire test campaign), obtaining a comparative sce-

nario in the literature for lift coefficient is challenging, which makes it harder to further validate the model. Ideally, the lift coefficient should be zero for a projectile positioned at a zero angle of attack. However, in this case, a discrepancy arises from the asymmetric positioning of the model.

Nevertheless, this asymmetry in the flow can be evaluated by extracting the lift coefficient of the projectile and deriving the equivalent angle of attack associated with this asymmetry, to ensure it is indeed negligible. Moreover, this evaluation allows us to quantify the "virtual" offset induced by the configuration, *i.e.*, the equivalent angle of attack at which the projectile would need to be placed in free-flight to reproduce the lift observed in the wind tunnel. To achieve this, the data obtained from the extensive testing campaign carried out by Silton and Howell on the firing range were once again used (Figure 6.15).

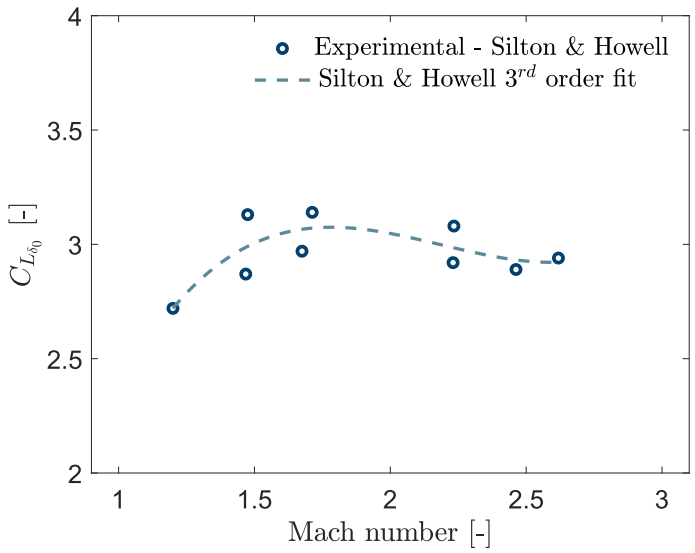

Figure 6.15: Lift force coefficient component as a function of Mach number for the 5.56 mm NATO bullet [122].

Associated with the value of the zero-yaw lift force coefficient derivative $C_{L_{\delta_0}}$ at Mach 2 (Figure 6.15) the numerical prediction of the lift coefficient (Figure 6.16) can be used in Equation 6.1.

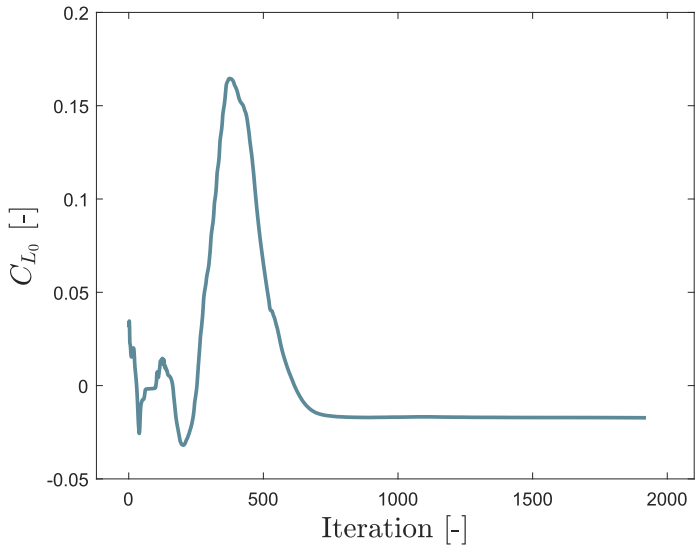

Figure 6.16: Lift coefficient C_{L_0} prediction by CFD.

$$C_L = C_{L_{\delta_0}} \sin \delta \,, \tag{6.1}$$

where $C_{L_{\delta_0}}$ is given by Figure 6.15 and is equal to 3.048 at Mach 2 and where δ is the angle of attack. For the present case, the drag coefficient C_L is defined by the CFD prediction and is equal to $C_L = C_{L_0} = -0.0171$. Therefore, the associate angle of attack is:

$$\delta = \arcsin\left(\frac{C_L}{C_{L_{\delta_0}}}\right) = -0.32^\circ \,. \tag{6.2}$$

The value obtained from Equation 6.2 demonstrates that the asymmetry of the flow in the region of the projectile is of low magnitude. Although this asymmetry is more pronounced in the downstream part of the setup, this result quantifies its effect in the region of interest. The lift coefficient and the associated equivalent angle of incidence can also be used in a subsequent study as a known offset to be subtracted from the measured values. This will be particularly useful when investigating non-zero angles of incidence and when direct extraction of aerodynamic coefficients becomes feasible.

Pitching Moment

Considering the calibration and the current setup configuration, one of the most crucial parameters to monitor is the moments, particularly the pitching moment. The influence of flow asymmetry, although known at the projectile level, induces a significant moment on the sen-

sor due to the lever arm distance separating them. Specifically, there is a distance of 69 mm between the base of the bullet and the origin of force balance calculations (neglecting the distance from the base to the center of pressure of the projectile). Looking forward to future investigations, it is essential to evaluate the pitching moment and the contribution of different components to this parameter.

During the wind tunnel tests, it was found that a significant portion of the challenges encountered were related to the saturation of the balance, particularly the saturation caused by the moments. From a numerical perspective, Figure 6.17 presents the numerical predictions of the different components of the setup, alongside their contributions in terms of percentage of the total pitching moment. The total pitching moment predicted by CFD is given by *Force Balance Measurement*: $P_{\text{tot}} = 47.9\,\text{Nmm}$.

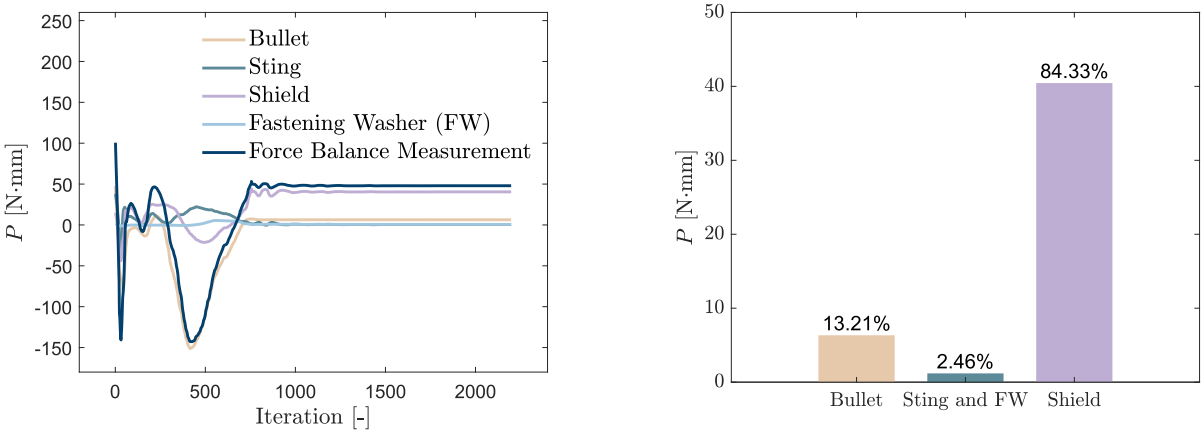

(a) Breakdown of the lift by setup components.

(b) Contributions of each component.

Figure 6.17: Breakdown of the pitching moment P obtained from CFD, evaluating the contributions of individual setup components.

While the numerical analysis of the lift showed that the projectile contributed approximately 3% to the total lift measured by the balance, it contributes 13% in the present case. This result clearly illustrates that even though the lift generated by the projectile is small, it has a much more pronounced effect on the moments calculated by the balance. Although the shield remains the major contributor to the pitching moment, its significant influence is primarily due to the lift generated rather than the lever arm effect, given its proximity to the origin of the balance calculations.

This observation implies that during investigations at non-zero angles of incidence, attention must be paid to both the projectile, which produces less lift but has a long lever arm, and the shield, which produces more lift but has a shorter lever arm. A more detailed study at

different angles of attack could analyze the evolution of these two contributions as a function of the angle of attack.

Figures 6.18 and 6.19 respectively present a temporal response of the balance for the pitching moment and the CFD prediction.

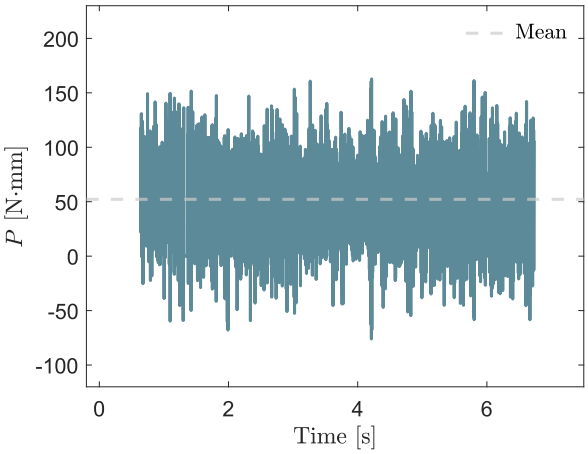

Figure 6.18: Typical sensor output.

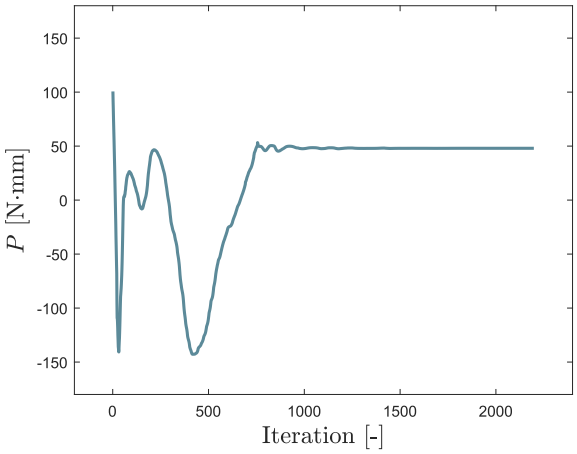

Figure 6.19: k-ω SST prediction.

First, the primary observation that can be made from Figure 6.18 is that the pitching moment has greater uncertainty, given the range of oscillation in its temporal response. Previously, the variation interval relative to the average force $\left|\overline{F}\right|$ was approximately within the following range :

$$\left[\left|\overline{F}\right| - \frac{\left|\overline{F}\right|}{2} \, , \, \left|\overline{F}\right| + \frac{\left|\overline{F}\right|}{2}\right] . \tag{6.3}$$

For the pitching measurement, the average moment $\left|\overline{P}\right|$ falls within the interval :

$$\left[\left|\overline{P}\right| - \frac{3\left|\overline{P}\right|}{2} \, , \, \left|\overline{P}\right| + \frac{3\left|\overline{P}\right|}{2}\right] . \tag{6.4}$$

This increase in the range of variation suggests a higher uncertainty in the pitching moment measurements, as a larger interval indicates greater variability and less stability in the measurements. This also confirms the manufacturer's specifications, which indicated a higher resolution for forces compared to moments. The sensor's resolution, as specified in Table 4.5, was finer for forces and coarser for moments.

This stems from the fact that even a tiny change upstream (even though the steady-state hypothesis remains considered) can have a significant impact on the measurement when the

lever arm is considerable. A potential source of these perturbations could be the rigidity of the setup. A potential improvement strategy could involve increasing the rigidity of the setup by using different materials or opting for a design with few screws connections.

Additionally, it was observed that the setup requires regular inspections, particularly of the front sting and the fastening washer. Every 2-3 tests, it was suggested to verify that the setup was properly tightened and that there was no play between the components. This sensitivity was particularly noticeable when comparing the numerical approach with the experimental measurements (Figure 6.20). However, it is important to note that uncertainty related to the exact orientation of the calculation axes for these forces still persists in the presentation of these data. The interpretation derived from this should be confirmed with a more in-depth study.

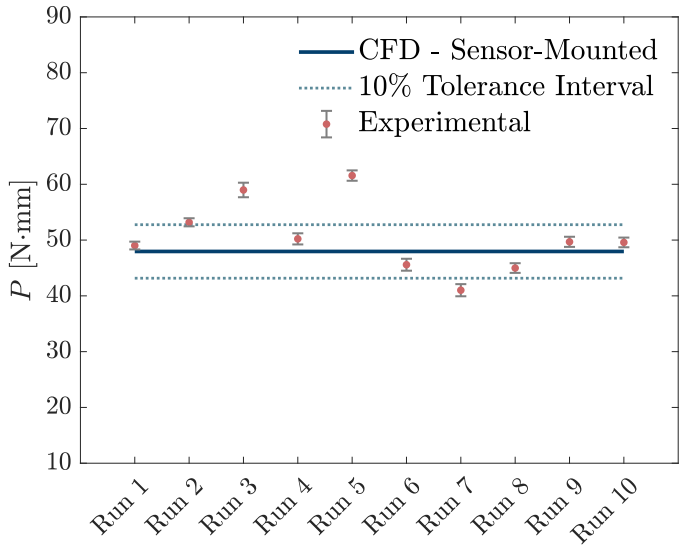

Figure 6.20: Comparison of pitching moment between force balance sensor measurements (10 samples) and numerical prediction.

Figure 6.20 highlights discrepancies more pronounced than those observed in the previous force analysis. Moreover, although the tests were conducted at a 0° angle of attack, it was observed that the force balance occasionally saturated for brief moments during some tests. Generally, it was noted that the accurate determination of moments remains quite challenging at this stage.

Nevertheless, it is still possible to derive meaningful insights. Although the CFD predicts forces well below the sensor's saturation limit of 120 Nmm, for future investigations involving angles of attack, it is recommended to use a sensor with a higher calibration range to keep away the saturation issue.

6.3 Discussion of the Results

This chapter delved into the implications of the results obtained from both experimental and numerical analyses. The focus was on understanding discrepancies observed between different testing configurations, such as sting-mounted versus confined free-flight scenarios, and the impact of these configurations on the measured aerodynamic forces. One key finding was the approximately 10% discrepancy in drag coefficient measurements between sting-mounted and confined free-flight scenarios, attributed to the influence of the sting on the pressure in the projectile's wake. The chapter also explored the challenges encountered during the wind tunnel experiments, including the calibration and resolution limitations of the force balance, and proposed potential solutions for future studies.

The effectiveness of various methodologies employed to isolate and quantify the contributions of individual components to the overall drag and lift forces was discussed, highlighting the significant contribution of the pressure component to the overall drag. The shield was found to have relatively high contributions for both drag and lift (80% and 90%, respectively), a necessary design choice to avoid saturating the sensor, which would have occurred without this shield design. Additionally, the study identified the equivalent angle of attack induced by asymmetry in the test setup, which was found to be -0.32°. This asymmetry was inherent to the positioning of the setup itself and was beyond control. This provides a valuable reference for future investigations at non-zero angles of attack.

The analysis of the numerical model demonstrated its robustness, providing reliable predictions of aerodynamic coefficients and enhancing confidence in the wind tunnel measurement tools. The projectile contributed approximately 20% to the overall drag, a significant result indicating that if a 1.5-scale projectile is tested at Mach 2, 0° angle of attack, and with a pressure of 268 kPa, the drag of the projectile can be estimated at 20% of the experimental measurement. This result supports the potential of further numerical investigations within a speed range around Mach 2 to study the evolution of this contribution and develop ratios to provide preliminary estimates of the projectile's drag during wind tunnel tests.

Further, the decomposition of drag into its pressure and shear components highlighted the dominant role of the pressure component. The contributions of the sting and the fastening washer were combined as their influence was minimal, thus focusing the analysis on the shield and the projectile.

The investigation of lift and pitching moments underscored the need for more precise measurement techniques and potential sensor upgrades. It was observed that the force balance occasionally saturated during tests, particularly for pitching moments. This saturation in-

dicates the necessity for higher calibration ranges and increased setup rigidity, potentially achievable through using different materials or opting for a design with fewer screw connections. These improvements could enhance the accuracy and reliability of future measurements.

In conclusion, this study has significantly advanced the understanding of the aerodynamics of the 5.56 mm NATO projectile, validating the numerical model and highlighting the reliability of the wind tunnel instruments. The insights gained will guide future experimental setups and improve the accuracy of aerodynamic measurements. This study has also built confidence in the wind tunnel flow characteristics, instruments, and force balance, paving the way for more refined and accurate future research.

Part III

Conclusion

Chapter 7 | Conclusion and Overview

7.1 Summary of the Study and Key Findings

The primary goal of this study was to analyze the aerodynamic characteristics of a 5.56 mm NATO projectile using both experimental and numerical methods. This investigation aimed to validate the numerical model and enhance the understanding of projectile aerodynamics under high-speed conditions. The study is particularly relevant given the challenges in extracting accurate aerodynamic coefficients, which are critical for predicting projectile performance.

The research has started with a numerical investigation using Simcenter STAR-CCM+ to simulate the projectile's aerodynamics. This included comprehensive mesh refinement, solver settings, and physical model evaluations to ensure high-fidelity simulations. The numerical analysis was complemented by experimental tests conducted in the newly established wind tunnel at the Royal Military Academy (RMA), using Schlieren visualization, pressure and drag measurements to capture key flow features and validate the numerical results.

Confidence in Tunnel Flow and Instruments

Despite various challenges, the study achieved significant confidence in the wind tunnel's flow characteristics and the instruments used. The comparison of experimental and numerical results demonstrated good agreement, particularly in the pressure distribution along the projectile and drag measurements. The CFD model accurately predicted observed flow features such as shock waves and expansion waves, enhancing the credibility of both the numerical approach and the wind tunnel setup.

Insights into Wind Tunnel Operations

This investigation clarified several aspects related to the newly established wind tunnel at the RMA. By validating the numerical model with experimental data, the study identified areas for improvement in experimental setups and measurement techniques. The findings provide a foundation for future investigations, enabling more precise and reliable studies.

Key Findings

- **Drag Coefficient Analysis**: The numerical and experimental results showed a 10% discrepancy in drag coefficient between sting-mounted and confined free-flight scenarios, attributed to the influence of the sting on the pressure in the projectile's wake.
- **Lift and Pitching Moment**: Numerical predictions indicated minimal lift generated by the projectile, while the shield contributed significantly to total lift and pitching moment due to its asymmetrical positioning within the test section. Despite the bullet having a small lift contribution, it remains critical due to the significant impact on the sensor's moment measurement caused by the lever arm.
- **Drag Decomposition**: The study successfully decomposed the drag into pressure and shear components, providing a detailed understanding of the sources of drag. The shield and bullet were major contributors to the overall drag and lift forces, with the shield being the dominant factor due to its size and positioning (80% for drag and 90% for lift). The projectile's contribution was approximately 20%, implying that the drag of the projectile can be estimated at 20% of the experimental measurement. It was observed that the shield had relatively high contributions for both drag and lift, but this was necessary to avoid saturating the sensor, which would have occurred without the design of this shield.
- **Equivalent Angle of Attack**: The analysis revealed that the setup's asymmetry induced an equivalent angle of attack of -0.32°, providing a useful reference for future investigations involving non-zero angles of incidence.

In conclusion, this study has significantly advanced the understanding of the aerodynamics of the 5.56 mm NATO projectile, validating the numerical model and highlighting the reliability of the wind tunnel instruments. The insights gained will guide future experimental setups and improve the accuracy of aerodynamic measurements. This study has also allowed for gaining more confidence in the wind tunnel flow, wind tunnel instruments, and the force balance. As the tunnel was new, there were many uncertainties regarding these aspects, and this study has helped to clarify and validate them. This study has paved the way for more refined and accurate future research.

7.2 Future Prospects

Extended Speed Range Testing

A primary future exploration is extending the speed range tested at a 0°angle of attack. This will enable the study of the sting's obstruction effect on the projectile's base as a function of Mach number and analyze each component's contribution. The ultimate goal is to develop a correlation to determine the projectile's drag coefficient directly from experimental measurements. This correlation should consider the projectile's contribution percentage to the sensor measurement and a correction factor for sting obstruction. Achieving this will require an extensive experimental campaign and parallel numerical investigation.

Non-Zero Angle of Attack Studies

Another exploration path involves testing at non-zero angles of attack to obtain a complete picture of the 5.56 mm NATO projectile under flight conditions. Although these angles are often smaller than 5°, a preliminary study is necessary to determine the appropriate sensor calibration for accurate testing. Upgrading the sensor calibration range and reducing the sting's length could be combined if needed. When testing at non-zero angles of attack, it will be crucial to develop a methodology to accurately tilt the force balance and assess its orientation.

Higher Inlet Pressure Studies

Exploring the influence of higher inlet pressures in the wind tunnel is another potential avenue. This study focused on a specific case based on the manufacturer's recommended pressure, leaving a broad range of pressures to explore. This would provide a more comprehensive understanding of the projectile under varying density and temperature conditions. Often, shooting range tests cannot control external conditions, while wind tunnel parameters can be precisely modelled.

Scale Effect and Sting Design

Combining the effect of scale by testing larger scales of the 5.56 mm projectile could reduce the sting's influence at the base. This exploration could be paired with a more refined sting design, tapering the base. If the resin used in this study can withstand such loads, 3D printing the projectile, sting, and shield, and as a single piece would allow for a finer design, reducing the linkage ratio and avoiding many screw connections.

Ongoing Research Collaboration

A research project is currently underway at the Royal Military Academy in collaboration with Cranfield University, specifically aimed at studying the scale effects on projectile aerodynamics.

These future prospects outline a path for advancing the understanding of projectile aerodynamics, enhancing the precision of experimental setups, and refining the methodologies used in wind tunnel testing. The insights gained from this study provide a solid foundation for these future explorations, ensuring continued progress in this field of research.

A | Appendix A - Cartridge Naming

The 5.56x45 mm NATO cartridge [101] is named after the nominal dimensions of the *barrel bore* and the *case length*, **not** the actual bullet diameter. This is a common naming convention in firearms and ammunition, where the first number represents the caliber of the barrel bore (Figure A.1), and the second number represents the case length. The use of a slightly larger bullet diameter allows for a tight fit within the barrel, providing stabilization during flight.

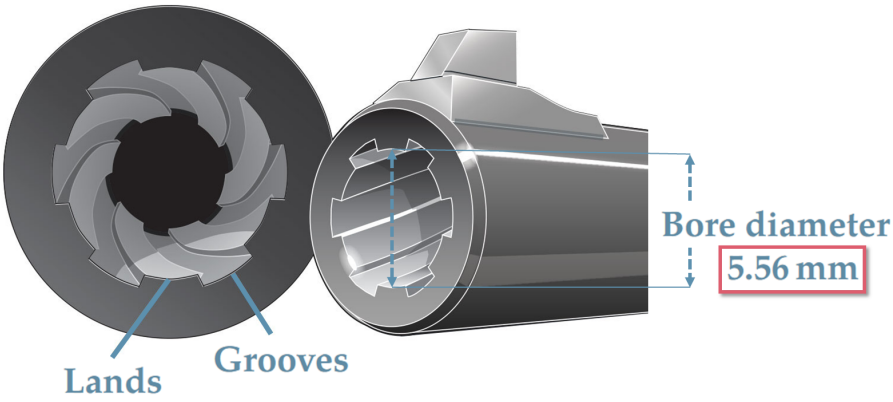

Figure A.1: Close-up view of barrel rifling showing the barrel bore diameter (5.56 mm) [42].

Rifling in firearm barrels involves spiral grooves that impart a spin to the bullet, providing stabilization and enhancing accuracy. The choice of the right twist rate is crucial and depends on factors such as ammunition range and user requirements. Overstabilization, resulting from an excessively high twist rate, can impact aerodynamic efficiency and alter trajectory dynamics, affecting accuracy. Striking a balance in twist rates is essential to avoid both understabilization and overstabilization, ensuring optimal projectile performance [40].

B | Appendix B - Tunnel Dimensions

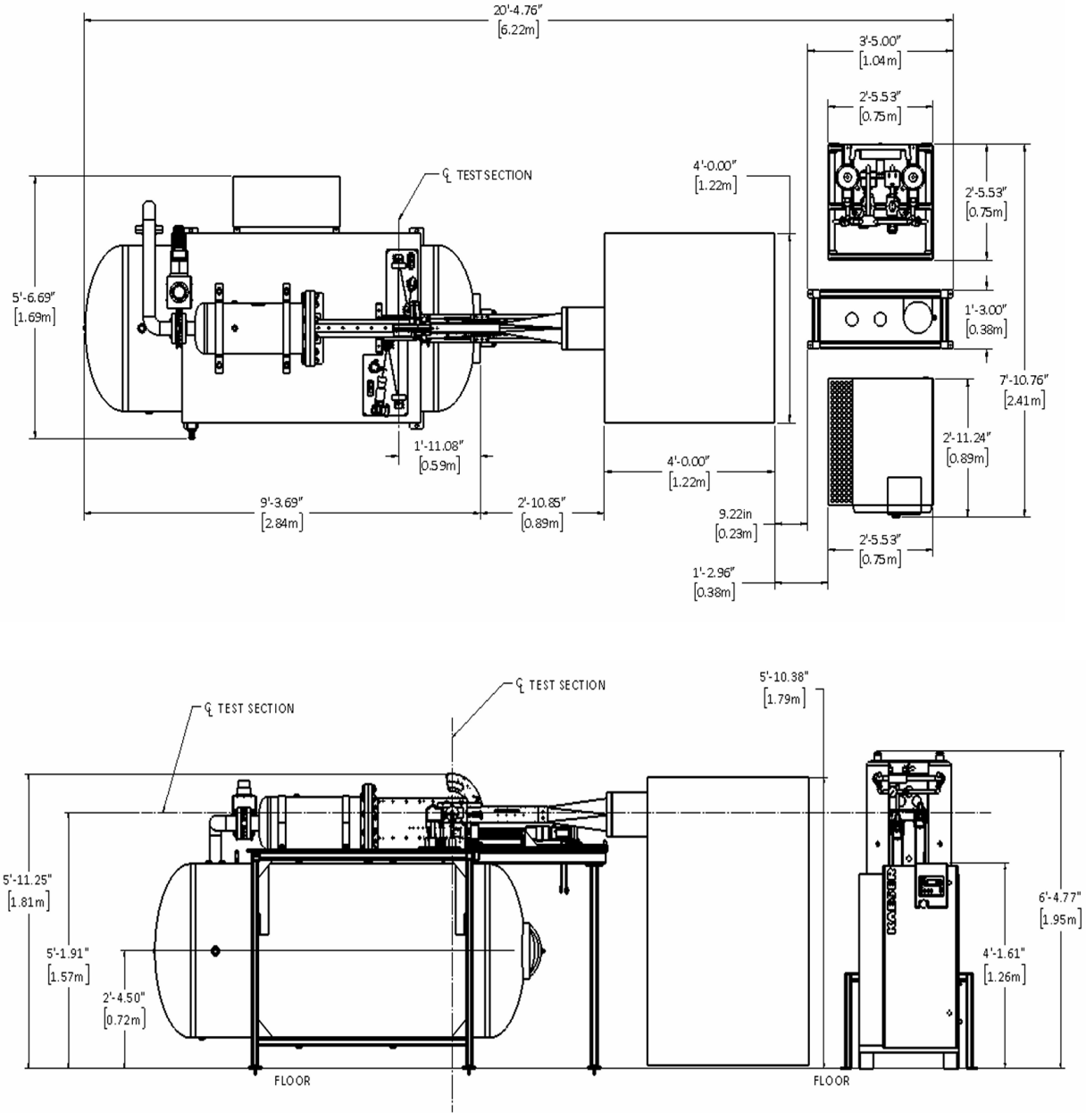

Figure B.1: Wind tunnel dimensions, taken from [3].

C | Appendix C - 3D Printer Resin

Grey Resin (V4)

Table C.1: Grey Resin (V4) properties for raw and post-cured samples [2].

	Raw Piece	Post-Cured
Tensile Properties		
Ultimate Tensile Strength	38 MPa	65 MPa
Tensile Modulus	1.6 GPa	2.8 GPa
Elongation at Break	12 %	6 %
Flexural Properties		
Flexural Modulus	1.3 GPa	2.2 GPa
Impact Resistance Properties		
Notched Izod	16 J/m	25 J/m
Thermal Properties		
Heat Deflection Temp. at 1.8 MPa	43°C	58°C
Heat Deflection Temp. at 0.45 MPa	50°C	73°C

D | Appendix D - Nano 17-E

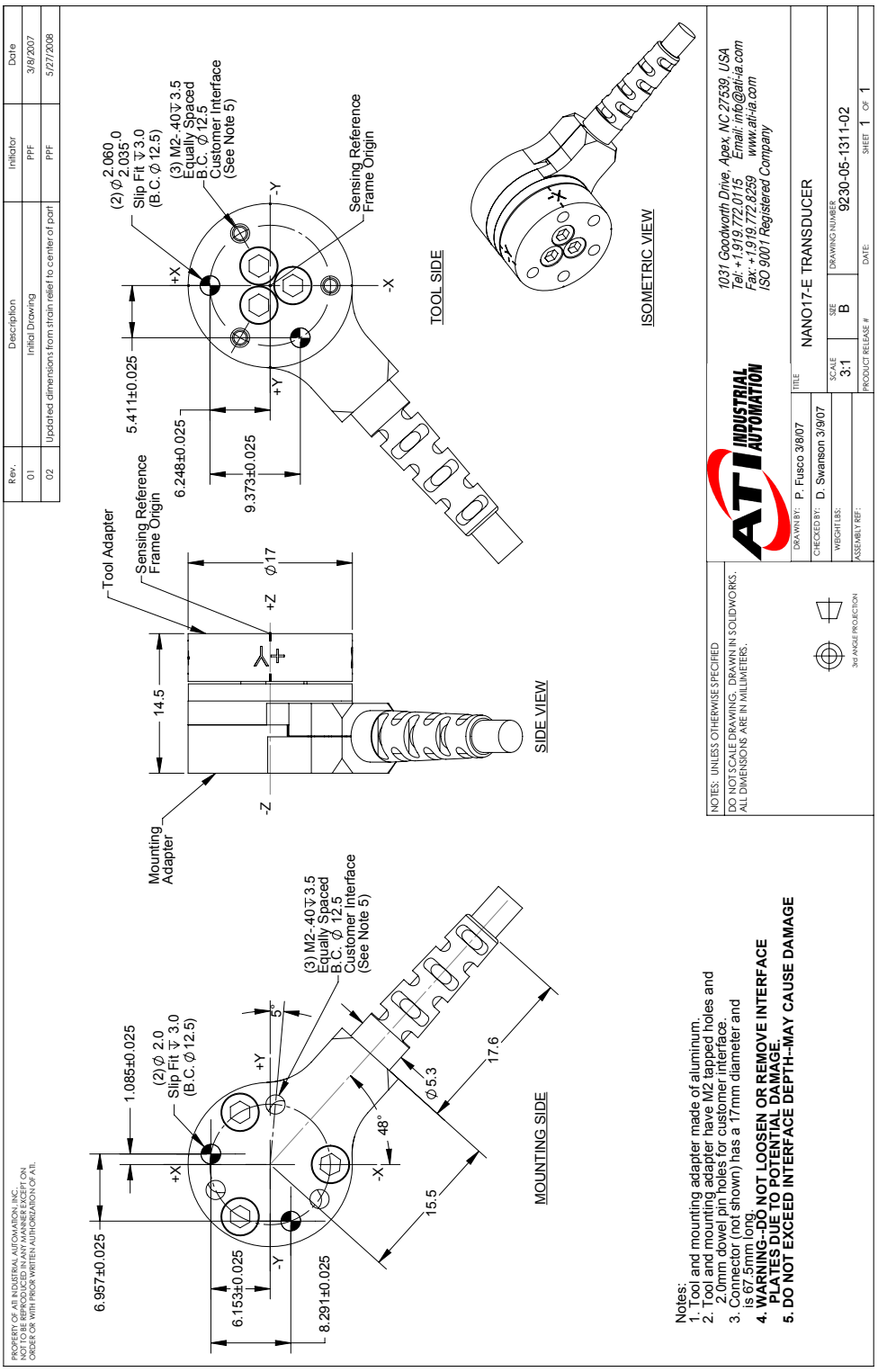

Figure D.1: Nano17-E Tranducer engineering drawing.

E | Appendix E - Physics and Solver

E.1 Viscosity model - Sutherland's Law

The **Sutherland**'s law for viscosity is a well-suited model 3for high-speed compressible flows as it accounts for the variation of viscosity with temperature. Indeed, in such flows, temperature changes significantly due to compression and expansion effects, and the Sutherland law provides a more accurate representation of viscosity under these varying thermal conditions. The Sutherland law relates dynamic viscosity to temperature, allowing it to capture the temperature sensitivity of viscosity (Equation E.1).

$$\mu = \mu_0 \left(\frac{T}{T_0}\right)^{3/2} \frac{T_0 + S}{T + S}, \tag{E.1}$$

where

- T is the static temperature in K;
- T_0 is the reference temperature in K;
- μ_0 is reference viscosity in kg/m-s;
- S is the Sutherland constant [1] in K.

For the *Three Coefficient Method*, the reference viscosity $\mu_0 = 1.716\,10^{-5}\,\mathrm{kg/(m \cdot s)}$, the reference temperature $T_0 = 273.11\,\mathrm{K}$, and the Sutherland constant $S = 110.56\,\mathrm{K}$ [119].

E.2 k-ω SST model - Compressibility Correction

Most turbulence models are derived based on incompressible flow assumptions. However, at high Mach numbers, density variations significantly affect the structures of turbulent flow, necessitating specific corrections. One critical aspect is modifying the turbulence dissipation to account for dilatation-induced dissipation.

In Simcenter STAR-CCM+, the **compressibility correction** is used to describe this dilatation-dissipation as a function of the turbulent Mach number M_t [117]. When compressibility correction is enabled, the coefficients β and β^* are replaced as follows :

$$\beta_{\text{comp}} = \beta - \beta^* \xi^* F(M_t)\,, \tag{E.2}$$

$$\beta^*_{\text{comp}} = \beta^* \Big[1 + \xi^* F(M_t)\Big]\,, \tag{E.3}$$

[1] The Sutherland constant is an empirical constant (effective temperature) specific to the gas being considered. It characterizes the temperature dependency of the gas's viscosity.

where β^* is given by the constant k-ω Model Coefficient, $\xi^* = 1.5$ is a model coefficient, and $F(M_t)$ is the compressibility function defined as:

$$F(M_t) = \max\left[0, M_t^2 - \left(\frac{1}{4}\right)^2\right], \tag{E.4}$$

where

$$M_t^2 = \frac{2k}{c^2}, \tag{E.5}$$

with k is the turbulent kinetic energy and c the speed of sound.

E.3 Algebraic Multigrid - F-Cycle

The F-cycle is a variant of the W-cycle. This cycle involves fewer coarse-level sweeps than the W-cycle but more than the V-cycle.

V Cycle

The V-cycle is the simplest type of fixed cycle, and only has two legs. In the first leg, one performs a number of relaxation sweeps on the finest level and transfers the residuals to the next level. Then, the operation is repeated on successively coarse levels until the coarsest level is reached. A coarse "grid" generally contains only a few "cells". After finishing the sweeps on the coarsest level, the solution is used to correct the solution on the next finer level. Some relaxation sweeps are performed on that level before repeating the process until the finest level is reached. This procedure is illustrated in Figure E.1.

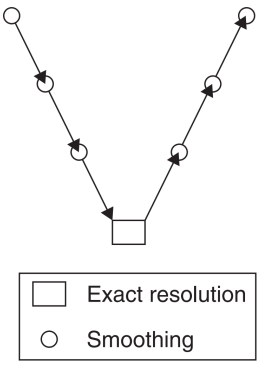

Figure E.1: Multigrid strategies on a four-grid method (V-cycle), taken from [62].

W Cycle

For stiff systems, the V-cycle sometimes is not sufficient, and more coarse iterations are advantageous. The W-cycle increases the number of coarse relaxation sweeps as illustrated in Figure E.2.

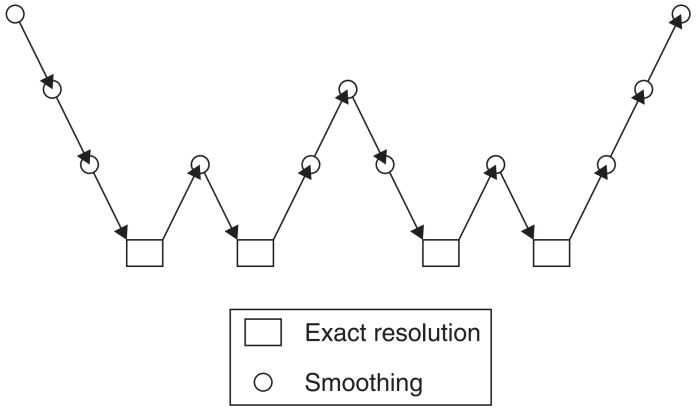

Figure E.2: Multigrid strategies on a four-grid method (W-cycle), taken from [62].

F Cycle

The F-cycle is a variant of the W-cycle. This cycle involves fewer coarse-level sweeps than the W-cycle but still more than the V-cycle. This cycle is particularly efficient for handling complex error components in the solution process, ensuring faster and more robust convergence with lower computational demand compared to the W-cycle.

F | Appendix F - Mesh Quality Metrics

Face Validity

Face validity is a measure of how correctly the face normals of a cell align with their attached cell centroid (Figure F.1). In cells with good quality, the face normals point outward, away from the cell centroid. Conversely, in cells with poor face validity, one or more face normals point inward, toward the cell centroid. A face validity value of 1.0 indicates that all face normals correctly point away from the cell centroid. Values below 1.0 indicate that some face normals point inward, suggesting some concavity. Values below 0.5 indicate a negative volume cell. Cells with face validity below 1.0 are considered poor quality.

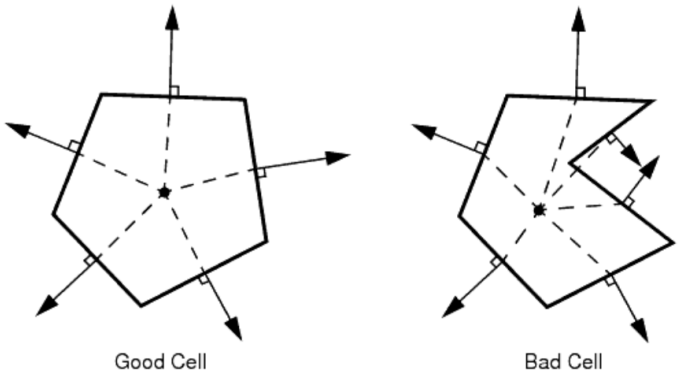

Figure F.1: Face Validity, taken from [119].

Cell Quality

The cell quality metric is calculated using a hybrid of the Gauss and least-squares methods for cell gradient calculation. It evaluates not only the relative geometric distribution of cell centroids of neighbouring faces but also the orientation of the cell faces (Figure F.2). Typically, flat cells with highly non-orthogonal faces have lower cell quality.

A perfect cell has a quality of 1.0. Cubic cells are an example of perfect cells, but other polyhedral shapes can also have high cell quality. Conversely, a degenerate cell has a quality approaching zero. Cells with a quality less than 1.0e-5 are considered poor quality.

The cell quality metric is particularly important for three-dimensional meshes. While low cell quality may still provide a valid solution depending on the selected physics, it can adversely affect both the robustness and accuracy of the solution.

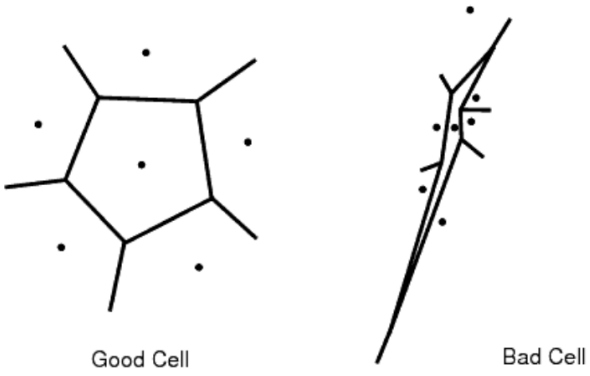

Figure F.2: Cell Quality, taken from [119].

Volume Change

The volume change metric compares a cell's volume to that of its largest neighbour (Figure F.3). A value of 1.0 means the cell's volume is equal to or larger than its neighbours. A decrease in volume relative to neighbours, such as with sliver (cell with extremely poor aspect ratio, very elongated or degenerated) or flat cells, can be flagged using this metric. Large volume disparities between cells can lead to inaccuracies and solver instability. Cells with a volume change of 0.01 or lower are considered bad.

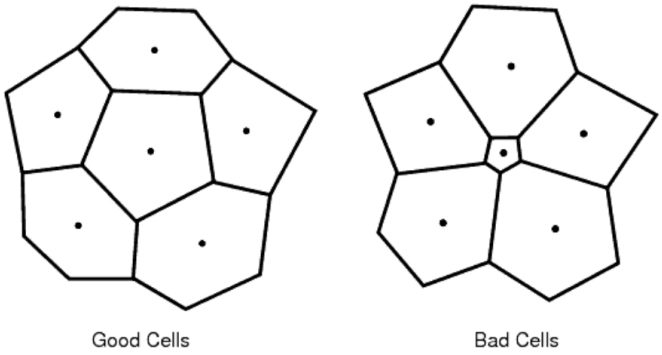

Figure F.3: Volume Change, taken from [119].

Cell Skewness Angle

The cell skewness angle measures whether adjacent cells permit diffusion of quantities without them becoming unbounded. It is calculated as the angle θ between the face normal **a** and the vector connecting the centroids of adjacent cells $d\mathbf{s}$ (Figure F.4). A skewness angle of zero indicates a perfectly orthogonal mesh. Cells with a skewness angle greater than 85°are considered bad.

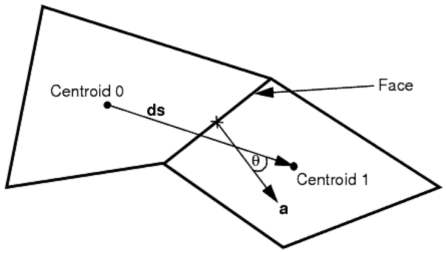

Figure F.4: Cell Skewness angle, taken from [119].

Chevron Quality Indicator

Chevron cells are pairs of thin slender cells that meet at a common face but have a particular orientation (Figure F.5). The chevron quality norm c determines whether a cell qualifies as a chevron cell [1]. Chevron cells are marked as 1.0, while all other cells are marked as 0. Chevron cells are considered bad cells.

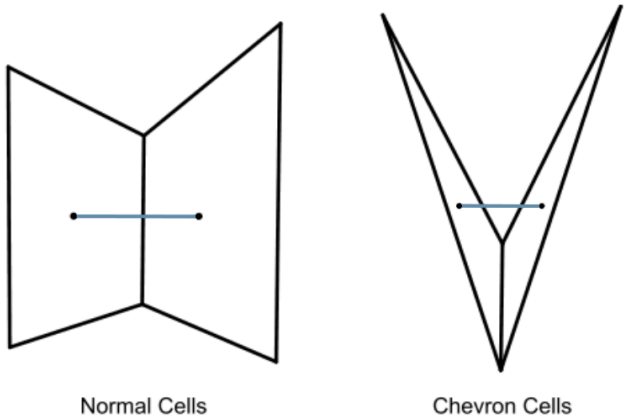

Figure F.5: Chevron Quality, taken from [119].

[1] More detailed explanations regarding the computation of this quantity are provided in [119].

Least Squares Quality

The least square quality indicates the quality of a cell based on the physical location of its centroid relative to the centroids of its face-neighbours (Figure F.6). A perfect cell has a Least Squares Quality of unity. Cells with a least squares quality less than 1.0×10^{-3} are considered bad [2].

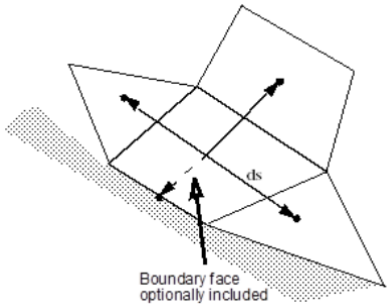

Figure F.6: Least Squares Quality, taken from [119].

Cell Warpage Quality

The cell warpage quality identifies thin and warped cells (Figure F.7), which can cause issues for flow solvers. The warpage quality is based on the measured cell warpage angle of the face [3]. The latter is non-linearly scaled and transformed into the cell warpage quality, which ranges from 0 (worst warpage) to 1 (no warpage). Cells with a cell warpage quality lower than 0.15 (corresponding to a cell warpage angle of 50°) are considered bad cells. In general, the smaller the cell warpage angle, the better the quality. Only cells with an aspect ratio smaller than 0.2 can have a warpage quality less than 1.0.

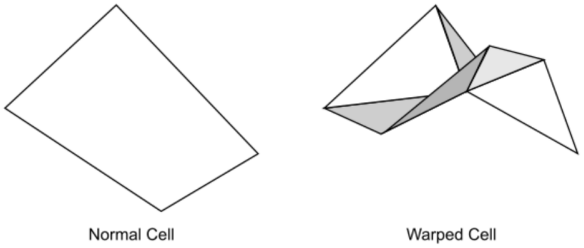

Figure F.7: Cell Warpage Quality, taken from [119].

[2] More detailed explanations regarding the computation of this quantity are provided in [119].
[3] More detailed explanations regarding the computation of this quantity are provided in [119].

G | Appendix G - Mesh Overview

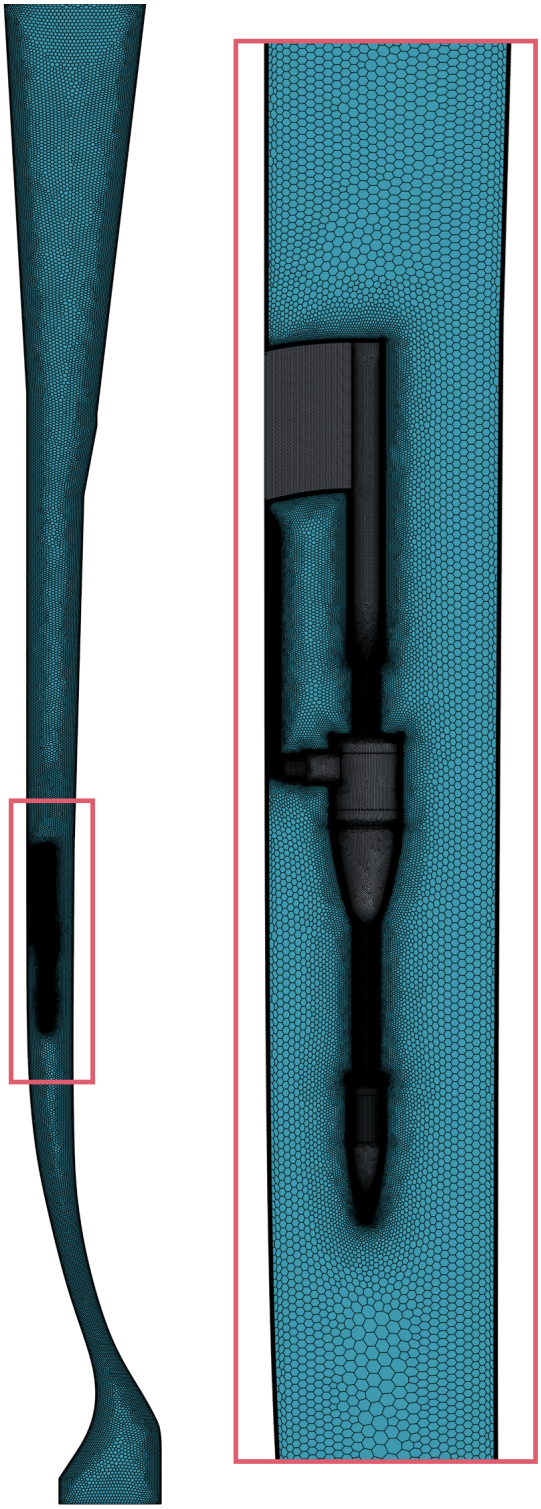

Figure G.1: Wind tunnel mesh with a close-up view of the test section.

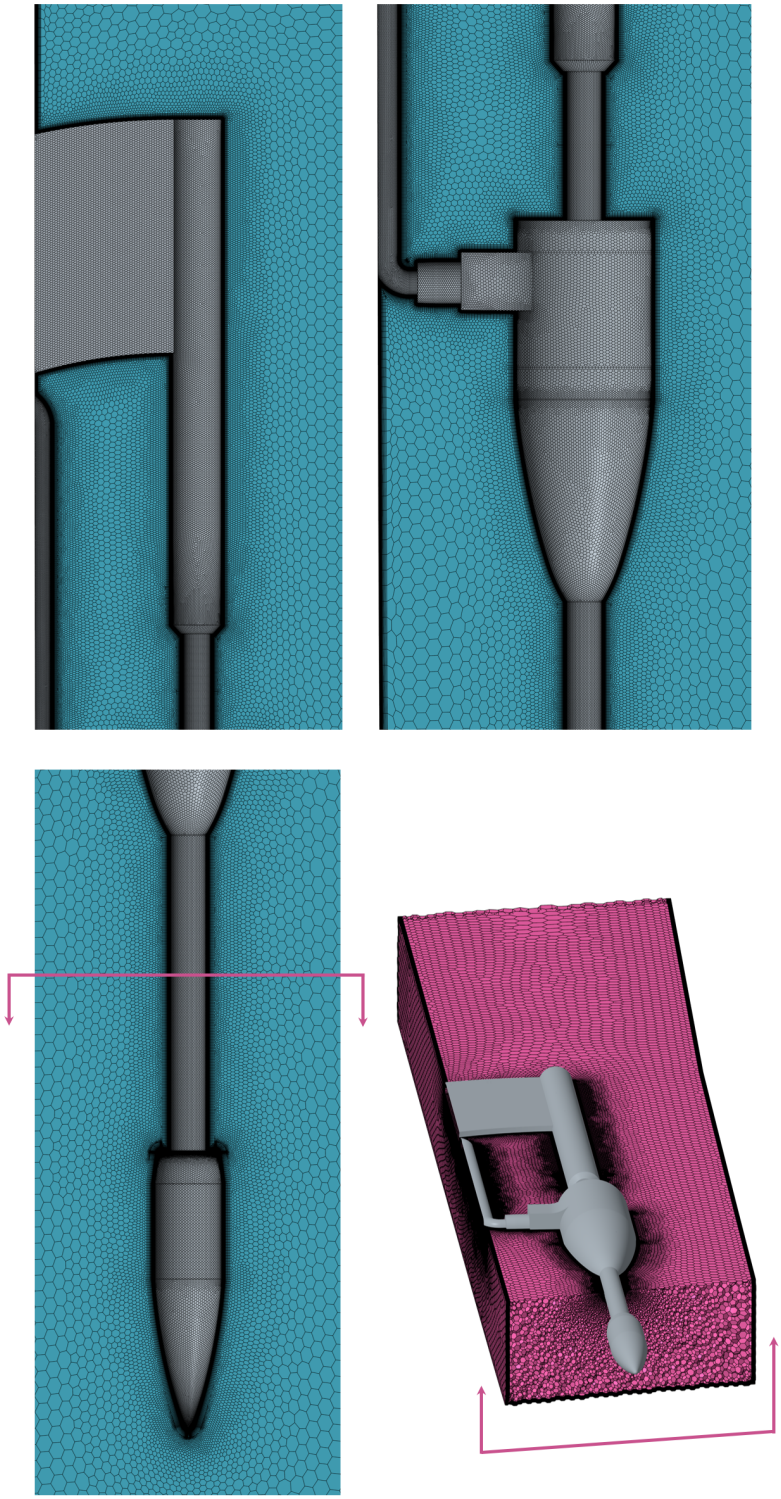

Figure G.2: Close-up view of the bullet, force balance, and model positioning support. The image includes a transverse cut of the front sting, showing the core mesh in a portion of the computational domain.

H | Appendix H - Uncertainty

This Appendix is mainly based on [44].

Uncertainty Measurement in Wind Tunnel Testing

1. **Data Acquisition and Signal Processing**
   During the wind tunnel tests, temporal signals of the measured pressures and forces are collected during 6-10 seconds.

2. **Statistical Analysis**
   For each force component and pressure measurement, the mean μ and standard deviation σ of the sampled data are computed. These statistical measures provide insight into the central tendency and variability of the measurements :

$$\mu = \frac{1}{N} \sum_{i=1}^{N} x_i \,, \tag{H.1}$$

$$\sigma = \sqrt{\frac{1}{N-1} \sum_{i=1}^{N} (x_i - \mu)^2} \,, \tag{H.2}$$

   with N is the number of samples, and where x_i represents each individual measurement.

3. **Uncertainty Estimation**
   The standard uncertainty u of each force component and pressure measurement is estimated directly from the standard deviation of the measurements :

$$u = \sigma \,. \tag{H.3}$$

4. **Incorporating Systematic Uncertainty**
   Systematic uncertainties u_s arise from consistent errors affecting all measurements equally, such as calibration errors or instrument inaccuracies. To account for these, the systematic uncertainties are combined with the random uncertainties using the *root-sum-square method* :

$$u_{\text{total}} = \sqrt{u^2 + u_s^2} \,. \tag{H.4}$$

5. **Expanded Uncertainty**
   To express the uncertainty with a higher level of confidence, the expanded uncertainty U is calculated using a coverage factor k (Equation H.5). Typically, a coverage factor of $k = 2$ is used to achieve approximately 95% confidence.

$$U = k \cdot u_{\text{total}} \,. \tag{H.5}$$

This methodology ensures a comprehensive and accurate assessment of the uncertainties in both force and pressure measurements, enhancing the reliability and credibility of the aerodynamic data obtained from wind tunnel testing.

Bibliography

[1] Form 3+ - Formlabs. https://formlabs.com/3d-printers/form-3/, . (Accessed on 2024-04-11).

[2] Technical Data Sheet - Formlabs (General Purpose Resins). https://formlabs-media.formlabs.com/datasheets/1801089-TDS-ENUS-0.pdf, . (Accessed on 2024-04-11).

[3] *2 inch Supersonic Wind Tunnel (SSWT) Operating Handbook and Manufacturer Approved Instrument Operating Manual*. AEROLAB, 2023. Wind Tunnel Facility: Royal Military Academy Belgium.

[4] M. A. Aguirre, R. Bracco, F. Milanese, and M. Meroniuc. Design of an external six-component wind tunnel balance with floating frame. *International Journal of Aerodynamics*, 2018.

[5] M. Albisser. *Identification of aerodynamic coefficients from free flight data*. PhD thesis, Université de Lorraine, 2015.

[6] G. . Ammo. M855 Green Tip Ammunition. https://www.gunsandammo.com/editorial/m855-green-tip-ammunition/249490, 2015. (Accessed on 2024-02-24).

[7] Andersenman. Nose Cone Haack Series. https://commons.wikimedia.org/wiki/File:Nose_Cone_Haack_Series.svg, 2013. (Accessed on 2024-03-26).

[8] J. D. Anderson. Ludwig Prandtl's Boundary Layer. *Physics Today*, 58(12), 2005. doi: 10.1063/1.2169443.

[9] J. D. Anderson. *Fundamentals of Aerodynamics*. McGraw-Hill Education, 6th edition, 2016.

[10] ApexO. ApexO Firing System (AFS). https://www.apexo.ca/en/products.

[11] Applied Ballistics. Consulting - hardware/software integration. https://appliedballisticsllc.com/consulting/.

[12] Applied Ballistics LLC. Softawre/Hardware. https://appliedballisticsllc.com/.

[13] Army Materiel Command Alexandria VA. *Engineering Design Handbook: Design for Control of Projectile Flight Characteristics*. Army Materiel Command, Alexandria, VA, 1966.

[14] Arrow Tech. Arrow Tech Software Products. http://www.prodas.com/Documents/Arrow%20Tech%20Software%20Products%20Catalog%20June%202013.pdf. (Accessed on 2024-03-06).

[15] ATA Engineering. Introduction to Hypersonic Aerodynamics and CFD Simulation using STAR-CCM+. https://www.ata-e.com/wp-content/uploads/2022/02/ATAEngineering_STARCCM_Hypersonics_Webinar.pdf, 2022. (Accessed on 2024-03-11).

[16] ATI Industrial Automation. Nano17 Force/Torque Sensor. https://www.ati-ia.com/products/ft/ft_models.aspx?id=Nano17. (Accessed on 2024-04-11).

[17] ATI Industrial Automation. Force/Torque Sensor FAQ. https://www.ati-ia.com/library/documents/FT_FAQ.pdf, 2020. (Accessed on 2024-04-08).

[18] G. Balakalyani and G. Jagadeesh. An accelerometer balance for aerodynamic force measurements over Hypervelocity Ballistic models in shock tunnel. 136:636–646, 2019. ISSN 0263-2241. doi: 10.1016/j.measurement.2018.12.099.

[19] G. Baum, J. Baum, D. Hayward, and B. MacKay. Gunshot Wounds: Ballistics, Pathology, and Treatment Recommendations, with a Focus on Retained Bullets. *Orthopedic Research and Reviews*, 14:293–317, 2022. doi: 10.2147/ORR.S378278.

[20] P. Belthori. Ammo 7.62mm x 51mm nato. Sketchfab, 2022. Licensed under Creative Commons Attribution 4.0 International License (http://creativecommons.org/licenses/by/4.0/).

[21] Berger Bullets. What is a Bullet BC? https://bergerbullets.com/nobsbc/what-is-a-bullet-bc/.

[22] M. G. Blevins, G. W. Lyons, M. J. White, and C. R. Hart. Optical and Acoustical Separation and Identification of Ballistic Noise Signatures. Technical Report ERDC TR-21-1, U.S. Army Engineer Research and Development Center (ERDC), 2021.

[23] W. F. Braun. The Free Flight Aerodynamic Range. Technical Report BRL Report No. 1048, U.S. Army Ballistics Research Laboratory, Aberdeen Proving Ground, MD, 1958.

[24] S. Bullets. Doppler Radar Method. https://www.sierrabullets.com/exterior-ballistics/2-3-3-doppler-radar-method/#:~:text=Doppler%20radar%20tracks%20the%20bullet,computer%20using%20very%20sophisticated%20software, 2020.

[25] D. E. Burns and P. A. Parker. Additively Manufactured Wind-Tunnel Balance. *Journal of Aircraft*, 57(5):958–963, 2020.

[26] D. E. Burns, P. A. Parker, B. D. Phillips, T. L. W. III, and D. Landman. Wind Tunnel Balance Design: A NASA Langley Perspective. Technical Report NASA/TM–2020-220570, Langley Research Center, Hampton, Virginia and Old Dominion University, Norfolk, Virginia, 2020.

[27] G. T. Chapman and D. B. Kirk. A Method for Extracting Aerodynamic Coefficients from Free-Flight Data. *AIAA Journal*, 8(4):753–758, 1970.

[28] S. S. Chin. *Missile Configuration Design*. McGraw-Hill, New York City, 1961.

[29] C.-K. Choi. Wind Tunnel Blockage Effects on the Aerodynamic Behavior of Bluff Body. Technical report, Department of Civil Engineering, KAIST, Korea, 1998.

[30] G. R. Cooper and K. S. Fansler. Yaw Card Influence on Stability and Yaw Growth for Spin-Stabilized Projectiles. Technical Report ARL-TR-1431, Army Research Laboratory, 1997.

[31] D. D. Corriveau. System Modeling of a 40 mm Automatic Grenade Launcher. In *International Infantry & Joint Services SMALL ARMS SYSTEMS Symposium*. Flight Mechanics Group/Precision Weapons Section, 2009.

[32] P. G. Cross and M. R. West. Simulation of hypersonic flowfields using star-ccm+. Technical report, Aeromechanics and Thermal Analysis Branch, Weapons Airframe Division, Naval Air Warfare Center Weapons Division, 2019.

[33] R. M. Cummings, H. T. Yang, and Y. H. Oh. Supersonic, Turbulent Flow Computation and Drag Optimization for Axisymmetric Afterbodies. Technical Report NASA TM-108424, NASA Ames Research Center, 1992.

[34] D. Damljanović and D. Vuković. Supersonic Wind Tunnel Tests of a Standard Model at High Angles of Attack. *7th European Conference for Aeronautics and Space Sciences (EUCASS)*, 2017.

[35] V. de Briey. *Small-Caliber Exterior Ballistics: Aerodynamic Coefficients Determination by CFD*. PhD thesis, Royal Military Academy and University of Liège, 2021.

[36] H. Demailly. *Identification des coefficients aérodynamiques d'un projectile à partir de mesures prises en vol*. PhD thesis, Université d'Orléans, 2011.

[37] Z. T. Deng, X. Qian, and D. Pett. Prediction of Chamber Pressure for a Mach 4 Su-

personic Wind Tunnel. *International Journal of Modern Engineering*, 13:45–50, 2012. Alabama A&M University, AeroLab LLC.

[38] J. DeSpirito and K. R. Heavey. CFD Computation of Magnus Moment and Roll Damping Moment of a Spinning Projectile. Technical Report ARL-RP-131, U.S. Army Research Laboratory.

[39] G. Doig, T. J. Barber, E. Leonardi, A. J. Neely, and H. Kleine. Aerodynamics of a supersonic projectile in proximity to a solid surface. *University of New South Wales, Sydney, Australia*, 2010.

[40] M. Driels. *Advanced Weaponeering- Third Edition, Volume 2*. AIAA Education Series, 2020. pp. 53–71.

[41] P. A. Durbin and B. A. P. Reif. *Statistical Theory and Modeling for Turbulent Flows*. John Wiley & Sons, Ltd, 2nd edition, 2010.

[42] C. C. Ed. Rifling in the handgun bore. https://www.concealedcarry-ed.com/montana/studyGuide/Rifling-in-the-Handgun-Bore/801026_12665/.

[43] G. E. Erickson. Overview of Supersonic Aerodynamics Measurement Techniques in the NASA Langley Unitary Plan Wind Tunnel. Technical Report NASA/TM-2007-214894, Langley Research Center, Hampton, Virginia, 2007.

[44] I. Farrance and R. Frenkel. Uncertainty of Measurement: A Review of the Rules for Calculating Uncertainty Components through Functional Relationships. *Clin Biochem Rev*, 33(2):49–75, May 2012.

[45] J. T. P. Fernandes. Design of a Wind Tunnel Force Balance. Master's thesis, Instituto Superior Técnico (IST) - ULisboa, 2018.

[46] M. A. M. A. Ferreira. Design of a Six-Component External Wind Tunnel Balance. Master's thesis, Instituto Superior Técnico (IST) - ULisboa, 2015.

[47] M. Fischer and W. Hathaway. Aeroballistic Research Facility Data Analysis System (ARFDAS). Technical Report AFATL-TR-88-48, Air Force Armament Laboratory, 1988.

[48] FN America. FN Elity - Ballistic Calculator. https://fnamerica.com/products/e-novation-military/fn-elity-ballistic-calculator/.

[49] FN Herstal. 12.7x99mm Ammunition (NATO Cartridges). https://fnherstal.com/en/defence/ammunition/127x99mm/,.

[50] FN Herstal. FN Elity - Ballistic Calculator. https://fnenovation.eu/products/aiming/fn-elity-ballistic-calculator/,.

[51] FN Herstal. 7.62x51mm Ammunition (NATO Cartridges). https://fnherstal.com/en/defence/ammunition/762x51mm/, .

[52] FN Herstal. FN MAG - 7.62X51 mm. https://fnherstal.com/en/defence/portable-weapons/fn-mag/, .

[53] FN Herstal. FN SCAR-H PR. https://fnherstal.com/en/defence/portable-weapons/fn-scar-h-pr/, .

[54] D. Fortier. Hornady Heat Shield: More Than Just Hype. https://www.firearmsnews.com/editorial/hornady-heat-shield-more-than-just-hype/77876, 2015. (Accessed on 2024-03-06).

[55] E. Gagnon and A. Vachon. Comparison of Computer Codes for Projectile Trajectory Simulation. In *31st International Symposium on Ballistics*, volume 1, pages 591–605, Hyderabad, India, 2019. doi: 10.12783/ballistics2019/33097.

[56] Gary A. Crowell Sr. Comparison of drag characteristics of various nose cone shapes in the transonic to low-mach regions. https://en.wikipedia.org/wiki/Nose_cone_design#/media/File:Nose_cone_drag_comparison.svg, 2020. (Accessed on 2024-03-26).

[57] S. A. Ghika and L. A. Penela Guerrero. Mechanical Design, Analysis, and Manufacturing of Wind Tunnel Model and Support Structure, 2021.

[58] R. H. M. Giepman. *Flow Control for Oblique Shock Wave Reflections*. PhD thesis, Technische Universiteit Delft, June 2016.

[59] P. Gnemmi et al. Flowfield Around Spike-Tipped Bodies for High Attack Angles at Mach 4.5. *Journal of Spacecraft and Rockets*, 40(5):622–631, 2003. doi: 10.2514/2.6910.

[60] M. Gonzalez, J. M. Ezquerro, V. Lapuerta, A. Laveron, and J. Rodriguez. Components of a Wind Tunnel Balance: Design and Calibration. In J. Colman Lerner, editor, *Wind Tunnels and Experimental Fluid Dynamics Research*. InTech, 2011. ISBN 978-953-307-623-2.

[61] Heckler & Koch. GMG - Heckler & Koch. https://www.heckler-koch.com/en/Products/Military%20and%20Law%20Enforcement/40%20mm%20systems/GMG?section=overview&s=true, (Accessed on 2024-03-11).

[62] C. Hirsch. *Numerical Computation of Internal and External Flows*. Butterworth-Heinemann, 2007.

[63] Interface. Interface Supports Wind Tunnel Testing. https://www.interfaceforce.com/interface-supports-wind-tunnel-testing/.

[64] Interface | Force Measurement Solution. Wind Tunnel Testing - Multi-Axis. https://interfaceforce.co.uk/wind-tunnel-testing-multi-axis/.

[65] Kestrel Meters. Kestrel Elite Weather Meter with Applied Ballistics. https://kestrelmeters.com/products/kestrel-elite-weather-meter-with-applied-ballistics.

[66] Leica Camera. Leica Rangemaster CRF 2800.COM. https://leica-camera.com/en-GB/sport-optics/rangemaster/crf/rangemaster-crf-2800/shop-now.

[67] Leica Hunting Blog. Leica's First Ever Bluetooth Compact Rangefinder - Rangemaster CRF 2800.COM. https://leica-hunting-blog.com/leicas-first-ever-bluetooth-compact-rangefinder-rangemaster-crf-2800-com/.

[68] R. Lieske and R. McCoy. Equations of Motion of a Rigid Projectile. Technical Report BRL Report 1244, Aberdeen Proving Ground, MD, 1964.

[69] R. Lieske and M. Reiter. Equations of motion for a modified point mass trajectory. Technical Report BRL report 1314, Aberdeen Proving Ground, MD: BRL, 1966. Accession Number: AD0485869.

[70] B. Litz. A Better Ballistic Coefficient. Technical report, Applied Ballistics, 2021.

[71] B. Litz. Aerodynamic Drag Modeling for Ballistics. Technical report, Applied Ballistics, 2021.

[72] B. G. Marinus. *Multidisciplinary Optimization of Aircraft Propeller Blades*. PhD thesis, Royal Military Academy, 2011.

[73] D. Martinez, C. Meaurio, D. Alviso, J. Chaparro, E. Vargas, and J. C. Rolon. Design and Implementation of an Aerodynamic Balance in a Subsonic Wind Tunnel and Validation Through Numerical and Experimental Investigations of Lift and Drag Performances on Airfoils. *Proceedings of ENCIT 2016: 16th Brazilian Congress of Thermal Sciences and Engineering*, 2016.

[74] R. K. Matthews and R. W. Rhudy. Hypersonic Wind Tunnel Test Techniques. Technical Report AEDC-TR-94-6, Calspan Corporation/AEDC Operations, 1994.

[75] R. L. McCoy. "MC DRAG" - A Computer Program for Estimating the Drag Coefficients of Projectiles. Technical Report ARBRL-TR-02293, US Army Armament Research and Development Command, Ballistic Research Laboratory, 1981.

[76] R. L. McCoy. Aerodynamic and Flight Dynamic Characteristics of the New Family of 5.56 mm NATO Ammunition. Technical Report BRL-MR-3476, US Army Ballistic Research Laboratory, 1985.

[77] R. L. McCoy. *Modern Exterior Ballistics - The Launch and Flight Dynamics of Symmetric Projectiles*. Schiffer Military History, 1999.

[78] MeasureX. Load Cells vs. Strain Gauges: Exploring the Differences and Benefits. https://www.measurex.com.au/load-cells-vs-strain-gauges/, 2023. (Accessed on 2024-03-24).

[79] F. R. Menter. Two-equation eddy-viscosity turbulence models for engineering applications. *AIAA Journal*, 32:1598–1605, 1994.

[80] K. Mukaiyam, K. Suzuki, T. Miyazaki, and H. Sawada. Aerodynamic properties of an arrow: Influence of point shape on the boundary layer transition. *Procedia Engineering*, 13:265–270, 12 2011.

[81] C. Murphy. The Measurement of Non-Linear Forces And Moments By Means of Free Flight Tests. BRL Report 974, Ballistic Research Laboratory, 1956.

[82] NASA. Similarity Parameters. https://www.grc.nasa.gov/WWW/k-12/airplane/airsim.html, 2021.

[83] NASA. Model Mounts. https://www.grc.nasa.gov/www/k-12/airplane/tunbalmnt.html, 2021. (Accessed on 2024-02-06).

[84] NASA. Types of Wind Tunnels. https://www.grc.nasa.gov/www/k-12/airplane/tuntype.html, 2021. (Accessed on 2024-02-06).

[85] NASA. Blowdown Wind Tunnel. https://www.grc.nasa.gov/www/k-12/airplane/tunblow.html, 2022. (Accessed on 2024-02-06).

[86] NASA and Defence Research Establishment. *Ballistic-Range Technology*. Number AGARDograph No. 138. 1970. Edited by Thomas N.Canning, Alvin Seiff and Carlton S.James.

[87] NASA Glenn Research Center. Wind Tunnel Balance - External Force Balance. https://www.grc.nasa.gov/www/k-12/airplane/tunbalext.html, 2021.

[88] NASA Glenn Research Center. Wind Tunnel Balance - Internal Force Balance. https://www.grc.nasa.gov/www/k-12/airplane/tunbalint.html, 2021.

[89] NASA Glenn Research Center. Wind Tunnel Testing. https://www.grc.nasa.gov/www/k-12/airplane/tuntest.html, 2021.

[90] NASA Glenn Research Center. Force Balance. https://www.grc.nasa.gov/www/k-12/airplane/tunbal.html, 2021.

[91] NASA Glenn Research Center. Wind Tunnel Balance - Idealized Force & Moment Balance. https://www.grc.nasa.gov/www/k-12/airplane/tunbalfomo.html, 2021.

[92] National Advisory Committee for Aeronautics (NACA). Characteristics of nine research wind tunnels of the Langley Aeronautical Laboratory. 1957.

[93] National Defense Magazine. Army Serious About Fielding 6.8 Caliber Round. 2018. (Accessed on 2024-02-29).

[94] NATO. Procedures to Determine Field Artillery Muzzle Velocity Management, Interchangeability and Prediction. STANAG 4500, 1998. (Classified).

[95] NATO. The 6/7 Degrees of Freedom Guided Projectile Trajectory Model. STANREC 4618, 2016. (Classified).

[96] NATO. The Lieske Modified Point Mass and Five Degrees of Freedom Trajectory Models. STANAG 4355, 2017. (Classified).

[97] NATO Allied Engineering Publication (AEP). The Six/Seven Degrees of Freedom Guided Projectile Trajectory Model - Edition A. AEP 96, 2016. (Classified).

[98] NATO Allied Ordnance Publication (AOP). *Firing techniques to determine ballistic data for fire control systems - Edition C, Version 1*, 2013. AOP-65. (Classified).

[99] NATO Allied Ordnance Publication (AOP). *The Lieske Modified Point Mass and Five Degrees of Freedom Trajectory Models - Edition A, Version 1*, 2017. AOP-4355. (Classified).

[100] NATO Science and Technology Organization (STO). AeroFI, NATO Technical Shareable Software (NTSS) for the Determination of Aerodynamic Coefficients- Version 1.3. AOP 53. (Classified).

[101] NATO Standardization Office (NSO). Multi-Calibre Manual of Proof and Inspection (M-CMOPI) for NATO Small Arms Ammunition, Edition A Version 1. Technical report, Allied Engineering Publication, 2020. (Available).

[102] B. D. News. Eastern breeze 23: Un défi à plusieurs niveaux. https://beldefnews.mil.be/eastern-breeze-23-un-defi-a-plusieurs-niveaux/?lang=fr, 2023.

[103] P. Denis (ONERA). Le code de prévision aérodynamique de l'ONERA:"MISSILE". In *RTO (Research and Technology Organization) Meeting Proceedings 5 - Missile Aerodynamics*. NATO. Session 5: Prediction Methodology. Sorrento, Italy, 1998.

[104] W. Pelham Phillips, G. J. Brauckmann, J. R. Mico, and W. C. Woods. Experimental Investigation of the Aerodynamic Characteristics for a Winged-Cone Concept. 1987.

[105] A. Pope. Wind-Tunnel Calibration Techniques. Technical Report 54, Sandia Corporation, 1961.

[106] A. Pope and L. W. Goin. *High-Speed Wind Tunnel Testing*. John Wiley & Sons, New York, 1965.

[107] L. Prandtl. *Verhandlungen des dritten internationalen Mathematiker-Kongresses in Heidelberg 1904*. Teubner, Leipzig, Germany, 1905. English trans. in *Early Developments of Modern Aerodynamics*, J. A. K. Ackroyd, B. P. Axcell, A. I. Ruban, eds., Butterworth-Heinemann, Oxford, UK (2001), p. 77.

[108] RealPars. What is a Load Cell? | Types of Load Cells. https://www.realpars.com/blog/load-cell, 2019.

[109] Red Bull. Kjeld Nuis Sets Speed Skating Record at 103 kph. https://www.redbull.com/int-en/kjeld-nuis-speed-skating-record-103-kph, 2022. (Accessed on 2024-03-24).

[110] R. P. Reklis and W. Sturek. Surface pressure measurements on slender bodies at angle of attack in supersonic flow. Technical Report ARBRL-MR-02876, US Army Armament Research and Development Command, Ballistic Research Laboratory, 1978.

[111] J. Robert and O. Adiémar. *La Balistique extérieure*. Gauthier-Villars, 1934.

[112] M. Robinson, J. M. Schramm, and K. Hannemann. An Investigation into Internal and External Force Balance Configurations for Short Duration Wind Tunnels. *Spacecraft Section, German Aerospace Center*, 2007.

[113] Royal Military Academy. Computing Cluster at the Royal Military Academy. https://www.rma.ac.be/en/information-for/research-partners/facilities, .

[114] Royal Military Academy. Researchers at the RMA - Laboratories. https://www.rma.ac.be/en/information-for/students/future-students/academic/researchers-at-the-rma/laboratories, . (Accessed on 2024-04-24).

[115] J. Sahu. Drag Predictions for Projectiles at Transonic and Supersonic Speeds. Memorandum Report BRL-MR-3523, US Army Ballistic Research Laboratory, Aberdeen Proving Ground, Maryland, 1986.

[116] T. Sailaranta and A. Siltavuori. AeroFi – Technical Report. Technical Report T-255, HUT Laboratory of Aerodynamics, 2008. (Unpublished).

[117] S. Sarkar, G. Erlebacher, M. Y. Hussaini, and H. O. Kreiss. The analysis and modelling of dilatational terms in compressible turbulence. *Journal of Fluid Mechanics*, 227:473–493, 1991.

[118] L. R. Shooting. Environmental effects. https://www.longrangeshooting.org/articles/long-range-shooting-10-ballistics-tips-for-better-accuracy.

[119] Siemens Digital Industries Software. *Simcenter STAR-CCM+ User Guide*, 2022. Version 2206.

[120] Siemens Digital Industries Software. Simcenter STAR-CCM+. https://plm.sw.siemens.com/en-US/simcenter/fluids-thermal-simulation/star-ccm/, 2024.

[121] S. I. Silton. Navier–Stokes Computations for a Spinning Projectile from Subsonic to Supersonic Speeds. *Journal of Spacecraft and Rockets*, 42(2):223–231, 2005.

[122] S. I. Silton and B. E. Howell. Aerodynamic and Flight Dynamic Characteristics of 5.56-mm Ammunition: M855. Technical Report ARL-TR-5182, Army Research Laboratory, 2010.

[123] S. I. Silton and D. W. Webb. Experimental Determination of the Effect of Rifling Grooves on the Aerodynamics of Small Caliber Projectiles. In *AIAA Atmospheric Flight Mechanics Conference and Exhibit*, Keystone, CO, August 2006.

[124] Special Forces Group (SFG). Sniper Kilo Team. http://www.sfg.be/sniper-kilo/.

[125] Tekscan. Load Cell vs. Force Sensor. https://www.tekscan.com/resources/whitepaper/load-cell-vs-force-sensor, 2024. (Accessed on 2024-04-11).

[126] J. Trevithick. The Army Is Once Again Looking to Replace the 5.56mm Cartridge. *The War Zone*, 2019. (Accessed on 2024-02-29).

[127] C. Tropea, A. L. Yarin, and J. F. Foss. *Springer Handbook of Experimental Fluid Mechanics*, volume 1. Springer Science & Business Media, 2007.

[128] P. B. Upadhyay, A. Shrivastava, and M. S. Rajpoot. Aerodynamic Characteristics of Hypersonic Vehicle with Variable Sweep-back Wing Configuration. 2009.

[129] U.S. Army. Development of firing tables for accuracy stretches back more than 100 years. https://www.army.mil/article/215516, 2018.

[130] P. Weinacht. Validation and Prediction of the Effect of Rifling Grooves on Small-Caliber

Ammunition Performance. In *AIAA Atmospheric Flight Mechanics Conference and Exhibit*, Keystone, CO, August 2006. 21–24 Aug. 2006.

[131] P. Weinacht, G. R. Cooper, and J. F. Newill. Analytical Prediction of Trajectories for High-Velocity Direct-Fire Munitions. Technical Report ARL-TR-3567, Army Research Laboratory, 2005.

[132] C. J. Welsh. Combustion in the Wake as a Means of Body-Drag Reduction as Determined from Free-Flight Tests of 40-Millimeter Shells. Research Memorandum RM SL53D01a, National Advisory Committee for Aeronautics, Langley Aeronautical Laboratory, Langley Field, Va., 1953.

[133] G. S. West and C. J. Apelt. The Effects of Tunnel Blockage and Aspect Ratio on the Mean Flow Past a Circular Cylinder with Reynolds Numbers between 10^4 and 10^5. *J. Fluid Mech.*, 114:301–325, 1982.

[134] P. Wey. *BALCO User's Guide, AOP-50 NATO technical shareable software V1.0b, Edition 1*, 2015.

[135] P. Wey et al. BALCO 6/7-DoF Trajectory Model. In *29th International Symposium of Ballistics*, Edinburgh, Scotland, 2016.

[136] R. H. Whyte and W. H. Mermagen. A Method for obtaining Aerodynamic Coefficients from yawsonde and radar data. BRL Report 2280 AD-759 482, Ballistic Research Laboratory, 1973.

[137] D. C. Wilcox. *Turbulence Modeling for CFD*. DCW Industries, Inc., 5354 Palm Drive, La Cañada, California 91011, 3rd edition, November 2006. ISBN 978-1-928729-08-2.